Swiss Federal Institute of Technology Zürich
&
Uppsala University

Master of Science Thesis in Applied Geophysics

Analysis of P- and S-wave velocities in the COSC-1 borehole, central Sweden

Author:
M.C. Ooms

Supervisors:
Prof. Dr. C. Juhlin
Dr. C. Schmelzbach

August 2016

UPPSALA
UNIVERSITET

Analysis of P- and S-wave velocities in the COSC-1 borehole, central Sweden

Master of Science Thesis

for the degree of Master of Science in Applied Geophysics at

Delft University of Technology

ETH Zürich

RWTH Aachen University

by

Michiel Cornelis Ooms

August 12, 2016

Department of Geoscience & Engineering
Department of Earth Sciences
Faculty of Georesources and Material Engineering

Delft University of Technology
ETH Zürich
RWTH Aachen University

Abstract

The Collisional Orogeny in the Scandinavian Caledonides (COSC) drilling project, supported by the International Continental Drilling Program (ICDP) and Swedish Research Council, was designed to study mountain building processes and the geologic structure and composition of the Caledonian orogeny in central Sweden. The 2.5 km deep scientific COSC-1 borehole (ICDP 5054-1-A) was successfully drilled during the spring and summer of 2014, targeting the Lower Seve Nappe Complex (SNC). With a variety of conducted seismic studies, nearly 100% core recovery, downhole well-logging and on-core measurements through the Lower SNC a comprehensive data set was obtained. This study will focus on the analysis of seismic P- and S-wave velocities of the full-waveform sonic (FWS) data set. The resulting velocities, v_p and v_s, have been used in seismic models and for comparison to other relevant studies conducted in the COSC-1 borehole. v_p and v_s showed correlation with velocities obtained from Zero-Offset VSP (ZVSP) and core measurements, indicating a varying v_p around a constant velocity and a gradually increasing v_s with depth. Correlation has been found between a gradually decreasing v_p/v_s ratio and an increasing SiO_2 content with depth, implying a gradual transition in the middle crustal composition from a mafic to a felsic environment with an average SiO_2 content of 69.89±9.23 wt% and v_p/v_s ratio of 1.70±0.14. Seismic modelling of the derived v_p, v_s and density resulted in 1D synthetic seismograms and a 2D elastic and isotropic finite-difference model, which are correlated to ZVSP and surface seismic. Seismic modelling obtained similar results as the ZVSP, both indicating a reflective Lower SNC. Reflective interfaces in the basal shear zone (>1710 m) are interpreted as due to amphibole-rich gneiss and mica schist interfaces. Similar reflectivity sequences are found in the 3D migrated section, but yielding a poorer correlation with the seismic models. Comparisons of the FWS data set show good correlations with other seismic methods which can be used in the further development of COSC, but also differences which may have to be accounted for in the future.

Keywords: full-waveform sonic logging, seismic modelling, collisional orogeny, Scandinavian Caledonides, scientific drilling, COSC-1 borehole.

Contents

List of Figures

List of Tables

Nomenclature

General terms

1D	One Dimensional
2D	Two Dimensional
3D	Three Dimensional
BL	Byxtjärn-Liten 2D reflection seismic profile
CCT	Central Caledonian Transect
COSC	Collisional Orogeny in the Scandinavian Caledonides
ICDP	International Continental Scientific Drilling Program
KF	Kallsjön-Fröå 2D reflection seismic profile
OSG	Operational Support Group
SSDP	Swedish Scientific Drilling Program

Geophysical terms

FWS	Full-Waveform Sonic
OWT	One-way Travel Time
P-wave	Compressional or primary (longitudinal) wave
R_c	Reflection coefficient
RSF	Regularly Sampled Format
S-wave	Shear or secondary (rotational) wave
SEG-Y	Specific file format for storing geophysical data
SNR	Signal to Noise Ratio
TWT	Two-way travel time
v_p	Compressional-wave velocity
v_p/v_s	Ratio of compressional-wave velocity and shear-wave velocity
v_s	Shear-wave velocity
VSP	Vertical Seismic Profiling
Z_p	Impedance of the compressional wave
Z_s	Impedance of the shear wave
ZVSP	Zero-Offset Vertical Seismic Profiling

CHAPTER 1

Introduction

In this first chapter, the subject of this study will be introduced. Section 1.1 describes the relevance of the research before concluding this chapter in Section 1.2 with the objectives and outline of this thesis.

1.1 Relevance of the COSC scientific drilling project

Geological reconstruction and geophysical measurements are powerful methods to understand the local subsurface geology. However, uncertainties in the correlation between the geological and geophysical results remain, leaving important questions unanswered. Validation of both results can be realised by employing a scientific drilling campaign, providing the best capability to determine the correlation between geologic and geophysical studies.

Scientific drilling campaigns are able to obtain a wealth of information but are not intensively employed due to the high cost of drilling. Interest in scientific drilling was raised after the successful drillings of the Kola Superdeep Borehole in Russia (Kozlovsky, 1987) and the Kontinentales Tiefbohrprogramm in Germany (Emmermann and Lauterjung, 1997). The latter led eventually to the establishment of an international platform for continental scientific drilling programs, the International Continental Scientific Drilling Program (ICDP). To date, a total of 37 ICDP supported drilling projects have been successfully executed (ICDP, 2015).

The Collisional Orogeny in the Scandinavian Caledonides (COSC) scientific drilling project is one of these ICDP supported projects, led by the Swedish Scientific Drilling Program (SSDP). Two drilling campaigns are planned in the Caledonides of western Scandinavia, which dominates the landscape of Norway and the westernmost part of Sweden and has been of geological (Törnebohm, 1888; Gee and Sturt, 1985; Corfu et al., 2014a) and geophysical (Palm, 1984; Dyrelius, 1986; Juhojuntti et al., 2001; Korja et al., 2008; Hedin, 2015) interest for more than a century. The central Swedish Caledonides have been subjected to mountain building process during a collisional orogen, resulting in the landscape as it is known today. Along with eastern Greenland, the Caledonides of central Sweden, have been recognised to have been of Alpine–Himalayan dimensions (Law et al., 2006; Gee et al., 2010) as a result of the closure of the Iapetus Ocean followed by thrusting of Baltica underneath Laurentia during the mid-Paleozoic Caledonian Orogeny (Gee et al., 2008). Extensive knowledge of the Caledonian Orogeny leads to an understanding of general mountain building processes and analogues orogens.

The COSC project is focussed on the Scandinavian mountain belt structure and mountain building processes at mid-crustal levels in the mid-Palaeozoic Caledonian Orogeny, in particular, the transport and emplacement of subduction-related high-grade allochthons with a focus on the Seve Nappe Complex (Lorenz et al., 2015a). The project is divided into two stages, each involving a fully cored 2.5 km deep borehole supported by geological and geophysical investigations in the province of Jämtland, in west central Sweden. The location of the first borehole, COSC-1, is based on a two-dimensional (2D)

seismic reflection profile (Hedin et al., 2012), complemented with surface geology, regional reflection profiles (Palm, 1984; Juhojuntti et al., 2001), regional and local gravity data (Dyrelius, 1986), and high-resolution aeromagnetics (Dyrelius, 1980). The COSC-1 borehole was therefore located and successfully drilled in 2014, near the town of Åre. Core and downhole logging measurements through the targeted Lower Seve Nappe Complex provide a comprehensive data set; regarding radioactive, electrical and acoustic properties of the formation along the wellbore.

1.2 Goals and outline of the thesis

This thesis project will focus on the full-waveform sonic (FWS) data set acquired as a part of the downhole logging measurements. Three logging runs with the compensated sonic sonde and two by the FWS sonde were required to reach total driller's depth of the COSC-1 borehole. The FWS data provides important information on the sonic properties (e.g. compressional and shear wave velocity together with the associated ratio) of the formation which can be used in the geological interpretation of the COSC-1 borehole. Recently, low-resolution surface-based seismic experiments (Hedin, 2015; Krauß et al., 2015; Simon et al., 2015) and high-resolution laboratory core measurements (Wenning et al., 2016) have been performed, although the correlation between the high- and low-resolution data sets is not been assessed yet. The goal of this thesis is to process and analyse the acquired FWS data set. Furthermore, the data set will be compared to other studies performed in and around the COSC-1 borehole. Comparison of the data sets enhances the geological knowledge and can be used as a constraint for further geophysical studies. In this thesis, the following tasks are addressed:

1. Determine the compressional (P-wave) and shear wave (S-wave) velocity along the wellbore with full-waveform sonic (FWS) data.
2. Compare the obtained P-wave and S-wave velocities with results from core measurements, Zero-Offset Vertical Seismic Profiling (ZVSP) and surface seismic.
3. Analyse the ratio of P-wave and S-wave velocities (v_p/v_s) as a lithology indicator.
4. Analyse the reflection response of seismic discontinuities as a function of offset, for P-waves, S-waves and converted waves.

The research will initially focus on the full-waveform sonic data of the COSC-1 borehole and subsequently incorporate and compare results with other studies. Finally, the data is used for interpreting the ZVSP and surface seismic data from the area.

Before presenting the investigations that form the basis of this thesis, an introduction to the project's investigation area is given in Chapter 2. In Chapter 3 is the physical theory provided of relevant seismic wave theory, FWS logging acquisition and seismic modelling in various dimensions. The processing and analysis of FWS logging data are presented in Chapter 4. P-wave and S-wave velocities are determined from the two FWS seismic data sets by processing and picking the waveforms. Other well-logs are presented along with the v_p, v_s and v_p/v_s ratio log to perform an analysis of the COSC-1 borehole. Next, the derived v_p, v_s and density information is used for 1D and 2D seismic modelling in Chapter 5. The results of the modelling are followed by a comparison with other seismic studies, i.e. ZVSP and surface seismic, in Chapter 6. Furthermore, the logging information is correlated with XRF results and core measurements followed by a discussion on general crustal composition and crustal reflectivity. Finally, conclusions and an outlook for further investigations are presented in Chapter 7.

CHAPTER 2

Background information on the central Swedish Caledonides and the COSC-1 borehole

Thorough knowledge of the geological background is required to understand the past and recent geological setting in which the COSC-1 borehole is situated. Several geological and geophysical studies have been performed to reconstruct the tectonic history of the Caledonide Orogen on regional and local scales. The COSC-1 borehole provides detailed information on the local geology of a high grade metamorphosed allochthon, therefore the selected studies are focussed on the proximity of the borehole, and the central Swedish Caledonides in general. The geological and geophysical background of the COSC study area is given in Sections 2.1 and 2.2. Section 2.3 focusses on the COSC scientific drilling project and the COSC-1 borehole. Detailed information on the full-waveform sonic log is presented in Section 2.3.1 and relevant comparative studies thereafter in Section 2.3.2.

2.1 Geological overview

The collision of continents and the resulting orogeny produces most of the major mountain belts in the world. The bedrock of central western Sweden Caledonides is part of the Caledonide Orogen which dominates the geology of western Scandinavia. Other parts of the Caledonide Orogen are mainly exposed today in the British Isles, Greenland and Svalbard (McKerrow et al., 2000; Gee et al., 2008; Gasser, 2013). Unexposed are the parts that occur below the shallow continental shelf of the North Atlantic Ocean. The Iapetus Ocean separated the continents Baltica and Laurentia prior to the Caledonian orogeny during the late Pre-Cambrium and Cambrium. Caledonian orogeny started in the early Ordovician (ca. 490 Ma) during closure of the Iapetus Ocean. By the end of the Ordovician (ca. 445 Ma), the collision had started with the development of intra-oceanic and arc-continent subduction, underthrusting Laurentia by Baltica and Avalonia (Corfu et al., 2014a). Subduction of the Baltoscandian margin beneath Laurentia continued into the early Devonian (ca. 390 Ma) followed by rapid exhumation later during the Devonian (McKerrow et al., 2000; Gee et al., 2008, 2010).

The Scandian mountain belt spans over 1000 km in longitudinal distance, from the Stavanger region in southern Norway to the Barents Sea region in northern Norway, and is 200 to 300 km in width. The basement underneath, and to the east, of the mountain belt consists from north to south of Pre-Cambrium (Archaean to Neoproterozoic) rocks of the Fennoscandian shield. The Precambrian basement was initially formed in a sequence of Palaeoproterozoic orogenies, with the Sveconorwegian orogeny being the most recent (ca. 1000 Ma). This is unconformably overlain by a thin Neoproterozoic to Palaeozoic sedimentary cover (Gee and Sturt, 1985; Corfu et al., 2014b). Törnebohm (1888) was the first to propose long-transported thrust-sheets or allochthons in the Scandinavian Caledonides. Several hundreds of kilometres of lateral emplacement have been demonstrated for some of them, with the

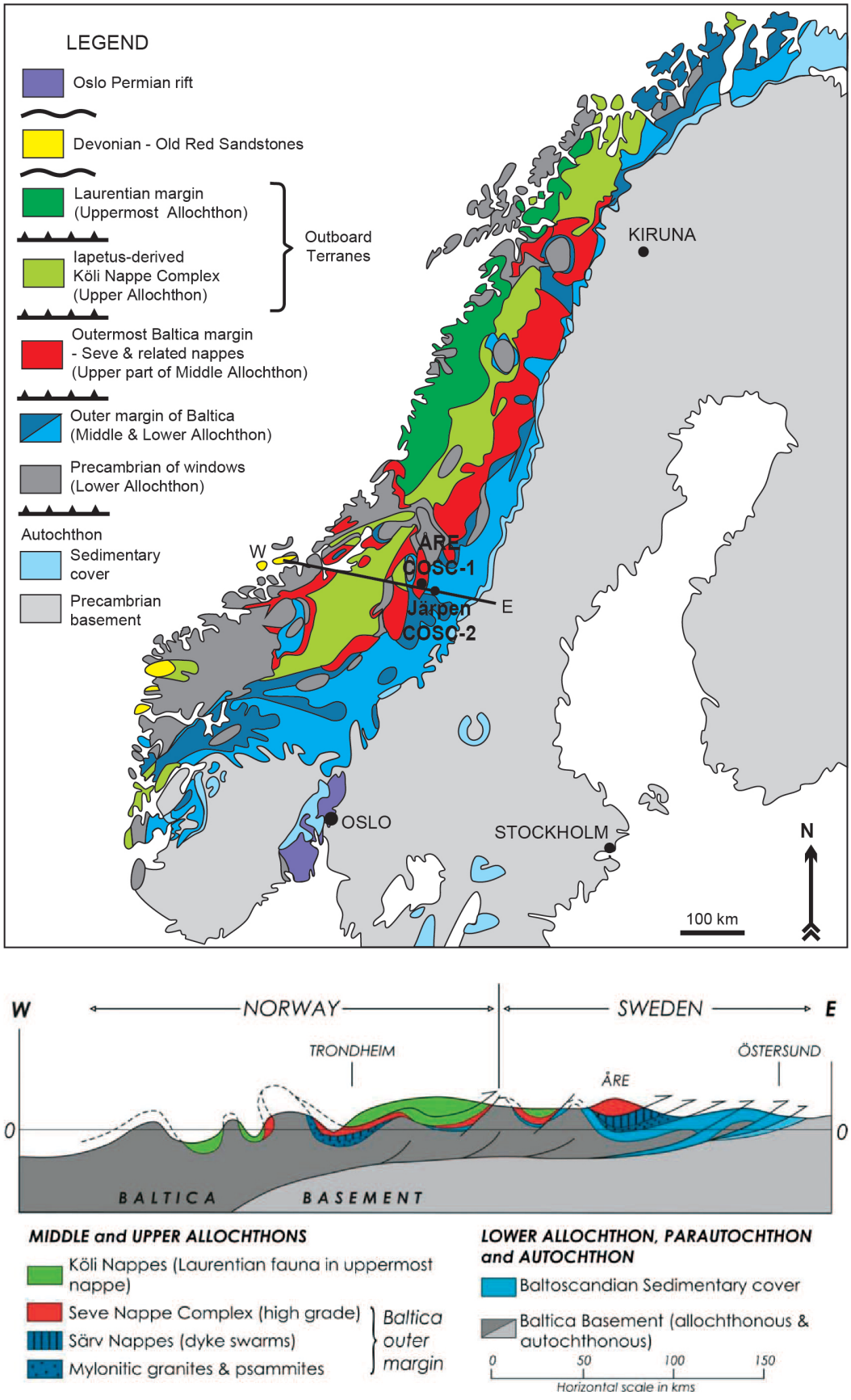

Figure 2.1: Top: Interpretation of the tectonostratigraphic map of the Scandinavian Caledonides (Gee et al., 1985). The W–E marks the approximate location of the profile. Bottom: Schematic profile through the Central Scandes (Östersund–Trondheim). Vertical exaggeration times 5 (Gee et al., 2010). Figures and captions adapted from Gee et al. (1985), Gee et al. (2010) and Geological Survey of Sweden.

highest units moved over 400 kilometres from west to east onto the Baltoscandian platform (Gee, 1975; Gee et al., 2010). Nappes which occur higher in the sequence have been transported farther relative to the lower ones as a result of displacement from locations west of Baltica's outer margin. After the closure of the Iapetus Ocean, the collision of Baltica with Laurentia, led to underthrusting of Laurentia by Baltica, folding the allochthons and basement together and continued transport eastwards onto the Baltoscandian platform.

The thrust sheets of the Scandinavian Caledonide Orogen are generally subdivided into Lower, Middle, Upper and Uppermost Allochthons (Gee et al., 1985). In Figure 2.1 an interpretation of the tectonostratigraphic representation of the Scandinavian Caledonides is shown, providing a general overview of the different rock units and structures of the orogen. Differentiation of these different units is based on their stratigraphy and tectonothermal history (Roberts and Gee, 1985). The geology of the central Scandinavian Caledonides has been extensively discussed (Gee, 1975; Dyrelius et al., 1980) and is the target of the COSC investigations. The description of the targeted Middle Allochthon provided below, is therefore specifically in the vicinity of the COSC-1 drilling operations.

The Precambrium crystalline basement mainly comprises granites and gneisses overlain by successions of Cambrium kerogen-rich black alum shales, acting as a detachment plane for nappes during Caledonian Orogeny, leading to major thrust emplacement between the autochthonous sedimentary cover and the Lower Allochthon (1-2° westwards, Gee et al., 2010). The Jämtlandian Nappes of the Lower Allochthon are dominated by Cambrian, Ordovician, and Silurian sedimentary successions, metamorphosed in subgreenschist to low greenschist facies (Gee, 1975). The Lower and overlying Middle Allochthons are separated by a major thrust. The lower part of the Middle Allochthon is dominated by characteristic gneisses, granites, and deformed meta-sandstones. Thrust over these lower units are feldspathic sandstones and arkoses cut by mafic dolerite dyke swarms from the rifted margin (Särv Nappe). Metamorphic grade increases upwards into the overlying Seve Nappe Complex (SNC) which comprises the uppermost part of the Middle Allochthon and the target of the COSC-1 drilling operation. Following Gee et al. (2010), the SNC is in general subdivided into three parts: a lower part of similar protolith to the Särv Nappes, but ductilely deformed in amphibolite facies, a central part of granulite facies migmatites and paragneisses and an upper unit dominated by amphibolites with some metamorphosed sedimentary rocks. The middle part of the Lower SNC is exposed in a quarry (N63.361862°, E13.210638°) near the COSC-1 borehole shown in Figure 2.2. The gneisses (mostly felsic and calc-silicate-bearing) with lenses of amphibolite boudins of variable thickness and meta-gabbros are encountered in the Lower SNC. A gradual increase in thickness of mylonites and presence of mica schists is reported towards the thrust zone of the Lower SNC and the underlying Särv Nappe. The overlying Köli Nappe Complex and the Uppermost Allochthon conclude the succession of nappes encountered in the Scandian mountain belt.

2.2 Previous investigations

A variety of geophysical investigations has been performed in the central Scandinavian Caledonides to provide information on the structural geology of the area. Before the COSC drilling project, geophysical investigations were employed to interpret the deeper crustal structure of the Jämtland area and basement configuration. Seismic refraction profiling (Palm, 1984) and seismic reflection surveys (Palm et al., 1991; Juhojuntti et al., 2001) concentrated on the central Scandinavian Caledonides, and were supplemented by magnetotelluric measurements (Korja et al., 2008) and magnetic and gravity maps over Scandinavia (Dyrelius, 1986). The seismic reflection profiling extended from east of the Caledonian thrust front to the Norwegian border with a distance of 160 km (Palm et al., 1991; Juhojuntti et al., 2001) and continued westwards to the Norwegian coast (Hurich et al., 1989); it is referred to as the Central Caledonian

Figure 2.2: Exposure of the Lower Seve Nappe Complex at a quarry in the vincinity of the COSC-1 borehole (N63.361862°, E13.210638°). The dominating gneisses are interrupted by amphibolite boudins in the middle of the outcrop, recognisable by the darker rocks (Photo by M.C. Ooms).

Transect (CCT).

The COSC project has led to new geophysical investigations in the central Scandinavian Caledonides. The more recent seismic surveys are high-resolution reflection seismic studies (Hedin et al., 2012), and three-dimensional (3D) reflection seismic interpretations (Hedin et al., 2014, 2016) to establish correlations between large-scale subsurface structures and surface geology. A 36 km long high-resolution reflection seismic profile, the Byxtjärn-Liten (BL), and a shorter Kallsjön-Fröå (KF) profile were acquired in the Åre area with the purpose of finding the most suitable locations for the two scientific boreholes, COSC-1 and COSC-2. The location of the seismic surveys (CCT, BL and KF) in central Jämtland are shown, together with the local geology, in Figure 2.3. The COSC-1 borehole is located on the BF reflection seismic profile and targeting the Lower SNC (Hedin et al., 2012).

2.3 The COSC-1 borehole

As part of the COSC project, the COSC-1 borehole (ICDP 5054-1-A) was successfully drilled from early May to late August 2014. Combined with the planned COSC-2 borehole, the COSC project is focused on the mid-Paleozoic Caledonide Orogen in Scandinavia in order to better understand orogenic processes, both in the past and in today's active mountain belts (Gee et al., 2010). The main scientific cross-disciplinary objectives of the COSC scientific drilling project are described by Lorenz et al. (2015a) and Hedin (2015) as follows:

1. Calibrate surface geology and geophysics in the area and reveal the nature of the sources for the observed strong reflectivity, conductivity and vast magnetic anomaly and constrain geophysical interpretations in order to use this information to increase understanding of the geological structure of the mountain belt and the Fennoscandian basement.
2. Establish a coherent model of mid-Paleozoic mountain building and to apply these new insights to the interpretation of modern analogues, in particular, the Himalaya-Tibet mountain belt (Law et al., 2006; Gee et al., 2010).
3. Refine knowledge on climate change at high latitudes, including historical global changes and recent paleo-climate developments.

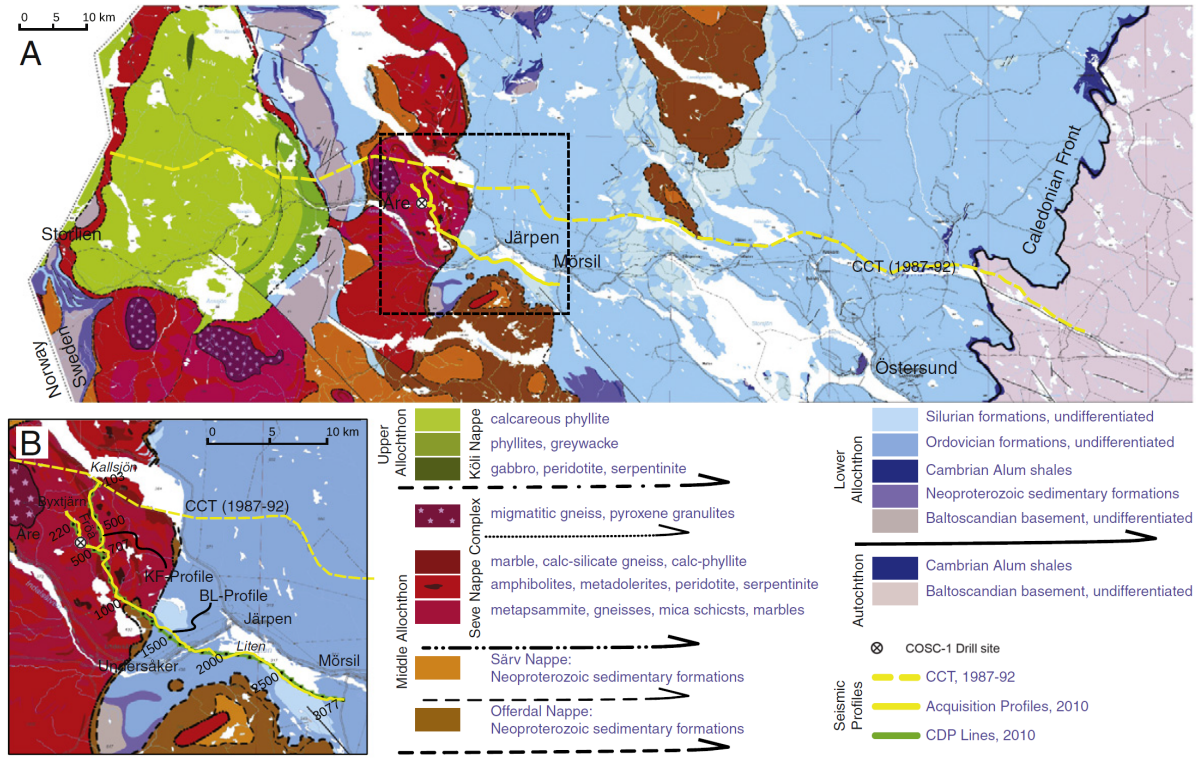

Figure 2.3: (A) Regional geology along the Swedish part of the CCT, and (B) local geology in the survey area along the Byxtjärn-Liten (BL) and Kallsjön-Fröå (KF) profiles. Numbers refer to CDP. Figure is based on Strömberg et al. (1994) and adapted with the caption from Hedin et al. (2012).

4. Understand the hydrological characteristics of the geological units and research present groundwater circulation patterns of the mountain belt.
5. Analyse the extent, functions and diversity of micro-organisms in the drill hole as a function of the different penetrated geological strata and their depth.

The COSC-1 borehole is located in the vicinity of the abandoned Fröå mine, close to the town of Åre in Jämtland, Sweden (N63.401629°, E13.202926°) and is shown in Figure 2.3. The borehole was planned to sample a thick section of the Lower SNC and to penetrate its basal thrust zone into the underlying lower grade metamorphosed Särv Nappe (Lorenz et al., 2015b). The COSC-1 borehole reached 2495.8 m driller's depth and during drilling specific attention was paid to the core recovery. Core drilling in the bedrock commenced at 102.7 m and was completed at driller's depth, by using an Atlas Copco CT20C mobile drilling rig. The equipment is capable of diamond wireline core-drilling with P, H and N sizes (hole/core diameters of 123/85 mm, 96/63 mm and 76/48 mm, respectively; Rosberg and Lorenz, 2012). After drilling a nearly 100% core recovery was achieved, leading to a 2396.0 m recovered core. The recovered drill core has a 61 mm diameter until a depth of 1615 m and 45 mm diameter from 1615 m to 2498 m. All technical operations of the COSC-1 borehole are described in Lorenz et al. (2015b) and data sets included in the COSC-1 basic data are available from the COSC-1 data repository (Lorenz et al., 2015c).

2.3.1 Full-waveform sonic logging

This thesis focusses on data from the full-waveform sonic (FWS) logging representing densely spaced in-situ acoustic measurements of various petrophysical properties, enabling correlation between low-resolution surface-based seismic experiments, high-resolution laboratory measurement and the recovered drill core. FWS logging was acquired during logging campaigns in 2014 and 2016 performed by Lund

University and the ICDP Operational Support Group (OSG).

Together with the information from the other geophysical well-logs, the FWS data can be constrained and correlated to the lithology and other physical parameters. The various sondes were employed in different logging runs, resulting in diverse depth ranges of individual logs. The depth reference of all logs is correlated with a composite log of total natural gamma measurements. Due to instrument limitations and logistics, two logging campaigns were required to obtain FWS data down to total drillers depth. The first logging campaign in May and July 2014 with the Compensated Sonic Velocity Sonde was conducted from 103.58 m to 1605.58 m, data acquisition stopped due to the decrease in borehole diameter and the pressure limitation of 20 MPa for the drill string and the sonde. In April 2016, Lund University and ICDP OSG performed FWS measurements 104.16 m to 2488.56 m by employing the BS Sonic Sonde together with the natural gamma.

In total five logging runs were required to measure the acoustic properties of the complete borehole with FWS data. The different logging runs are shown in Figure 2.4 along with a generalised tectono-stratigraphic representation of the core description. The acquisition parameters of the FWS data are described in Table 2.1. The logging campaigns were conducted with different acquisition parameters, where the Compensated Sonic Velocity Sonde acquired compensated slowness and FWS data with a source frequency of 23 kHz, the BS Sonic Sonde only collected FWS data with 20 kHz. All logging runs gathered FWS data at a near and far receiver.

Table 2.1: Acquisition parameters of the full-waveform sonic data.

	Logging tool description				
Sonde	Compensated Sonic Velocity Sonde including Full-Waveform recording (25 082 000)			BS Sonic Sonde	
Logging organisation	Lund University			ICDP OSG	
Configuration	TX2-RX2-RX1-TX1			TX-RXN-RXF	
Separation distance	TX2-RX2: 710 mm RX2-RX1: 400 mm RX1-TX1: 710 mm			TX-RXN: 250 mm RXN-RXF: 50 mm	
Source frequency	23 kHz			20 kHz	
Source interval	0.1 m			0.1 m	
Total length	4.33 m			4.45 m	
Diameter	60 mm			52 mm	
Weight	24 kg			23 kg	
Maximum temperature	70°C			150°C	
Maximum pressure	20 MPa			80 MPa	
	Acquisition system				
Recording system	WinLogger V1.5/410			Geobase	
Sampling rate	4 μs			12.8 μs	
Record length	1.916 ms			8.3968 ms	
	Full-waveform data				
Logging run	Run 1	Run 4.1	Run 4.2	Run 6.1	Run 6.2
Reference name	`FWVS1.1`	`FWVS1.3`	`FWVS1.2`	`FWVS2.1`	`FWVS2.2`
Start depth	103.58 m	924.90 m	734.95 m	104.16 m	1453.46 m
End depth	754.31 m	1605.08 m	925.23 m	1534.26 m	2488.56 m
Traces	3252	3401	950	14300	10350

2.3.2 Comparative studies

In and around the COSC-1 borehole several geophysical surveys have taken place. During drilling core recovery, downhole logging and hydrogeologic testing (Tsang et al., 2016) were the main interest. 2D

and 3D seismic reflection data were obtained post drilling (Hedin et al., 2012, 2014, 2016), supplemented by a Zero-Offset VSP (ZVSP) (Krauß et al., 2015) and a multi-azimuthal walkaway VSP survey (Simon et al., 2015). Elastic anisotropy and in-situ stress estimation from borehole data concludes the geophysical research so far (Wenning, 2015).

The COSC-1 core was analysed on site and afterwards qualitatively analysed by an XRF-scanner (Sjöqvist et al., 2015) for geochemical data and the content of minerals and trace elements (Lorenz et al., 2015b). The uppermost part down to 1700 m, of the borehole is dominated by gneisses (felsic, amphibole and calc-silicate), amphibolites and meta-gabbros. The meta-gabbros and amphibolites correlate with seismic reflections between 500 and 1000 m depth. The succession of the interval is interrupted by highly strained marbles, pegmatite dykes, and minor mylonites. Very steep fractures are encountered at about 175 m and at several levels between 1200 m and 1320 m as a result of the dissolution of calcite-rich bands in the gneisses. Below 1700 m narrow deformation bands and thin mylonites are encountered which are interpreted as the thrust zone below the SNC. With the gradual increase in thickness of mylonites, they dominate the stratigraphy below 2100 m depth along with garnets. A transition from gneiss into lower grade meta-sedimentary rocks occurs between 2345 m and 2360 m. The lower part until driller's depth is dominated by quartzite and meta-sandstone of unclear tectonostratigraphic position mylonitised to varying degree. At total driller's depth, the bottom of the basal shear zone was not reached.

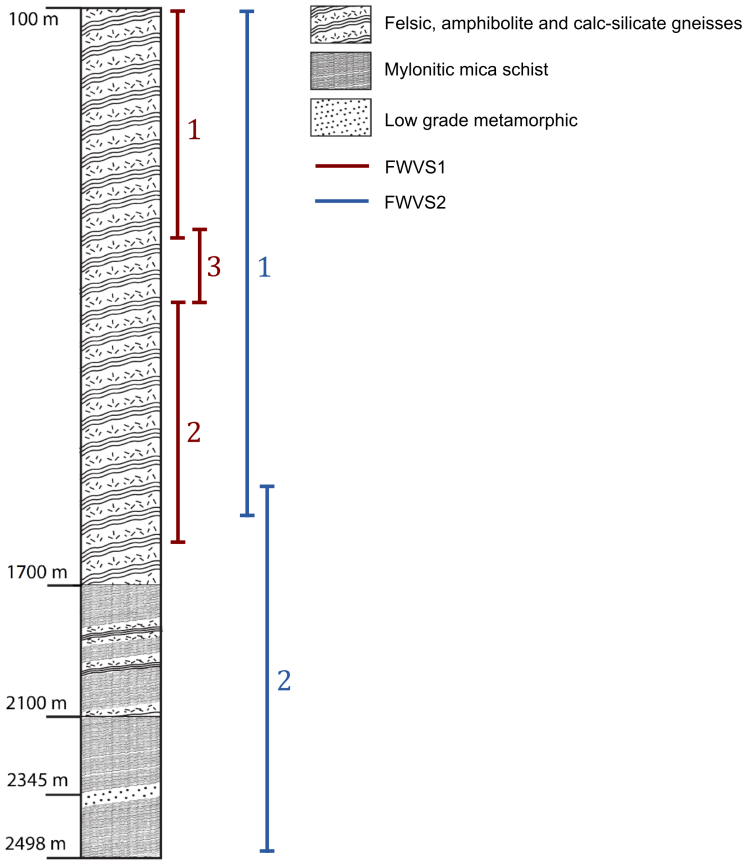

Figure 2.4: Generalized tectono-stratigraphic column following the core description after Lorenz et al. (2015a). The coloured lines represent the different logging run; `FWVS1` (red) and `FWVS2` (blue). The number indicates the extension of the reference name explained in Table 2.1.

CHAPTER 3

Physical background of seismic wave propagation

Seismic waves are transmitted to acquire full-waveform sonic data. Despite the seeming simplicity of the measurement, it contains the theory of the complex acoustic waveform. In this chapter, relevant information is provided where the research in the next chapters is based on. A brief summary is given on seismic wave propagation and body wave velocities and their characteristics in Section 3.1. The theory of seismic wave propagation is further applied on the full-waveform sonic logging method in Section 3.2, before introducing the principles of seismic modelling in Section 3.3.

3.1 Seismic waves

The propagation of a seismic disturbance through a heterogeneous medium is extremely complex. The disturbance in a solid, liquid or a gaseous medium is accompanied by a force which tries to restore the equilibrium situation. The fundamental property of matter underlies wave propagation, where the restoring character depends largely on the characteristics of the medium (Wapenaar and Berkhout, 1989). Throughout the text, the knowledge of wave propagation is used, adapted from e.g. Pilant (1979), Wapenaar and Berkhout (1989), Aki and Richards (2002) and Lowrie (2007), and is referred to for more derivations and in-depth discussions.

The 3D elastic wave equation for seismic waves transport energy is given by the elastic displacement, propagating through a source-free, isotropic, homogeneous, elastic medium:

$$\rho \frac{\partial^2 \vec{u}}{\partial t^2} = (\lambda + 2\mu)\nabla(\nabla \cdot \vec{u}) - \mu \nabla \times (\nabla \cdot \vec{u}) \tag{3.1}$$

Where ρ is the density, $\vec{u}$ is the displacement, t is the time, v is the velocity, λ and μ are Lamé constants, and ∇ is the Nabla operator, written in a 3D Cartesian coordinate system as $\nabla = \vec{e_x}\frac{\partial}{\partial x} + \vec{e_y}\frac{\partial}{\partial y} + \vec{e_z}\frac{\partial}{\partial z}$ where $\vec{e_x}$, $\vec{e_y}$ and $\vec{e_z}$ being unit vectors. The elastic wave equation accounts for both compressional and shear motion and can be separated into a compressional (P-wave) and shear (S-wave) component. The physical properties of the compressional and the shear motion are elastically different, where particle motion is established by dilation or compression of the medium parallel to the propagation direction for the compressional motion and rotational motion in perpendicular direction for the shear motion. The velocity of the P-wave is described by the bulk modulus, given by $K = \lambda + \frac{2}{3}\mu$, and shear rigidity modulus μ. The only elastic property that determines the velocity of the S-wave is the rigidity modulus (Lowrie, 2007). Therefore, the P-wave velocity is given by:

$$v_p = \sqrt{\frac{\lambda + 2\mu}{\rho}} = \sqrt{\frac{K + \frac{4}{3}\mu}{\rho}} \tag{3.2}$$

And the S-wave velocity by:

$$v_s = \sqrt{\frac{\mu}{\rho}} \tag{3.3}$$

The P-wave velocity is always higher than the S-wave velocity in a compressional medium with shear due to additional bulk modulus accounting for the velocity and the P-wave will, therefore, arrive earlier at the receiver.

The v_p and v_s both strongly depend on the density of the surrounding rock, these properties are directly related to lithology, leading to extensive research on the correlation between v_p and v_s versus density (e.g., Birch, 1960, 1961; Christensen and Mooney, 1995; Salisbury et al., 2003). As an example, Figure 3.1 shows the relation between average v_p and v_s and densities of common crystalline rocks at standard confining pressure of 200 MPa (crack-closure pressure) and room temperature (Birch, 1961; Salisbury et al., 2003). A linear correction can be applied on the velocities assuming a pressure gradient of 0.04 km·s^{-1}/100 MPa for v_p and 0.02 km·s^{-1}/100 MPa for v_s. For pressures below 200 MPa, non-linear corrections are required to account for the effect of micro-cracks. In general, velocities and density increase as the rocks become more mafic or increase in metamorphic grade.

Comparison of the compressional wave velocity to the shear wave velocity results in a convenient method of classifying lithologies (Pickett, 1960). The ratio of the compressional and shear wave velocities is obtained by combining Equations 3.2 and 3.3. Velocities of P- and S-waves are often related to each other, leading to approximately equal values for the Lamé constants. Poisson's relation $\lambda = \mu$ applies therefore for the body wave velocities (Lowrie, 2007). Media where the Poisson's relation is applicable are called Poisson solids and are described by the following equation:

$$\frac{v_p}{v_s} = \frac{\sqrt{\frac{\lambda+2\mu}{\rho}}}{\sqrt{\frac{\mu}{\rho}}} = \sqrt{\frac{\lambda+2\mu}{\mu}} \approx \sqrt{3} \tag{3.4}$$

Given that the v_p is higher compared to the v_s, based on the elastic properties of particle motion, the ratio of v_p and v_s is always higher than 1. Examples exist which deviate from the approximation of Equation 3.4, e.g. quartz-rich rocks have anomalously high shear wave velocities and mafic granulites low (Salisbury et al., 2003).

3.2 Full-waveform sonic log

The general objective of a sonic sonde is to determine the body wave velocities of the formation along the wellbore, while the associated acoustic properties closely depend on rock type and formation fluid. These acoustic properties can be obtained by measuring the transit time (Δt) of the P- and S-wave between the transmitter of an acoustic pulse and the receivers, separated by a known distance. The transmitter, usually made of a piezoelectric material producing frequencies in the range of ~20-40 kHz, introduces a sequence of acoustic pulses into the fluid within the wellbore (Schmitt et al., 2003). These acoustic pulses radiate through the borehole fluid as P-waves towards the borehole wall where partial energy is converted into S-waves.

The incident P-wave arrives at the interface of the borehole wall with an incident angle, the refracted waves of interest will propagate through the medium with an altered angle, this change in angle is controlled by the velocity contrast in the two media and is known as Snell's Law:

$$\frac{\sin i}{\sin r} = \frac{v_{p1}}{v_{p2}} \tag{3.5}$$

Where v_{p1} and v_{p2} describe the velocity contrast, i is the incidence angle and r is the refracted angle. One

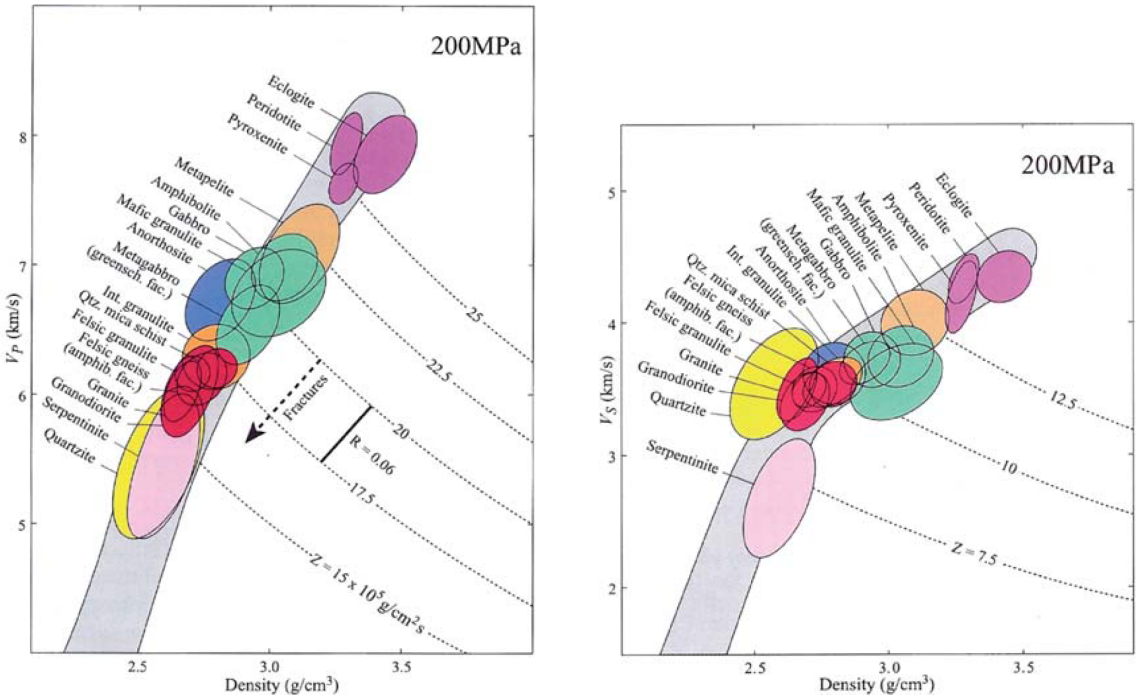

Figure 3.1: Average compressional- and shear wave velocities and densities of common crystalline rocks at a standard confining pressure of 200 MPa (crack-closure pressure) and room temperature: a) v_p versus density and b) v_s versus density. Ellipses have areas corresponding to standard deviations of density and velocities found in Salisbury et al. (2003) and major axes subparallel to Nafe-Drake curve (light-gray). Lines of constant acoustic impedance are superimposed for reference. The heavy dashed arrow shows the effect of a 10% water-filled fracture on the impedance. Figure and caption adapted from Salisbury et al. (2003).

interesting aspect of this relationship is that if the angle of the incident wave becomes large enough, then the refracted wave will travel parallel to the interface surface (Ellis and Singer, 2007). Refracted waves propagate through the rock along the wellbore and radiate back into the borehole fluid as P-waves to be detected at the receiver. A sonic sonde measures FWS by utilising two receivers, a near and far receiver. The dual receiver configuration of a sonic velocity sonde, as shown in Figure 3.2, allows accounting for the transit time of the fluid. The path of the waves from the transmitter to receivers is identical apart from the additional separation distance between the receivers in the wellbore, assuming the wellbore is smooth and the sonde is perfectly centralised. Taking the difference in transit time between both receivers results in the interval transit time of the formation. Conventionally transit times are converted to slowness:

$$s = \frac{\Delta t}{\Delta d} = \frac{t_F - t_N}{\Delta d} \tag{3.6}$$

Where s is slowness or reciprocal velocity, Δd is the separation distance of the near and far receiver, t_F and t_N are the transit times of, respectively, the far and near receiver. For all wave arrivals, the slowness is obtained. Besides the body waves, the compressional and shear waves described in Section 3.1, three other propagation modes are recorded by the full-waveform sonic tool: the fluid wave (or tube wave) and two dispersive guided modes; the pseudo-Rayleigh waves and the Stoneley waves (Mari et al., 2011). The most important parameter in detecting all five propagation modes is the property of the propagation medium, e.g. in slow formations it occurs that the shear wave and pseudo-Rayleigh waves are not detected. Several methods exist to determine poorly detected waveform arrivals by using processing algorithms, e.g. Slowness Time Coherence (Kimball and Marzetta, 1984) and Maximum-Likelihood Method (Hsu and Baggeroer, 1986).

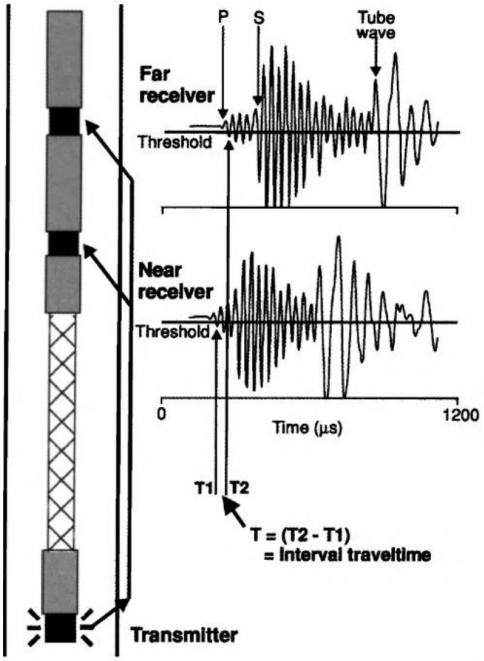

Figure 3.2: Configuration of compensated sonic velocity probe for FWS data and determination of transit times using the dual receiver configuration. Figure adapted from Schmitt et al. (2003).

In sonic logging, different configurations are used for different purposes. FWS logging employs a single transmitter or monopole source, where the acoustic pulse radiates equally in all directions. When a dipole source is used, consisting of two monopole sources of equal strength and opposite phase, the polarised shear waves can be obtained. When seismic waves propagate through a formation with intrinsic anisotropy, shear waves split or polarise into two directions perpendicular to each other (Ellis and Singer, 2007).

3.3 Seismic modelling

The subsurface is a highly heterogeneous medium and reconstruction of its structure is a challenging problem. By solving the forward problem of imaging the subsurface with seismic propagation methods an estimation is made of the seismic wave field and associated medium properties (Virieux et al., 2012). The seismic propagation method has been extensively studied based on different approximations: acoustic or elastic, isotropic or anisotropic, and attenuating effects (Karal and Keller, 1959; Alford et al., 1974; Kelly et al., 1976; Virieux, 1986; Bayliss et al., 1986; Levander, 1988; Sei, 1995).

The availability of dense data sets of medium parameters obtained by logging operations in boreholes enables to create seismic models and approximate the seismic response of the subsurface in the vicinity of the borehole. The data of FWS is limited to v_p and v_s measurements, therefore seismic modelling is limited to two variations: 1D seismic modelling and 2D isotropic and elastic finite-difference modelling.

3.3.1 1D seismic modelling

The reflection response of the encountered geological features found in well-log data can be tied to seismic data by forward modelling the seismic response of the input model, generating a one-dimensional (1D) synthetic seismogram. The input is considered to be an earth model of v_p and density. The product of density and v_p is the acoustic impedance (Z) of the layered rock in the borehole:

$$Z = \rho v_p \tag{3.7}$$

The contrast in acoustic impedance is used to calculate the reflection coefficient (R_c) at each interface:

$$R_c = \frac{Z_2 - Z_1}{Z_2 + Z_1} = \frac{\rho_2 v_{p2} - \rho_1 v_{p1}}{\rho_2 v_{p2} + \rho_1 v_{p1}} \tag{3.8}$$

To obtain a direct 1D model of the subsurface, the reflection coefficient is convolved with the source wavelet. Ideally, the source wavelet would represent a Dirac delta function and there would be no multiples nor losses by transmission or intrinsic attenuation within the layers traversed (Mari et al., 1999). A more representable source signature would be given by a Ricker or minimum phase wavelet. The convolutional model is summarised as follows:

$$s(t) = R_c(t) * w(t) + n(t) \tag{3.9}$$

Where s is the seismic trace, w is the source wavelet and n is the noise, all variables are functions of time. The seismic response makes it possible to associate known geological features with reflections in the seismic data and therefore is widely used to constrain seismic data.

3.3.2 2D elastic finite-difference modelling

The finite-difference method is the most frequently used method to model seismic wave propagation (Fichtner, 2011). Finite-difference methods can be applied to the different modes of the wave equation: acoustic, visco-acoustic, elastic (Equation 3.1) and visco-elastic wave equations. In this thesis, the 2D elastic wave equation is used.

Finite-difference methods approximate partial differential equations at discrete grid points. Wave motion is therefore described by a system of two partial differential equations based on the elastic wave equation in the vertical and horizontal direction (Karal and Keller, 1959; Kelly et al., 1976):

$$\rho \frac{\partial v_x}{\partial t} = \frac{\partial \tau_{xx}}{\partial x} + \frac{\partial \tau_{xz}}{\partial z} \tag{3.10}$$

$$\rho \frac{\partial v_z}{\partial t} = \frac{\partial \tau_{xz}}{\partial x} + \frac{\partial \tau_{zz}}{\partial z} \tag{3.11}$$

Where τ is the stress. These equations are rewritten into discretized equivalents by using a centred grid (Kelly et al., 1976) or staggered grid (Virieux, 1986; Levander, 1988). Discritized finite-difference equations require determinations of spatial and temporal sampling criteria to provide stable solutions and avoiding numerical dispersion. Courant et al. (1928) recognized a necessary stability condition in 1D, the so-called Courant–Friedrichs–Lewy (CFL) condition:

$$C = \frac{v_{max} \cdot \Delta t}{\Delta x} \leq 1 \tag{3.12}$$

Where C is the Courant or CFL number, v_{max} is the maximum velocity coinciding generally with the maximum v_p, Δt is the temporal increment and Δx is the discretization step in the spatial dimension. A necessary condition for stability of finite-difference methods is thus that the Courant number is not greater than 1. However, the CFL condition is only a necessary condition for stability but is not sufficient for convergence (LeVeque, 1992).

Stability of the discretized elastic wave equation has been extensively discussed with varying results, for 4th order spatial derivatives of homogeneous media the Courant number has been determined by several authors; e.g., Levander (1988): $C = 0.7071$, Bayliss et al. (1986): $C = 0.67$ and Sei (1995):

$C = 0.606$. By taking heterogeneity into account, the Courant number will be affected and become smaller, requiring stricter sampling. According to Virieux (1986) stability of 2D heterogeneous media is expected, provided the following equation holds:

$$v_{max} \cdot \Delta t \cdot \sqrt{\frac{1}{\Delta x^2} + \frac{1}{\Delta z^2}} \leq 1 \tag{3.13}$$

Where Δx and Δz represent the vertical plane of the spatial discretization in 2D. For the special case $\Delta x = \Delta z$, the stability condition reduces to:

$$\frac{v_{max} \cdot \Delta t}{\Delta x} \leq \frac{1}{\sqrt{2}} \tag{3.14}$$

Besides numerical instability, grid dispersion can also occur by defining a too coarse grid spacing. Grid dispersion will result in stable solutions, but dispersive waves will become visible. Unfortunately, finite-difference models are intrinsically dispersive and therefore sampling criteria to completely avoid dispersion is non-existent. In order to reduce grid dispersion the following relation should be obeyed (Virieux, 1986; Thorbecke, 2016):

$$\Delta x < \frac{\lambda_{min}}{n} = \frac{v_{min}}{f_{max}} \cdot \frac{1}{n} \tag{3.15}$$

Where λ_{min} is the minimum wavelength, v_{min} is the minimum velocity coinciding generally with the minimum v_s, f_{max} is the maximum frequency and n is the number of data points per wavelength. Unfortunately, no fixed grid points per wavelength rule exist to avoid grid dispersion. In general, 5 grid points per wavelength is considered to be sufficient to avoid erroneous interpretation from seismic responses obtained by fourth-order finite-difference methods (Alford et al., 1974). Coarser grids can be used when the order of accuracy is increased.

Besides sampling criteria inside the grid, solutions need to be found at edges of the grid. Internal interfaces are not treated by explicit boundary conditions because they are in a homogeneous formulation, represented by changes naturally occurring in elastic parameters and density (Virieux, 1986). The four edges of the finite-sized vertical grid, on the other hand, require explicit boundary conditions by applying e.g., free surface or absorbing boundary conditions. The free surface boundary condition implies that no normal or shear stresses are active on it, implemented by setting the stress normal to the surface to zero (Levander, 1988; Juhlin, 1995). The absorbing boundary conditions are implemented by thin strips along the boundary where the solution is tapered.

CHAPTER 4

Full-waveform sonic data analysis

The analysis and interpretation of the compressional and shear wave velocity are crucial in understanding the acoustical properties of the rocks in the borehole and to be able to constrain surface seismic data. In this chapter, the processes towards extracting acoustical information from the FWS data are described in detail. Firstly, the raw data is discussed to define the annotation of the data in Section 4.1, followed by the processing steps preformed on the data in Section 4.2. Next, the picking of the P- and S-wave is discussed in Section 4.3 and depth matching thereafter in Section 4.4. Finally, the body wave velocities and other well-log data will be presented and analysed in Section 4.5.

4.1 Raw data

The raw data of the FWS logging operation resulted in several data files comprising different depths and logging tools. To be able to clearly describe the applied processing steps on the individual FWS data files, the abbreviation `FWVS`$i.j$ will be used to annotate the different full-waveform sonic data sets in the remainder of this thesis. `FWVS` denotes the type of sonic data, assigned by the logging organisation. i denotes the dataset of a complete logging campaign, where $i = 1$ refers to the complete FWS data set acquired in 2014 from 103.58 m to 1605.08 m and $i = 2$ for the acquisition in April 2016 from 104.16 to 2488.56 m. j denotes the subset in a FWS data set with increasing depth, where $i = 1$ and $j = 2$ results in `FWVS1.2` and refers to the second FWS data file from 734.95 m to 925.23 m of the first FWS data set. Every data file consists of two seismic records, one from the near receiver and one from the far receiver. For an overview, the reference names are summarised in Table 2.1.

4.2 Data processing

To process, analyse and interpret the recorded waveform arrivals, the GLOBE *Claritas*$^{\text{TM}}$ V6.3.1.12576 Seismic Processing software was used. The FWS data has, in general, a high SNR, but required header correction and noise removal. The waveform arrivals were picked on the data after applying frequency filters, effectively reducing the noise at the arrivals, but has always been manually checked on quality by comparing it to the raw data.

To be able to visualise the FWS data, the composite log software WelCAD V5.1 was used to export the data in SEG-Y format. The header information of data was lacking and was added in GLOBE *Claritas*$^{\text{TM}}$. The ShotID and CHANNEL header information were added by renumbering the receiver configuration and traces. The receivers RX2 and RX1 were separated by ShotID, respectively ShotID = 1 for RXN (near receiver) and ShotID = 2 for RXF (far receiver). The CHANNEL header contained the trace numbers, starting at 1 to the last trace with an increment of 1.

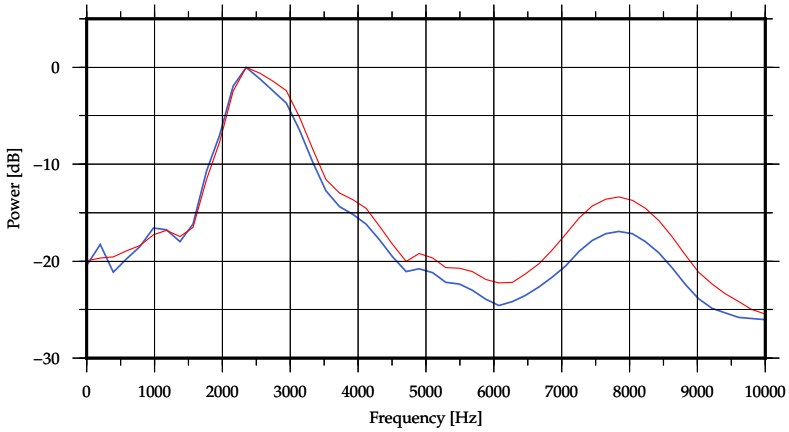

Figure 4.1: Amplitude spectra of the raw (blue line) and filtered data (red line) to increase the SNR of the *P*- and *S*-wave. The spectra are averaged over traces 700-850, 151 traces in total, of the `FWVS1.3`) far receiver from 3 to 5 ms.

Different sampling rates were used between the logging sonde and the seismic processing software to be able to increase the precision of the picked waveform arrivals. Where the sampling rate of the logging sonde was 4 μs for the `FWVS1` and 12.8 μs for the `FWVS2`, the seismic processing software uses a lower sampling rate; e.g. 10 times lower leading to a sampling rate of 40 μs for the `FWVS1` and 128 μs for the `FWVS2`. GLOBE *Claritas*$^{\text{TM}}$ is able to pick waveforms within $\pm$0.01 ms precision, by using a lower sampling rate, the precision of the picked arrivals was increased to $\pm$0.001 ms. However, the precision is decoupled from the accuracy of the picking, the actual arrival position on the waveform. The accuracy of the waveform picking will be discussed in Section 4.3.

Data sets `FWVS1` and `FWVS2` required different processing steps and are therefore discussed separately. First will the `FWVS1` data processing be discussed. In general, the `FWVS1` data showed a high SNR and required not extensive processing. Several traces contained a high level of noise up to the *P*-wave arrival at $\sim$ 2.5-3.0 ms, especially in `FWVS1.2` and `FWVS1.3`. By using frequency filtering, the coherent and incoherent noise was suppressed in the data. For frequency filtering, a zero-phase Ormsby band-pass filter was applied. The Ormsby band-pass filter was defined as a trapezoidal shaped filter and was specified by four corner frequencies [f_1, f_2, f_3, f_4]. The filter removes frequencies lower than corner frequency f_1 and higher than corner frequency f_4. Corner frequencies f_2 and f_3 are included to ramp up the removal of the frequencies. The filter has a ramped shape to avoid ringing (the so-called Gibbs phenomenon) and a slightly gentler slope on the high-frequency side (Yilmaz, 2001). The choice of the frequency filter depends on the amplitude spectra of the waveform arrivals in the raw data, represented by the blue line shown in Figure 4.1. The most effective filter proved to be 10-400-9000-10000 Hz and is represented by the red line in Figure 4.1. The filter did not alter the frequency content much, but the waveform arrivals were boosted and noise was more controlled in the frequency range 0-1000 Hz. The effect of this filter on the seismic data is shown on traces 700-1000 of `FWVS1.3` in Figure 4.2. The low frequency bandpass filter assisted in differentiating between noise and waveforms. The raw data showed noisy traces up to the *P*-wave arrival at $\sim$2.6 ms, which made it hard to differentiate between the arrival of the waveform and the noise when the picking algorithm was used. The filtered data removed effectively the noise at the arrival of the *P*-wave without changing the phase of the arrival. The amplitude of the *P*-wave arrival was slightly decreased by the frequency filter, but a clear amplitude difference remained between the noise and *P*-wave arrival. Also note the difference in amplitude between the *P*- and *S*-wave arrival, where the amplitude was boosted after frequency filtering at $\sim$4.4 ms.

The data of `FWVS2` contained a lower SNR and waveforms were not visible besides a linear arrival at $\sim$8.7 ms. Waveforms became visible after adjusting the gain significantly, but a high level of noise remained present. To define the arrivals of the waveform, frequency filters were applied to enhance the

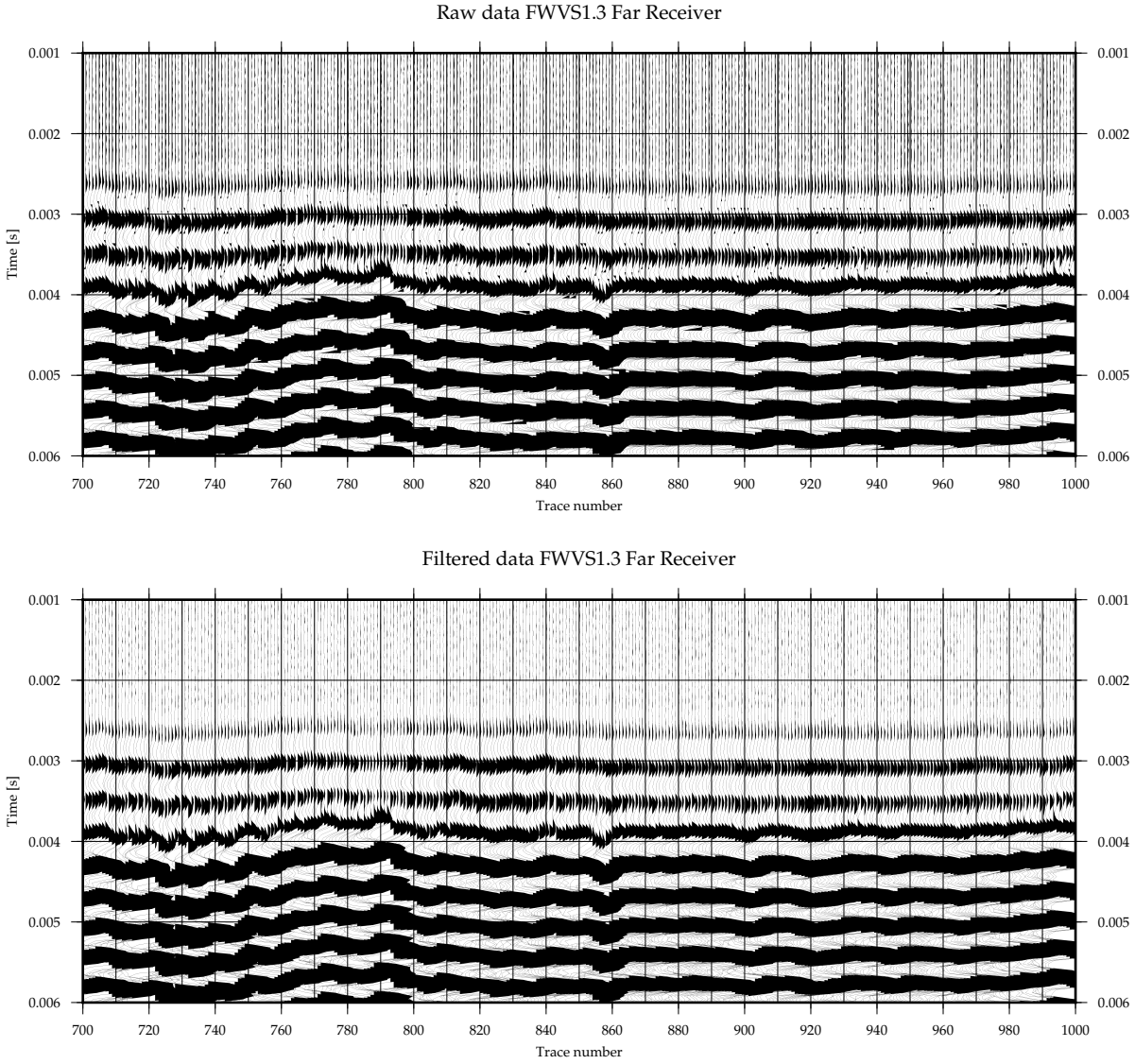

Figure 4.2: Example of a seismic recording (trace number 700-1000) from the far receiver of `FWVS1.3` before and after applying frequency filtering. The upper panel displays the raw data and the lower panel the data with a 10-400-9000-10000 Hz frequency filter.

SNR. A difference in frequency content between the `FWVS1` and `FWVS2` data was noted, arrivals of the `FWVS2` data were having a lower frequency content, ranging from 0 to 3900 Hz, compared to `FWVS1`, ranging from 0 to 10000 Hz. Several filters were tested and the best result was obtained by using two different zero-phase band-pass Butterworth filter with corner amplitudes 0.05-0.95-0.95-0.05. In Figure 4.3 the frequency content is shown of the raw data (blue lines) and the filtered data (red lines) from two seismic recordings in `FWVS2.2`. The P- and S-wave frequency content was treated separately to justify the choice of frequency filtering, therefore were the amplitude spectra only taken within the arrival itself; Figure 4.3a for the P-wave and Figure 4.3b for the S-wave. The frequency content of the noise among the P- and S-wave arrivals was different, requiring two different frequency filters for both arrivals. Where the noise near the P-wave on the raw data was ranging from 0 to 500 Hz, the noise near the S-wave was from 500 to 1250 Hz. The most effective filter for the P-wave arrival was determined to be 500-1000-3000-4500 Hz, this filter reduced the amount of noise significantly, boosted the P-wave in amplitude and did not affect the dominant frequency of 1700 Hz, as shown in Figure 4.3a. Unfortunately, the noise near the S-wave arrival has a higher frequency content and the ramp up of the 500-1000-3000-4500 Hz filter was applied before the noise frequency, resulting in a high amount remaining noise. By applying a narrower

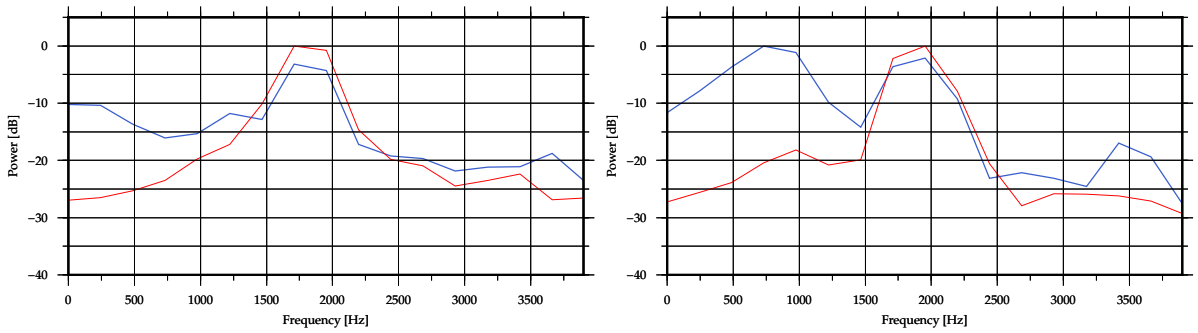

Figure 4.3: Amplitude spectra of the raw (blue line) and filtered data (red line) to increase the SNR of the *P*- and *S*-wave. The spectra are averaged over traces 1200-1350, 151 traces in total, of the `FWVS2.2` near receiver. a) *P*-wave amplitude spectra from 5 to 8 ms and application of a 500-1000-3000-4500 Hz frequency filter and b) *S*-wave amplitude spectra from 9 to 11 ms and application of a 800-1500-3000-4500 Hz frequency filter.

frequency filter of 800-1500-3000-4500 Hz and taking into account that the dominant frequency of the *S*-wave was concentrated at 1900 Hz and was less spread compared to the *P*-wave, Figure 4.3b shows an effectively reduced amount of noise at the boosted *S*-wave arrival. The result of this frequency filter will directly result in a higher SNR and a better defined *S*-wave arrival.

In Figure 4.4 the effect of the chosen filters is shown, the upper panel corresponds to the raw data, the middle panel to the 500-1000-3000-4500 Hz frequency filter and the lower panel to the 800-1500-3000-4500 Hz frequency filter. A high amount of noise was present before the *P*-wave arrival, making it difficult to pick the arrival. The *S*-wave arrival was not even visible in the raw data. After applying the 500-1000-3000-4500 Hz frequency filter the *P*-wave arrival was better defined. Unfortunately, the upper and middle panel contained both a poorly defined *S*-wave arrival, making it impossible to pick the arrival. Application of the 800-1500-3000-4500 Hz frequency filter enhanced the *S*-wave arrival in the lower panel, instead of the three horizontally linear events occurring in the upper and middle panel at 8.7, 9.9 and 11 ms, the lower panel shows five or even six *S*-wave arrivals. After applying the 800-1500-3000-4500 Hz frequency filter it enabled to pick the *S*-wave arrival on approximately traces 3100-3160, 3190-3350 and 3430-3700. The frequency filter did not allow resolving the *S*-wave arrival on all traces.

4.3 Waveform picking

Picking of the *P*- and *S*-wave transit times was performed in the seismic data view of GLOBE *Claritas*$^{\text{TM}}$ by using an automatic picking algorithm. Unfortunately, the data, especially the *P*-wave arrival, contained a remaining amount of noise which could not be removed by the frequency filter without affecting the wavelet of the arrivals. Therefore was the automatic picking algorithm supported by manual picking. The cross-correlation (XCF) automatic picking algorithm, searches for the first positive zero-crossing near the indicated waveform arrival. Differentiation between the waveforms was mainly visible by amplitudes analysis and rock property approximations.

The picking procedure of the waveform transit times is supported by Figure 4.5, showing a seismic recording of the filtered data at the near receiver of `FWVS1.1`. Trace number 1900-2300 were selected in the upper panel to give an overview of the seismic recording and show picking location of the first *P*-wave (green line) and *S*-wave arrival (pink line). The noise has a low amplitude without any continuity hence a contrast is visible between the higher amplitude *P*-wave and noise, also is the *P*-wave having continuous refractions. The differences between *P*- and *S*-waves were found in the amplitude, where the *S*-wave has a higher amplitude, and the slope of the refraction, in general the *S*-waves were having steeper slopes. The lower left panel of Figure 4.5 shows an enlarged image of the first *P*-wave arrival picked in green.

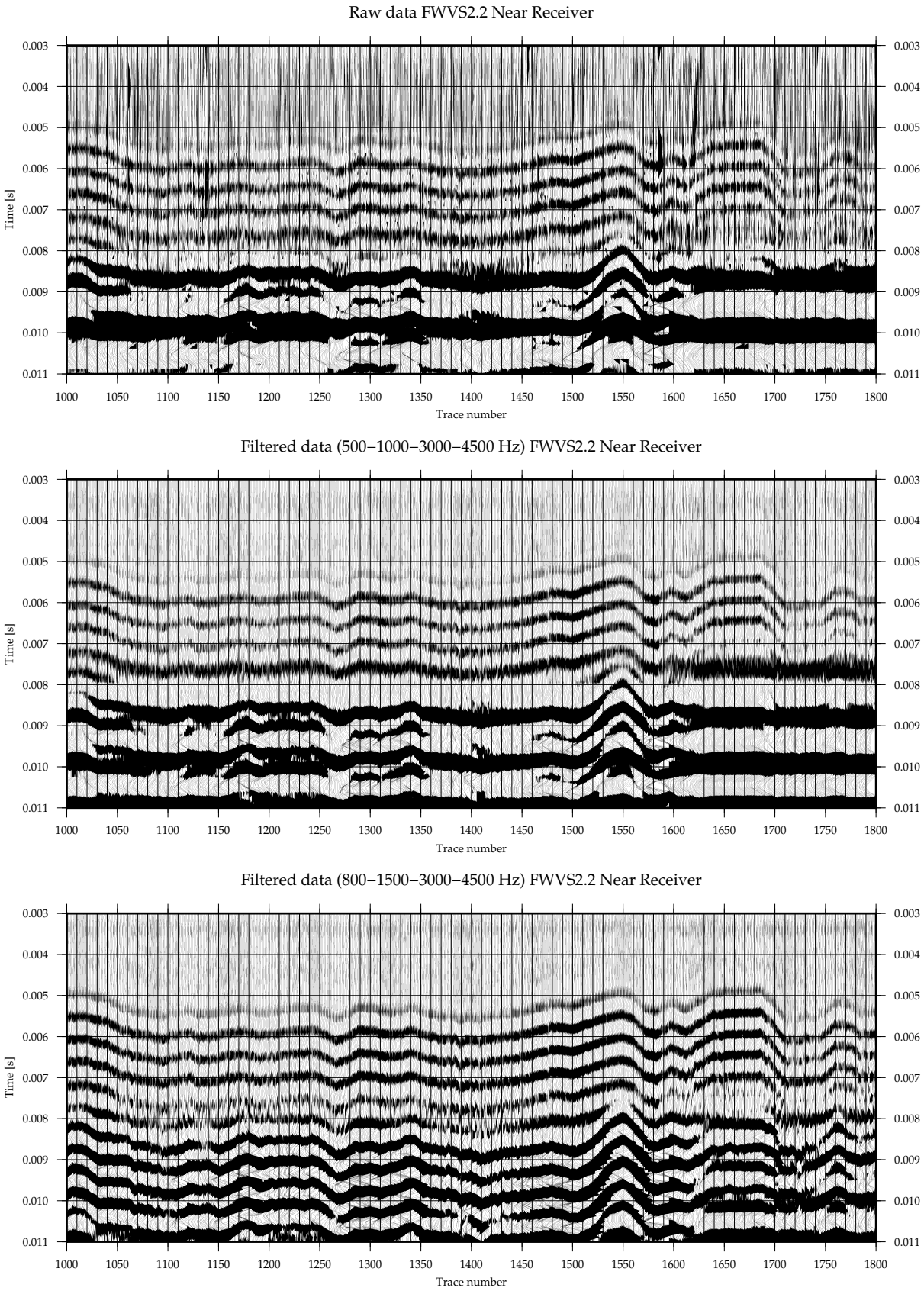

Figure 4.4: Example of a seismic recording (trace number 1000-1800) from the far receiver of `FWVS2.2` before and after applying frequency filtering. The upper panel is displaying the raw data, middle panel the data with a 500-1000-3000-4500 Hz zero-phase band-pass Butterworth filter and the lower panel the data with a 800-1500-3000-4500 Hz zero-phase band-pass Butterworth filter.

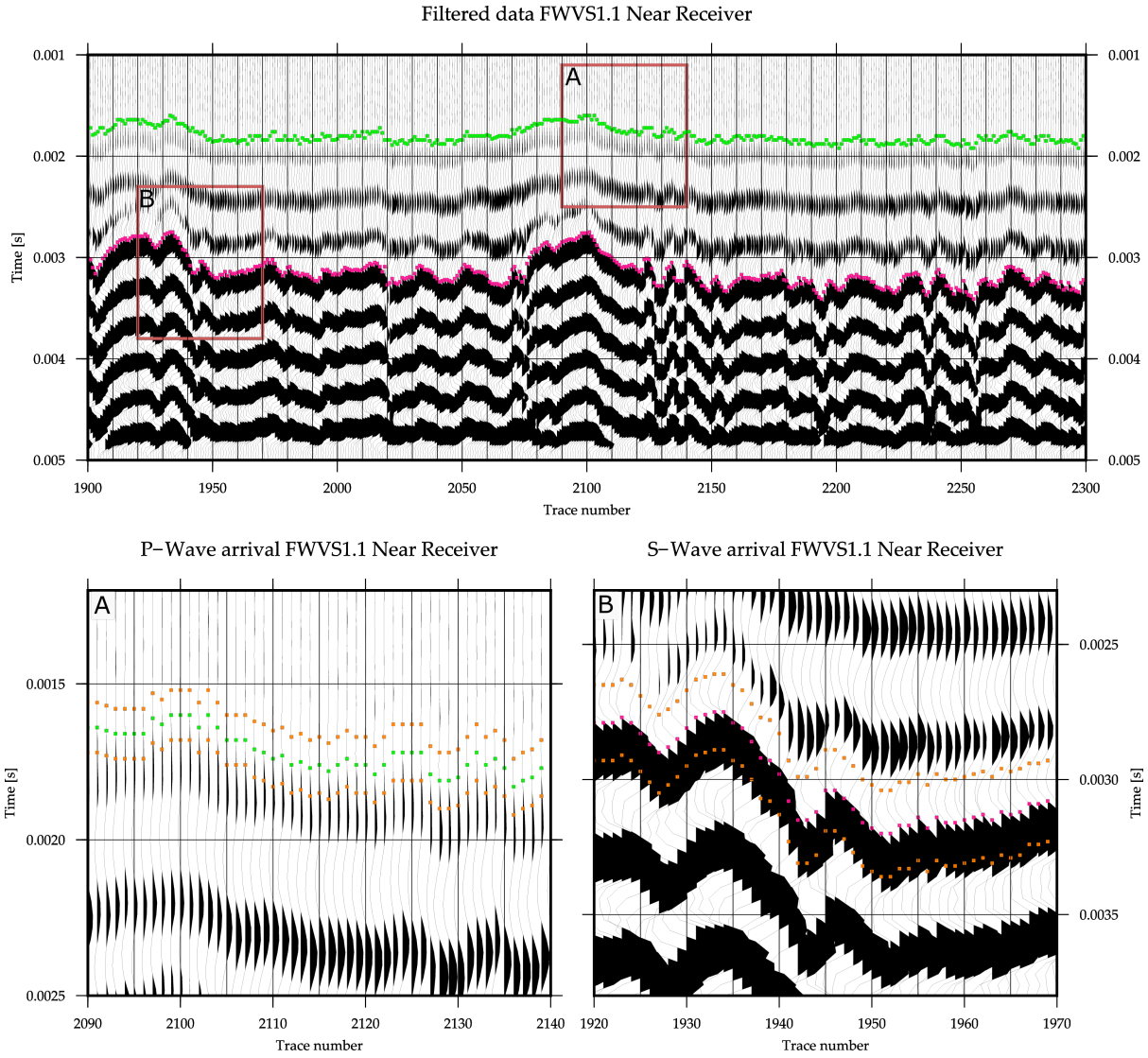

Figure 4.5: Upper panel: Picking of the P- (green) and S-wave arrival (pink) on traces 1900-2300 of the `FWVS2.1` near receiver. The red boxes indicate the location of a detailed analysis of the P- and S-wave arrival. Lower left panel: detailed analysis of the first P-wave arrival (green) and the 5% error range (orange) on traces 2090-2140. Lower right panel: detailed analysis of the first S-wave arrival (green) and the 5% error range (orange) on traces 1920-1970.

Due to the irregularities in the amplitude of the noise, it is difficult to determine the first zero-crossing of the P-wave by using the automatic picking algorithm, therefore manual picking was also used. The P-wave transit times were mostly picked in the range of 1.60 ms to 1.75 ms. By assuming Poisson's relation according to Equation 3.4, a first approximation of the S-wave transit time was made and was estimated between 2.77 ms and 3.03 ms. The lower right panel of Figure 4.5 shows an enlarged image of the first S-wave arrival picking in pink. The picked arrival was identified as the S-wave arrival by its increase in amplitude. By comparing the picked arrivals and the first crude estimation of the arrival, it can be concluded that the two results are in line. Better visible in the upper panel, the S-wave arrival has steeper slopes compared to the P-wave arrival around traces 1905-1930 and 2070-2100, making sure the S-wave is found. Beside the picked arrival in the lower panels, also the 5% error margin on the transit times is shown. By using these error margins it becomes visible that a wrongly picked arrival, due to the picking algorithm or manual picking error, makes a large difference on the location of the transit time picking. Especially the P-wave arrival was subjected to error in the picking. The 5% error margin before the waveform arrival results in a clear picking in the noise, where 5% late error margin

results in picking on the onset of the waveform. The margins on the S-wave arrival imply that a 5% erroneous picking lead to picking locations on the slope down of the last P-wave and first S-wave. The accuracy of transit times is therefore always within the 5% error margin and often smaller. It has to be kept in mind that an erroneous pick should only occur at one of the two receivers, when both picks are slightly earlier this would yield a velocity within the acceptable range.

The picking of the body waves has been performed on all data files of `FWVS1` and `FWVS2`, several general observations can be formulated after the picking:

- The overall quality of the `FWVS1` data was higher than the `FWVS2` data, requiring less frequency filtering and better resolved waveform arrivals.
- In every data file of `FWVS1` and `FWVS2` it was possible to pick the first P-wave arrival on all 14300 non-overlapping traces. However, this was not possible for the S-wave arrival in `FWVS2`. First of all, in Figure 4.3 it was identified that the frequency filter was not able to resolve the S-wave on all traces, therefore are 20211 traces resolved of the 23828 non-overlapping traces, hence 84.82% of the S-wave transit times is obtained. Secondly, the S-wave transit time is determined by picking on the second S-wave arrival, because the first arrival is not as consistent as the second arrival over the complete data files, which would lead to further data loss.
- In the first 900 traces of `FWVS1.1` and `FWVS2.1` large discontinuities in the P- and S-wave refractions occur, making it difficult to pick the arrivals. The discontinuities lead to a higher transit time and eventually to lower velocities.
- Specifically for the `FWVS1` data set, the S-wave was not as pronounced on the first 500 traces of `FWVS1.1` as on the remaining traces of the data set, where there is a sharp contrast in amplitude between the multiple P-wave arrivals and the first S-wave arrival. The S-wave is interfering with the last P-wave arrival resulting in unclear arrival transit times. Furthermore, the noise near the P-wave arrival is increasing with depth, making the P-wave arrival less continuous and harder to distinguish due to interference of the noise.

After picking the P- and S-wave transit time on both receivers for every data file, the transit times are converted to v_p and v_s by taking the reciprocal function of Equation 3.6. The v_p and v_s are now used in all following steps of the analysis.

4.4 Depth matching

In total 9 logging runs have been performed in the COSC-1 borehole, 7 runs by Lund University and 2 by ICDP OSG. All geophysical well-logs which are not run on the same tool are off-depth and require therefore correction in depth. Differences between the logging runs occur due to different tool sizes, logging velocities and approximated starting depths. In order to correlate the FWS data with the lithology, depth matching is performed according to a reference log. The depth reference for the COSC-1 borehole is a composite log of the total natural gamma measurements (`GR_DLL_Master`) from the oriented borehole geometry and electric rock resistivity logging in the ICDP-OSG logging I campaign (Lorenz et al., 2015b). The `GR_DLL_Master` log is chosen as a reference log based on the amount of individual logging runs made use of the total natural gamma, making it more accurate to match the different total natural gamma logging runs to each other.

All down-hole logs were depth matched in WellCAD, however the process differed between the `FWVS1` and `FWVS2` data set. The Compensated Sonic Velocity Sonde simultaneously measured the `FWVS1` and the compensated slowness data. However, the Compensated Sonic Velocity Sonde was run without the addition of a total natural gamma tool. Acoustic properties correlate not very clearly with radioactive properties of the investigated rock volume, therefore were the acoustic properties depth matched to

density. Slowness, v_p and v_s are dependent on density, so it is reasonable that a relationship exists or more distinct correlation compared to radioactive measurements. For this reason was the high-resolution density log (part of the sidewall density tool employed by Lund University in their fourth logging campaign) first depth matched to the reference log by direct correlation of two total natural gamma logs. Next, the three FWS logging runs (`FWVS1.1`, `FWVS1.2` and `FWVS1.3`) were all individually depth matched to the high resolution density log. Well ties, made to bulk shift, compress or extend logging data locally, were not exceeding vertical differences larger than ±2 m. After depth matching the three individual files, both density and acoustic data, were merged into a single file, leading to a total well-log covering depths of 103 m till 1605 m. During merging of the individual files, overlap between the files occurred, therefore the beginning of a new logging file was discarded in favour of the previous file while the beginning of new files contain bad data on the first traces. The BS Sonic Sone measured the `FWVS2` together with total natural gamma, therefore were the two data files (`FWVS2.1` and `FWVS2.2`) directly corrected for depth against the `GR_DLL_Master`, which was performed by the ICDP OSG.

4.5 Analysis of the logging data

After performing the data processing on the FWS data, the most essential logs are presented in Figure 4.6. The v_p, v_s and ratio of v_p and v_s resulted from the two FWS data sets, the first data set (red line) spanning a depth from 104 to 1604 m and the second data set (blue line) from 107 m to 2498 m. Besides the acoustic properties, also the density of the density log (red line) and core density (blue line) are presented. All these rock properties are related to the natural gamma log of the `GR_DLL_Master`. For displaying purposes are all logs smoothed by a 25 data-point moving filter prior to plotting, except the core density, where a 75 data-point moving filter is used.

The v_p logs in Figure 4.6a exhibit similarities at overlapping positions, distinct peaks in the data are captured by both measurements. Both data sets are bounded by velocities between 5000 and 6500 m/s, within the acceptable ranges of rock properties until 5 km crustal depth (Christensen and Mooney, 1995). The v_p shows a continuous record until the eventual depth of the log, except for some sharp peaks not related to rock properties but to fracturing; at 144 m and 177 m the v_p decrease abruptly to 3400 m/s and 3500 m/s, respectively. Further fluctuations are due to rock properties and are also visible in density and natural gamma logs. In the uppermost 350 m velocities are similar, before drifting apart to maximum 500 m/s until 1250 m where the drift is decreasing. The driving force behind drift is not found, but the body wave velocities depend on the complex interplay between transmitter-receiver spacing, formation type and source frequency (Serra, 1984). As shown in Table 2.1, distinct differences exist between the two FWS acquisitions in source frequency and separation distance, which could lead to a drift between the two data sets. The general trend of the v_p over the complete depth of the borehole is identified by a fluctuating v_p as follows: first slowly increasing (from 5200 m/s at 104 m to 6000 m/s at 630 m), followed by fluctuations of increasing and decreasing velocities reinstalling continuously around 6000 m/s (from 630 m to 2300 m) and a small decrease in the lowermost part (from 6000 m/s at 2300 m to 5500 m/s at total driller's depth).

The v_s logs in Figure 4.6b show similar behaviour between the two data sets as the v_p logs, the v_s is similar and both logs contain the same peaks with depth. Both data sets are bounded by velocities between 2500 and 4000 m/s, where the fluctuating v_s, as a result of changing rock properties with depth, shows an important general trend over the complete borehole for lithology identification. Besides the small scale fluctuations, the v_s exhibits a gradual increase in velocity with depth; ∼3000 m/s at 104 m to 3750 m/s at total driller's depth. Christensen (1965) discussed the dependence of velocity on porosity, mineral orientation, and mineral composition. The highly deformed metamorphic rocks

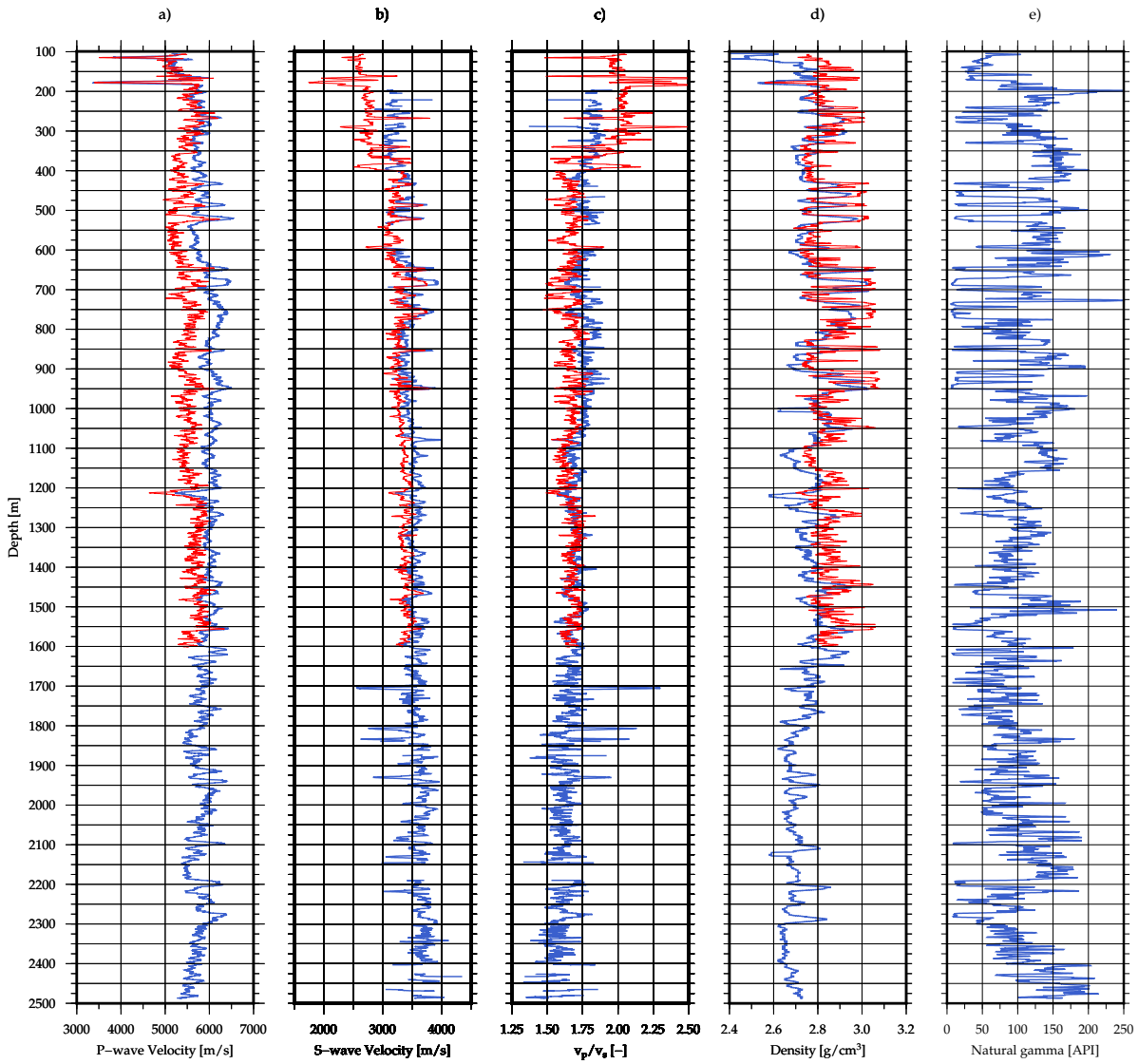

Figure 4.6: Well-log measurements of the COSC-1 borehole: a) the P-wave velocity, b) S-wave velocity, c) v_p/v_s ratio, d) density and e) natural gamma log. The v_p, v_s and v_p/v_s logs from the `FWVS1` data set is shown in red and from the `FWVS2` data set in blue. The density log is given in red and the core density in blue.

contain very small porosity leading to compaction with increasing overburden pressure. This could be one explanation for an increase in v_s, but is not validated in this study. Previous research is performed on the velocities through six important lithological units (Wenning et al., 2016), proving high anisotropic behaviour up to 18%-24% in the bottom of the borehole. However, the bottom part is consisting of amphibole-rich and micaschist lineated perpendicular to the preferential direction of wave propagation in the FWS logging acquisition and contradicting the increase in v_s. Besides the possible implication of confining pressure, resulting in an increase in v_s, the following chapters will treat the effect of mineral composition with depth.

Most of the occurring peaks are correlating with the v_p logs as a result of changing rock properties, for example the two distinct positive peaks at 650 m and 680 m, and the negative peak at 1210 m. Furthermore, note that the fluctuations of v_s are more constant and smaller velocity changes than in the v_p log. Besides the visual comparison with the v_p logs, differences exist between the two v_s logs. In general is the drift of the v_s logs less than the v_p logs, but noticeable is the difference between the logs in the top 400 m, where the v_s of `FWVS2` is continuous, is the v_s of `FWVS1` having a lower velocity (∼200-350 m/s). Unfortunately is the v_s information in the uppermost 200 m of the `FWVS2` missing,

so the continuity is not proven for the complete borehole. An explanation of the drift is due to the differences in borehole condition, where `FWVS1` is acquired during the drilling process implying borehole disturbance at time of acquisition. `FWVS2` is acquired after two years of undisturbed conditions where the borehole could be restored. Another feature in `FWVS2` is the five distinct peaks at 1705, 1807, 1834, 1931, 2130 and 2217 m, where each peak represents a 5 to 10 m thick layer. Revisiting the seismic recordings leads to the observation of real features, not caused by erroneous picking.

The v_p/v_s ratio log in Figure 4.6c is showing the ratio of the compressional and shear wave, indicating lithology changes with depth. Values for the v_p/v_s are found between 1.5 and 2.0. Due to the v_p and gradual increasing v_s, the v_p/v_s log shows a gradual decrease in v_p/v_s ratio; 1.7 at the top to 1.5 at the bottom of the borehole. Fluctuations and differences in v_p and v_s are still directly visible in the v_p/v_s ratio log, but falls back into the pattern of gradual decrease as a result of the increasing v_s. Where the general trend of the v_p/v_s ratio depends mostly on the v_s, the lowermost part is poorly defined by the v_s log and it is noted that the decrease in v_p is contributing to the decrease of the v_p/v_s ratio. The changing v_p/v_s ratio implies a gradual change in environment. From the core description is known that the environment is changing from mafic to felsic, which is also shown in the v_p/v_s ratio log. The v_p/v_s ratio log proves to be good lithology indicator.

The density logs in Figure 4.6d are measured with variable methods, the high resolution density log is acquired through well-logging down to 1605 m and the core density is measured by scanning the complete core sections down to driller's depth in a laboratory (Sjöqvist et al., 2015). The core is not acquired in one piece and is therefore broken up, when measuring the core density results in a high fluctuating density values due to these transitions between core sections and required more filtering. The core density and high resolution density log correlate well around changing density values. Density values are found between 2.5 and 3.1 g/cm^3. Nevertheless, the core density measures continuously slightly lower density values and has much lower values when low density values are measured. Also a shift in depth is noticed from 850 m, peaks in the high resolution density log start occurring earlier than the core density.

The total natural gamma in Figure 4.6e is directly related to the environment of the rocks, the fluctuations in the top 950 m between 30 and 150 API show quick changes in the rock environment, which are not as clearly visible in the acoustic and density information. In the bottom part, the total natural gamma is showing slowly fluctuating larger trends.

The decreasing v_p/v_s ratio indicated a gradual transition from mafic to felsic rocks, this is now supported by an increase in natural gamma and a decrease in density. Felsic rocks contribute to high natural gamma, due to the presence of quartz, and generally have a lower density than mafic rocks (e.g. shown in Figure 3.1; Salisbury et al., 2003). The natural gamma and density log provide an indication of layer thickness by highly varying values for different rock types, which is not seen as clearly in the acoustic logs The upper part contains thin layers of varying mafic and felsic origin, supported by the geological interpretation of the core. Progressing downward, layer thickness increases with increasing natural gamma and decreasing density.

The well-logs will be used in this research for seismic modelling, presented in the next chapter. Furthermore, the implications of the well-logs will be discussed based on the chemical data and reference studies.

CHAPTER 5

Seismic modelling

The theoretical background on seismic modelling described in Chapter 3, is used and several models are created to model the COSC-1 borehole in various dimensions. The compressional wave velocity and density information are used to generate 1D synthetic seismograms in Section 5.1. Additional shear wave velocity is incorporated to generate a 2D elastic and isotropic finite-differences model in Section 5.2. The results of 1D seismic modelling and 2D finite-differences modelling are compared in Section 5.3.

5.1 Synthetic seismogram

The FWS data is used to tie encountered geological features in the COSC-1 borehole to surface seismic data. By using the available v_p and density information, the reflection response of the COSC-1 borehole is modelled in 1D. Synthetic seismograms are generated from the two different FWS data sets, by applying the steps described in Section 3.3.1. The reflection coefficient (R_c) is convolved with wavelets containing different frequencies. The chosen frequencies are based on the dominant frequencies of the ZVSP and surface seismic. The down-going wave field of the ZVSP data describes the dominant frequency content of the source, which is 65 Hz. A similar approach is performed for the 3D reflection seismic data; the frequency content of the receiver gather close to the borehole (PEG226) is analysed and the dominant frequency is determined as 50 Hz. The synthetic seismograms of `FWVS1` and `FWVS2` are shown in Figure 5.1 and Figure 5.2, respectively.

Figures 5.1a-b and 5.2a-b show the 50 data point averaged v_p and density log of Figure 4.6. Averaging is performed to correlate well-logs to the lithology and generate more clear R_c, creating so-called "blocky" well-logs. The impedance in Figures 5.1c and 5.2c is calculated according to Equation 3.7 and afterwards converted to the time domain resulting in one-way travel time (OWT) and subsequently transformed to two-way travel time (TWT), enabling correlation with seismic data. The FWS data starts just below the casing of the borehole at a depth of approximately 103 m, so an initial approximation of time is made consisting of the first 1000 averaged data points (v_p = 5200 m/s and ρ = 2.68 g/cm^3). The impedance log as a function of TWT is re-sampled to 1 ms before calculation of the R_c in Figures 5.1d and 5.2d. The highest amplitude in the R_c is for both data sets occurring in the uppermost part of the borehole, around 0.06 s. Furthermore, R_c of 0.05 are encountered throughout the complete borehole for both data sets. The synthetic seismograms are presented in Figures 5.1e-f and 5.2e-f for the convolution with a 50 Hz and 65 Hz minimum phase wavelet, respectively. The differences between the two synthetic seismograms are visible by higher occurring amplitudes and additional reflections after a peak in the R_c when using a higher frequency for the wavelet. For example, at 0.06 s the 50 Hz minimum phase wavelet in Figure 5.2e generates two reflections, where the 65 Hz minimum phase wavelet generates three reflections.

Similar v_p and density logs of the `FWVS1` and `FWVS2` data set result in similar impedance logs. It was observed that the v_p in `FWVS2` has a higher velocity between 400 and 1200 m, this is visible in the

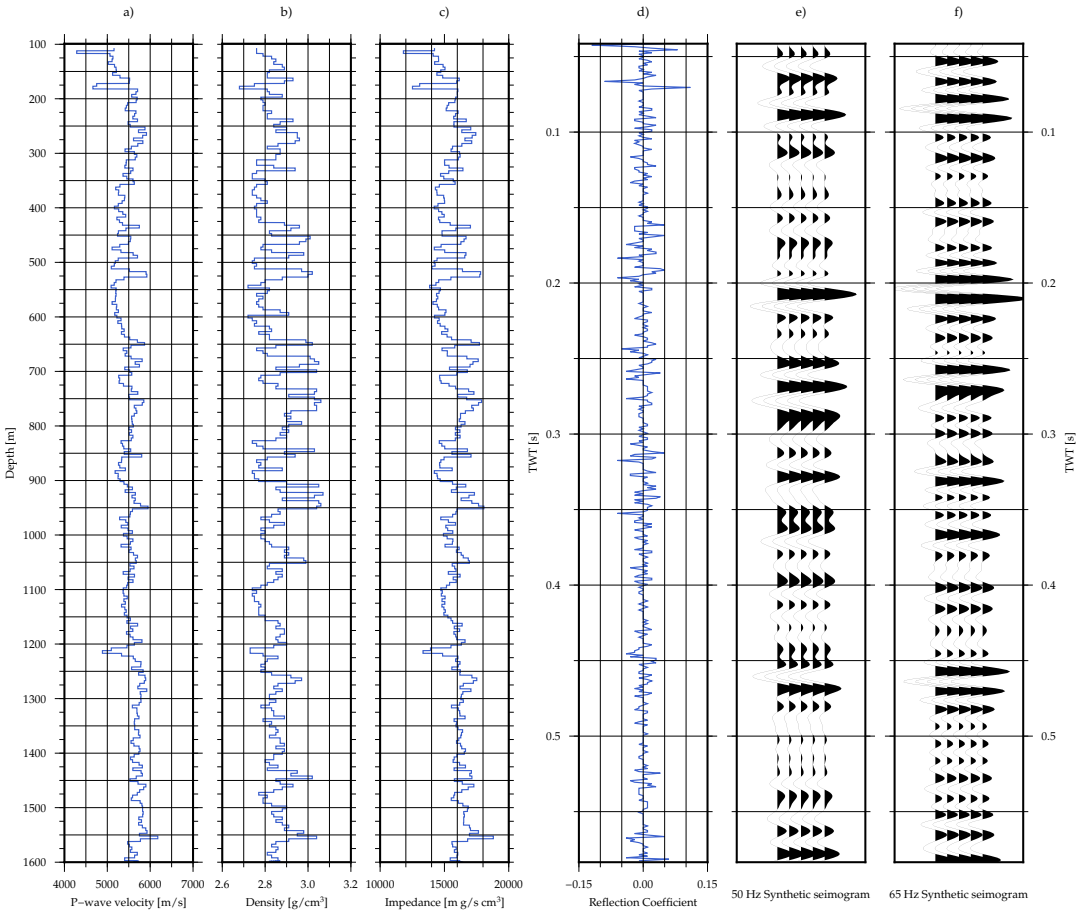

Figure 5.1: Generation of the synthetic seismogram from blocky v_p and density logs of `FWVS1` from the complete COSC-1 borehole: a) the blocky P-wave velocity, b) the blocky core density, c) the P-wave impedance, d) the R_c and e) the synthetic seismogram by convolving the reflection coefficient with a 50 Hz minimum phase wavelet. The impedance log is converted to the time domain and re-sampled prior to calculating the reflection coefficient.

R_c after the v_p is used to transform the impedance as a function of depth to TWT. High amplitude reflections occur later in time, starting after 0.15 s for the synthetic seismograms of `FWVS1`, e.g. the two positive reflections in Figure 5.1f at 0.46 and 0.47 s have a 0.03 s delay compared to Figure 5.2f where the same reflections occur at 0.43 and 0.44 s. Nevertheless, similar sequences of significant reflections are generated, therefore it is likely that reflections in the surface seismic section will resemble the 1D seismic modelling results. In the unique part of `FWVS2` from 1600 to 2500 m, the synthetic seismograms show a decrease in amplitudes after 0.56 s indicating a less reflective lower part of the borehole. Three distinct reflections with high amplitude in both synthetic seismograms remain between 0.76 and 0.80 s.

For the comparison, only the synthetic seismograms of `FWVS2` will be used because the velocities are known over the complete borehole, being able to correlate the FWS data to deeper parts of the other seismic studies.

5.2 2D seismic model

Extending the seismic model from 1D to 2D has major advantages. First of all, the 1D synthetic seismogram only provides information at zero-offset of the borehole while the 2D model shows the seismic response as an offset function. Furthermore, the 2D seismic model utilises the v_s additionally to the v_p and density, which is neglected by the 1D model. For these reasons it is decided to expand the seismic model to 2D, being able to approximate the seismic response in and around the borehole by

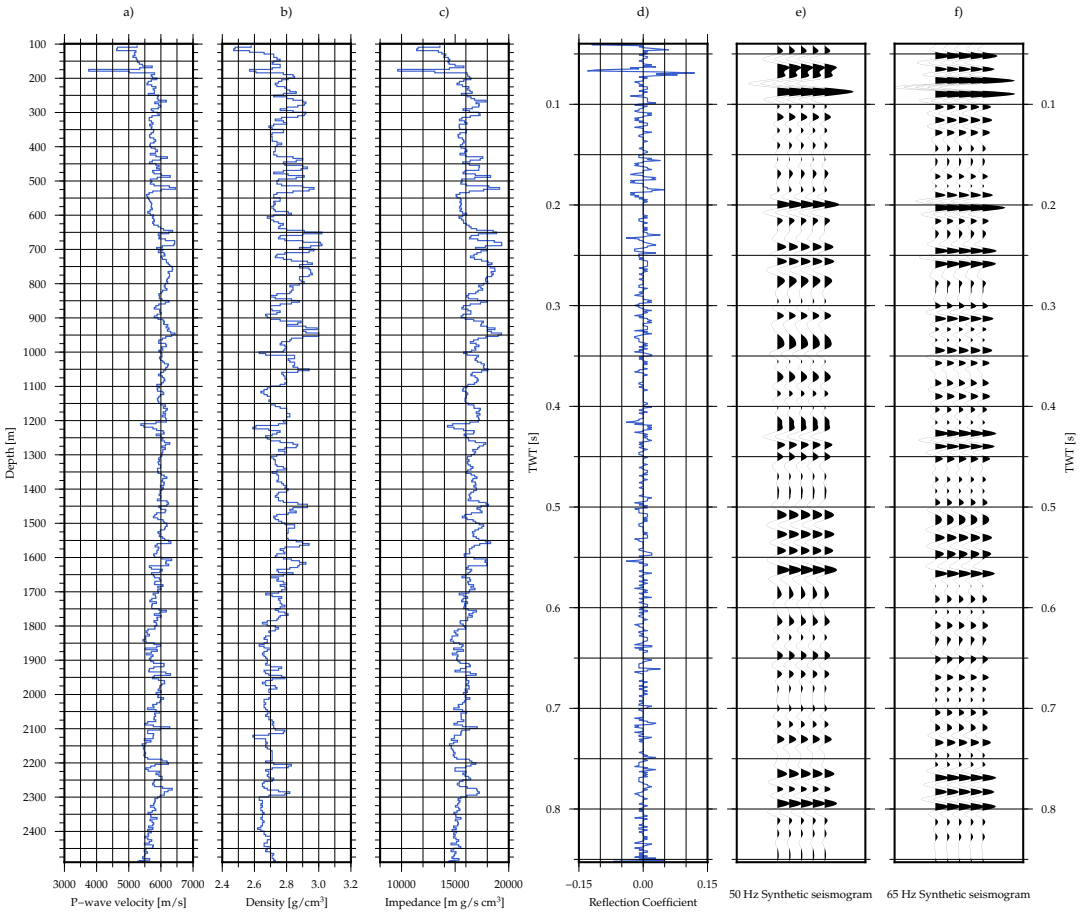

Figure 5.2: Generation of the synthetic seismogram from blocky v_p and density logs of `FWVS2` from the complete COSC-1 borehole: a) the blocky P-wave velocity, b) the blocky core density, c) the P-wave impedance, d) the reflection coefficient and e) the synthetic seismogram by convolving the reflection coefficient with a 50 Hz minimum phase wavelet. The impedance log is converted to the time domain and re-sampled prior to calculating the reflection coefficient.

using all geophysical information available from the FWS data.

2D finite-difference modelling comes also with a computational cost, therefore is efficiently modelling of seismic data sets in complex media an important challenge in computational geophysics (Weiss and Shragge, 2013). The 2D seismic model is therefore computed in Madagascar. Madagascar is an open-source software package and implements a computational environment that is designed for conducting computational challenging experiments in the area of large-scale geophysical data analysis (Fomel et al., 2013). The 2D seismic model of an elastic and isotropic medium in this thesis is making use of the `ewefd2d` modelling code in the Madagascar software, freely available in the archives of the Madagascar project. In Appendix A.1, the utilisation of the 2nd-order temporal and 8th-order spatial accurate `ewefd2d` modelling code in Madagascar is explained and used scripts for running the seismic model are provided.

5.2.1 Discretization of the modelling code

The `ewefd2d` modelling code is using a stress-stiffness formulation on a regular grid. In the framework of linear elasticity, the following constitutive relationship between stresses and strains is defined (Aki and Richards, 2002):

$$\tau_{ij} = c_{ijkl}\epsilon_{kl} \tag{5.1}$$

Where τ_{ij} is the second rank stress tensor, c_{ijkl} is the fourth-order stiffness tensor, ϵ_{kl} is the strain tensor describing the deformation of the continuum medium as follows:

$$\epsilon_{kl} = \frac{1}{2}(\partial_k u_l + \partial_l u_k) \tag{5.2}$$

A Cartesian geometry is assumed for the 2D isotropic and elastic seismic model where the x- and z-axes are represented by directional indices i, j, k and l, being 1 or 2. Because of symmetry properties in 3D stress and strain tensors, only 36 independent parameters among the 81 elastic coefficients are considered in the fourth-order stiffness tensor. By assuming only positive strain energy this leads to a further reduction to 21 independent parameters for a general anisotropic medium. In the special case where only a 2D isotropic medium is considered the stiffness tensor c_{ijkl} can be defined as a stiffness matrix c_{ij}. Following the derivation of the 3D isotropic stiffness matrix by Thomsen (1986), the 2D isotropic stiffness matrix can be written in a 3×3 symmetric form:

$$c_{ij} = \begin{bmatrix} c_{11} & c_{12} & 0 \\ c_{12} & c_{11} & 0 \\ 0 & 0 & c_{33} \end{bmatrix} \tag{5.3}$$

All non-zero components in the stiffness matrix are related to the Lamé constants λ and μ, and to the bulk modulus K, resulting in: $c_{11} = \lambda + \frac{2}{3}\mu$, $c_{33} = \mu$ and $c_{12} = c_{11} - 2c_{33} = \lambda - \frac{4}{3}\mu$.

Following the discretization of Weiss and Shragge (2013), Equations 5.1 and 5.2 have been given an numerical implementation by specifying computational mesh and a numerical discretization scheme. The discretized computational grid has the dimension of $n_x \times n_z$ and using n_t time steps. The continuous elastic wave field displacements are at given locations represented by the following equations:

$$\partial_x u_j \approx D_x[u_j^{p,r|n}] = \frac{1}{\Delta x}\sum_{\alpha=1}^{4} W_\alpha (u_j^{p+\alpha,r|n} - u_j^{p-\alpha,r|n}) \tag{5.4}$$

Where $D_x[\cdot]$ is a compact centred difference operator, p, r and n are the integer counters with the size of the model dimension and W_α are polynomial weights given by $\mathbf{W} = [\frac{+4}{5}\ \frac{-1}{5}\ \frac{+4}{105}\ \frac{-1}{280}]$. The spatial difference operator in the z-direction is specified similarly:

$$\partial_z u_j \approx D_z[u_j^{p,r|n}] = \frac{1}{\Delta x}\sum_{\alpha=1}^{4} W_\alpha (u_j^{p,r+\alpha|n} - u_j^{p,r-\alpha|n}) \tag{5.5}$$

Both discretizations of continuous wave field displacements are used for derivatives of the elastic wave (Equation 3.1). A standard second-order accuracy approximation is used for the second time derivative:

$$\partial_{tt}^2 u_j \approx D_{tt}[u_j^{p,r|n}] = \frac{1}{\Delta t^2}(u_j^{p,r|n+1} - 2u_j^{p,r|n} + u_j^{p,r|n-1}) \tag{5.6}$$

These difference operators specify a time-stepping scheme to calculate wave field displacements in media throughout the model domain. The difference operators are inserted into the stress-strain relations and rearranging terms leads to a finite-difference scheme for the forward time step of the unknown wave field, $u_j^{p,r|n+1}$, using values of the current and previous time steps, $u_j^{p,r|n}$ and $u_j^{p,r|n-1}$ and representing the 2nd order accuracy. For the spatial dimension, with 8th order accuracy, the stencil points of the neighbouring points of $u_j^{p,r|n}$ are used in x- and z-directions.

5.2.2 Model descriptions

Throughout this chapter, several seismic models will be discussed to show how elastic wave propagation in a 2D isotropic media is modelled with a constant emphasis on the COSC-1 borehole. These models

are summarised in Table 5.1, where grid dimensions, sampling, source and boundary information is provided for each individual model. Numerical stability and minimum grid dispersion have been tested and validated for all seismic models according to Equations 3.14 and 3.15.

Two seismic models will be presented in this section; a simplified 3 layer model and the final model which represents the COSC-1 borehole. Not every model will be discussed in this section, for these seismic models is referred to Appendix A.2. These seismic models deal with the boundary implementation for homogeneous and horizontal homogeneous situations.

Table 5.1: Grid dimension, sampling, source and boundary information of models used in this thesis. Ref. is referring to the description of the model within the text. Wavelet options are R (Ricker) for wavelet type and used frequency. Boundary options are ab (absorbing boundary) and fs (free surface).

Model		*Grid dimension*		*Sampling*			*Source*			
No.	Layers	$n_x \times n_z$	n_t	Δx [m]	Δz [m]	Δz [ms]	Wavelet	Depth [m]	Boundary	Ref.
1	3	3001 × 1244	8601	2	2	0.1	R50Hz	0.01	ab	5.2
2	1	1501 × 1001	3001	2	2	0.1	R50Hz	0.01	ab	A.2
3	1	1501 × 1001	3001	2	2	0.1	R50Hz	0.01	ab, fs	A.2
4	1244	3001 × 1244	8601	2	2	0.1	R50Hz	0.01	ab	A.2
5	1244	3001 × 1244	8601	2	2	0.1	R50Hz	0.01	ab, fs	A.2
6	1244	3001 × 3244	8601	2	2	0.1	R50Hz	4000.01	ab	5.2

5.2.3 Model implementation

3 layer model

The first model (Model 1 in Table 5.1) is used to test the `ewefd2d` modelling code and to identify converted waves as a function of offset. A three layer model is considered where the layers resemble important lithological units in the COSC-1 borehole: Layer 1 is a calc-silicate gneiss (v_p = 6358 m/s, v_s = 3653 m/s, ρ = 2.726 g/cm^3), Layer 2 is an amphibolite (v_p = 7118 m/s, v_s = 3578 m/s and ρ = 3.004 g/cm^3) and Layer 3 is a mica schist (v_p = 5121 m/s, v_s = 2726 m/s and ρ = 2.788 g/cm^3). As a result of the used input model (Figure 5.3) the R_c between the interface of Layer 1 and 2 is 0.1046 for the P-wave incidence and 0.0382 for the S-wave incidence. For the interface between Layer 2 and 3 the R_c is -0.1992 for the P-wave incidence and -0.1716 for the S-wave incidence. Good reflectivity is expected at the interface between calc-silicate gneiss and amphibolite for the P-wave, but lower reflectivity for the S-wave arrival. Reflectivity is significantly higher for the interface between amphibolite and mica schist, for the P-wave as well as for the S-wave.

Figure 5.4 shows wave field snapshots of Model 1 and identifies reflection and transmission of body waves and associated converted waves. Strong amplitude P- and S-waves are identified (Figure 5.4a). After propagation of both wave fields, waves are reflected and transmitted at the calc-silicate gneiss/amphibolite interface resulting in clear transmitted and reflected P- and S-waves (Figure 5.4b). Additionally, converted waves are also transmitted and converted for $P-S$ and $S-P$ with varying amplitude as a function of angle from the shot point. At the low reflective amphibolite/mica schist interface are still strong reflections observed (Figures 5.4c-d) from both body waves and converted waves. The strong P-wave hits the lower boundary of the model and gets attenuated by the implemented absorbing boundary, observing a low amplitude P-wave reflection from the boundary.

The raw and processed model response of the Model 1 is shown in Figure 5.5. Processing steps applied to the raw model response are trace balancing (0-860 ms), spherical divergence correction ($\sqrt{t}$) and adding bias (0.02). The raw model response in the left panel of Figure 5.5 contains not well defined reflection, the processed model response in the right panel makes it possible to identify 6 reflections indicated by numbers: 1 and 5 are P-wave reflections at the two interfaces; 2, 3 and 6 are converted waves; and 4 is the S-wave reflection at the calc-silicate gneiss/amphibolite interface.

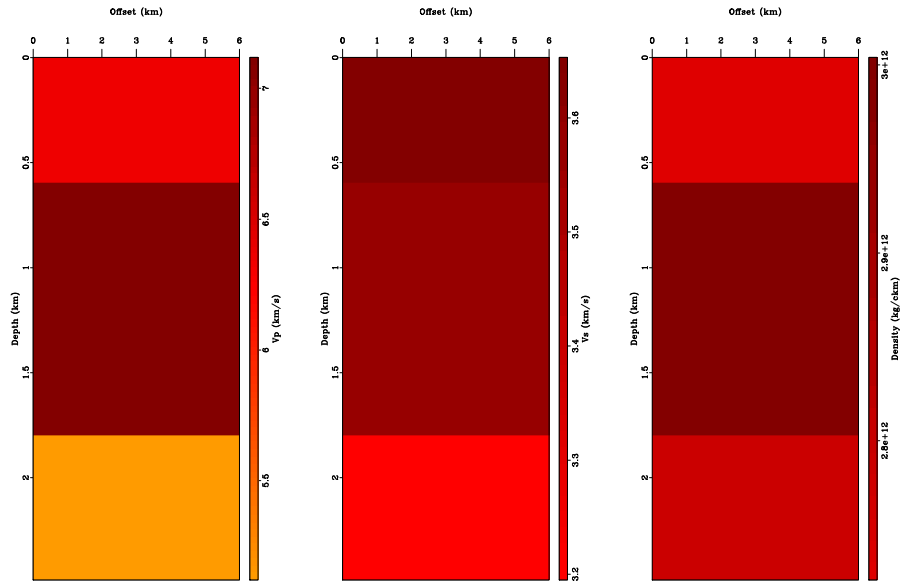

Figure 5.3: Input parameters of the 3 layer model (Model 1 in Table 5.1).

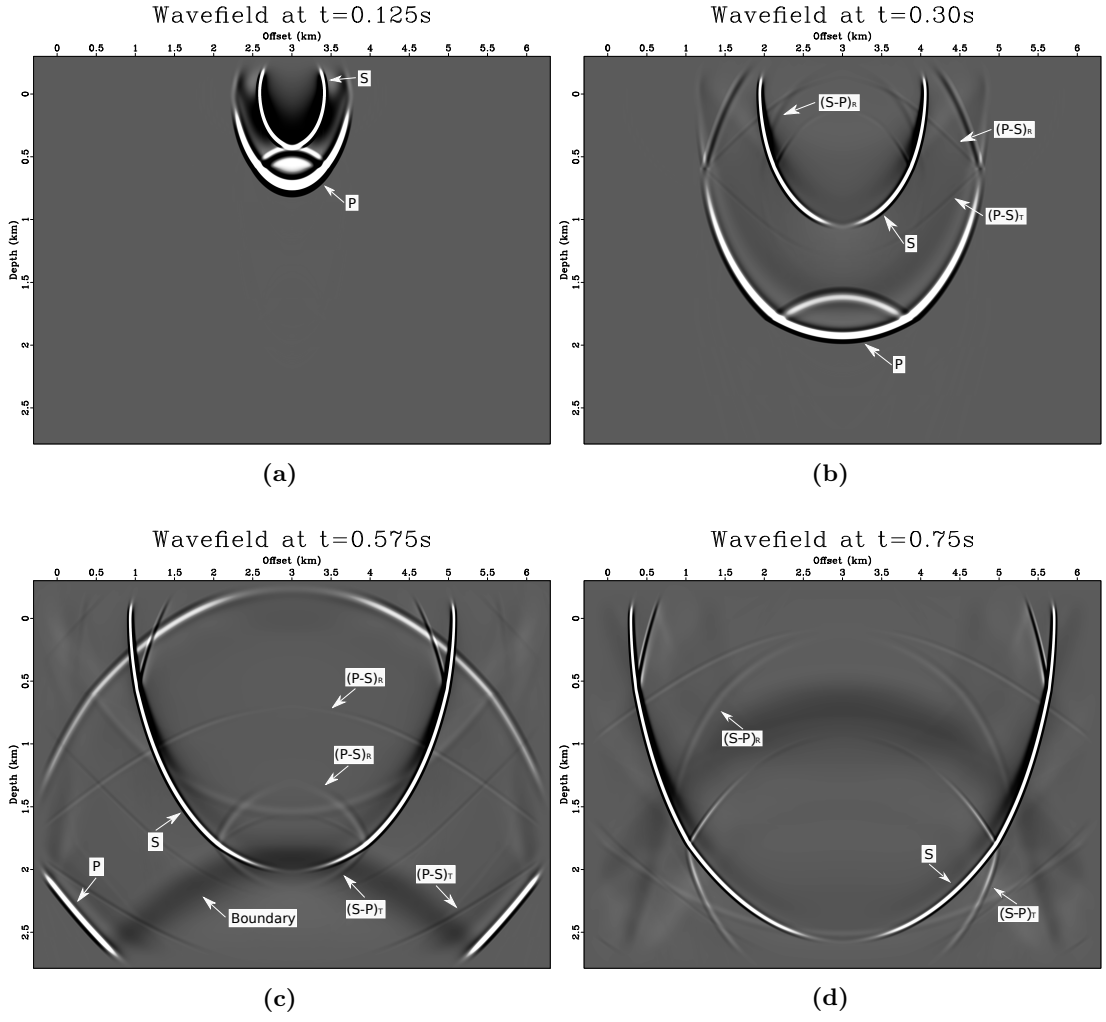

Figure 5.4: Wave field snapshots of a 3 layer model (Model 1 in Table 5.1) at time: a) $t = 0.125$ s, b) $t = 0.375$ s, c) $t = 0.575$ s and d) $t = 0.75$ s. In the snapshots are the transmitted (T) and reflected (R) body- and converted waves indicated.

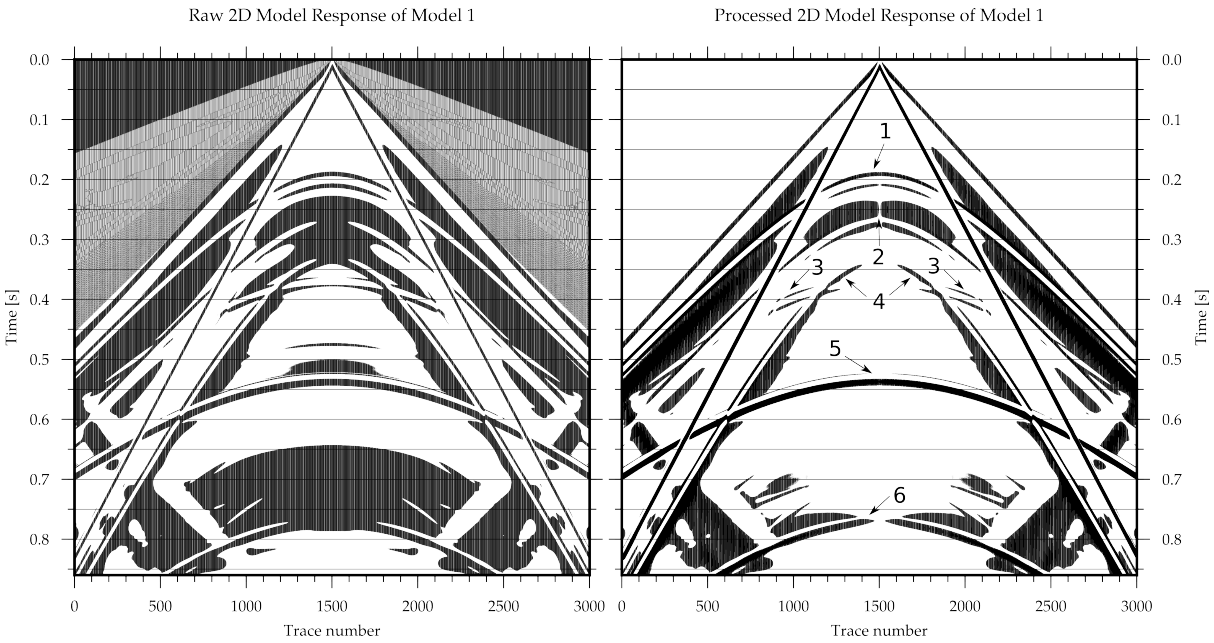

Figure 5.5: Model response of the 3 layer model (Model 1 in Table 5.1). The left panel is displaying the raw model response after 2D elastic and isotropic finite-difference modelling and the right panel is displaying the model response after processing. The numbers represent the following reflections: 1 and 5 are P-wave reflections at the two interfaces; 2, 3 and 6 are converted waves; and 4 is the S-wave reflection at the second interface.

The interface between calc-silicate gneiss/amphibolite is theoretically an excellent reflective boundary and clear reflections of the body- and converted waves are observed, and can potentially be seen in the actual model of the COSC-1 borehole. The R_c of the amphibolite/mica schist interface is high and also clear reflections are observed from the body- and converted waves in this simplified model. Two types of wave conversion are observed in the model response at the first interface, limitation in model time made it unable to see arrivals of the S-wave reflection and more than one converted wave. Amplitude distributions of the body wave are equal of the complete wavefront, where the zero-offset of the converted waves has very low to zero amplitude.

Model of the COSC-1 borehole

The 2D model of the COSC-1 borehole is performed to acquire the zero-offset trace and analyse wave conversion as an offset function. The treatment of the surface is an important parameter in seismic modelling. The `ewefd2d` modelling code provides an implementation of absorbing and free surface boundary conditions for the surface. Reflected waves from the surface by using absorbing boundaries of 150 grid points are interfering with the synthetic zero-offset trace, therefore a free surface implementation was required, but during testing, problems were encountered. The free surface causes a high degree of dispersion at the surface and critically interfering with the waveforms. Direct use of the free surface is therefore not possible, so a model is configured by adding a thick homogeneous layer above the input model of the COSC-1 borehole. The effect of the absorbing boundary and free surface is described by testing four different types of models and comparing them to each other in Appendix A.2; Figure B.1.

The model of the COSC-1 borehole (Model 6 in Table 5.1) is defined by the v_p, v_s and density values of the FWS logging results and core density measurements, similar to the 1D seismic model. The data points averaged over 50 cm and the first 103 m is approximated by $v_p = 5200$ m/s, $v_s = 3000$ m/s and $\rho = 2.68$ g/cm^3. Missing values of the v_s over depth due to picking difficulties are approximated by Equation 3.4. The input values are assumed to be constant with offset, leading towards a horizontal homogeneous model (Figure 5.6). To avoid dispersion problems of the free surface and reflections from the surface as

a result of the absorbing boundary conditions, the homogeneous layer is 4 km thick and added above the model parameters of FWS logging results. Source and receivers are placed at a depth of 4000.01 m, to simulate a 0.1 m deep source and receiver location. Within 0.86 s wave field simulation, no reflections from the homogeneous layer and surface were recorded at the receivers (Figure 5.7). The propagating wave field shows the P- and S-wave spreading with time inducing clear reflections with varying amplitude at the sharp interfaces in the model, but wave conversion is not visible as such previously shown in Model 1.

The raw and processed model response of Model 6 (Figure 5.8) shows the reflections within the model, before and after applying frequency filtering (0-18-2500-12000 Hz), trace balance (0-860 ms), spherical divergence correction ($\sqrt{t}$) and adding bias (0.02). Similar to the wave field snapshot, the model response also doesn't show wave conversion. Distinct direct P- and S-wave arrival is observed and the highly vertical heterogeneous medium results in reflections with varying amplitude. It is known from the 3 layer model that wave conversion occurs in the seismic model and also results in clear reflections, but it requires more model testing and processing to observe these reflections in either the wave field or the model response which represents the complex structure of the COSC-1 borehole.

5.3 Comparison of the modelling results

The synthetic seismogram of `FWVS2` after convolution with a 50 Hz minimum phase wavelet (Figure 5.2e) is compared to the zero-offset trace of the 2D elastic and isotropic finite-difference model with source generation by a 50 Hz Ricker wavelet (Model 6; Figure 5.8). Prior to plotting is the zero-offset trace of the 2D model reversed in polarity, while the impedance in velocity-stress modelling is calculated reversely, $Z = Z_1 - Z_2/Z_1 + Z_2$. The comparison is made to examine the difference between the two types of seismic modelling. Furthermore, a synthetic seismogram after convolution with a 50 Hz Ricker wavelet is examined to show the differences when the same wavelet is used in 1D and 2D seismic modelling. In Figure 5.9 three synthetic traces are presented; left the 1D synthetic seismogram of the 50 Hz minimum phase wavelet type, in the middle the 1D synthetic seismogram of the 50 Hz Ricker wavelet type and right the 2D finite-differences model.

First will be focussed on the comparison between the synthetic seismogram of the 50 Hz minimum phase wavelet type and the zero-offset trace of the 2D model. Both input models are based on the FWS logs so the synthetic traces bear similar reflections. Significant reflections at 0.20, 0.24, 0.26, 0.51, 0.53, 0.55, 0.56, 0.65, 0.77, 0.78 and 0.79 s are present in both seismic models, however the reflections in the 2D model are continuously delayed by 0.01 s. Differences also exist, the first striking feature is the extremely high amplitude at 0.01 s in the 2D model, caused by excitation of the source, which is non-existent in the 1D seismic model. The two similar reflections occurring at 0.07 and 0.09 s in the 1D model and at 0.06 and 0.11 s in the 2D model have reversed amplitudes, in the 1D model is the second reflection of high amplitude and in the 2D model the first. An explanation for this feature could be the difference in source wavelet, changing the amplitude during convolution and modelling. In general is the earth response better approximated by a minimum phase wavelet, where the zero-phase Ricker wavelet adds the approximation of symmetry in the earth response. Another difference is the general reflectivity between TWT of 0.26 and 0.51 s. Several reflections are not correlating well. In the 2D model are also multiples generated, the observation of strong multiple reflections could, therefore, be a possible explanation for these features.

When the same 50 Hz Ricker source wavelet is used for the 1D convolutional modelling and 2D elastic and isotropic finite-difference modelling a poorer correlation is found. Larger and but now negative time shifts are observed ($\sim$0.015 s) therefore give rise to reflectivity earlier in time compared to the synthetic

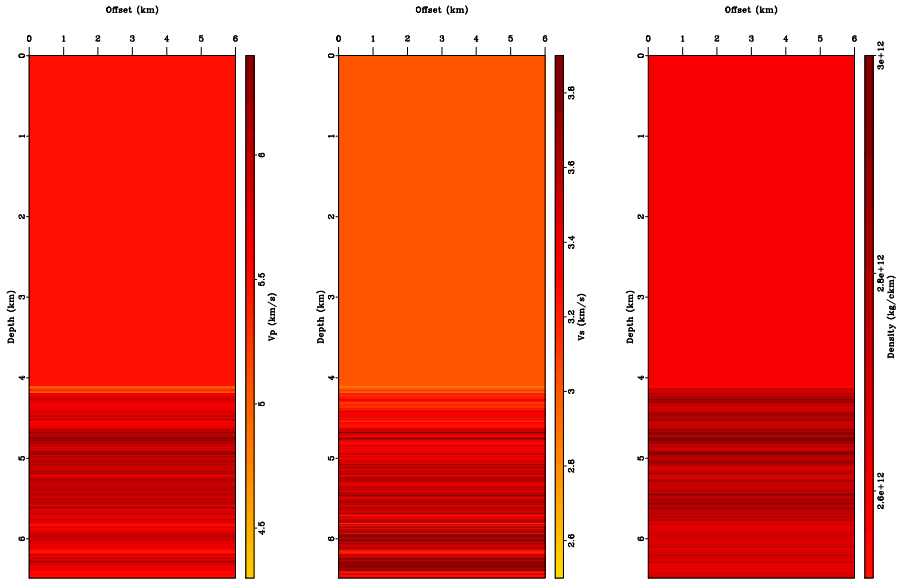

Figure 5.6: Input parameters of the model representing the COSC-1 borehole (4-6.48 km) with a 4 km thick homogeneous layer above (Model 6 in Table 5.1).

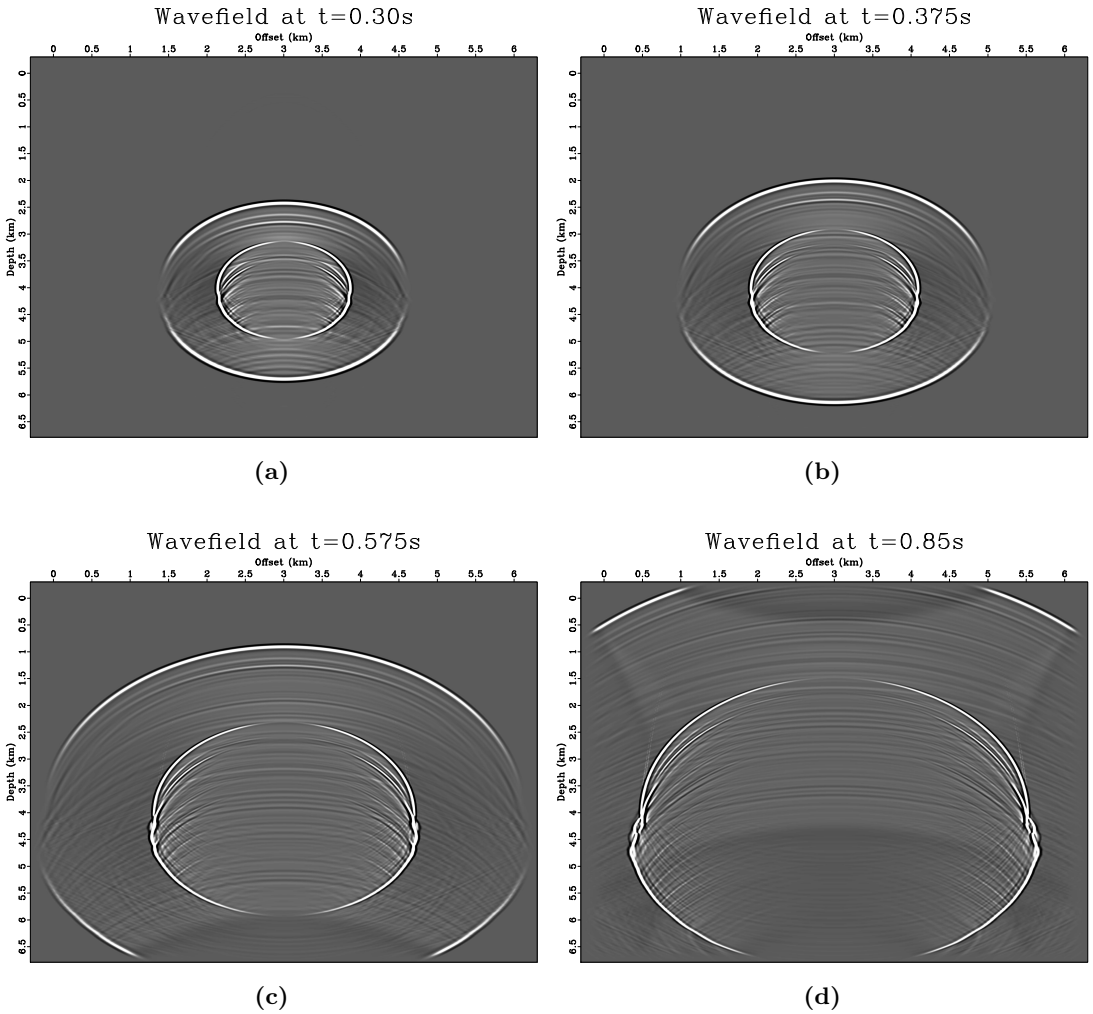

Figure 5.7: Wave field snapshots of the model representing the COSC-1 borehole (4-6.48 km) with a 4 km thick homogeneous layer above (Model 6 in Table 5.1) at time: a) $t = 0.30$ s, b) $t = 0.375$ s, c) $t = 0.575$ s and d) $t = 0.55$ s. Source is at 3 km offset and approximately 4 km depth.

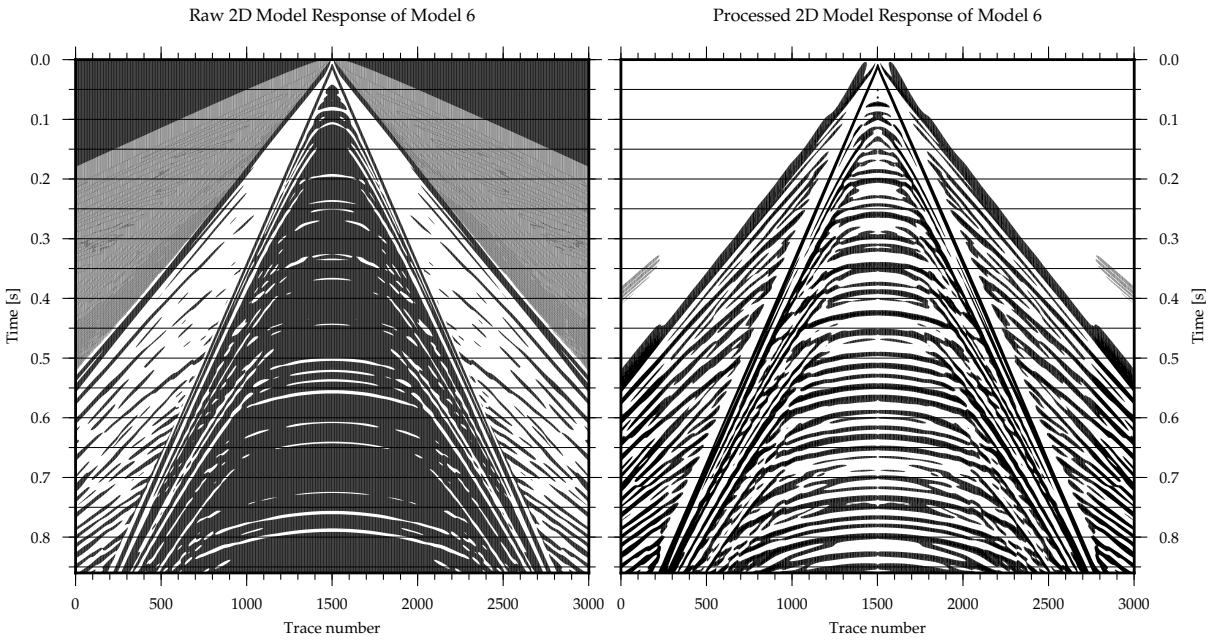

Figure 5.8: Model response of the model representing the COSC-1 borehole with a thick homogeneous layer above (Model 6 in Table 5.1). The left panel is displaying the raw model response after 2D elastic and isotropic finite-difference modelling and the right panel is displaying the model response after processing.

seismogram after convolution with a 50 Hz minimum phase wavelet. Despite the difference in wavelet type between 1D and 2D modelling, a better result is obtained than by using the same 50 Hz Ricker wavelet. The difference between the minimum phase and zero phase wavelet type is observed as critical in the 1D convolutional modelling, deciding to continue with the 50 Hz minimum phase 1D model while it approximates the surface seismic better. The simplicity of the wavelet type and resemblance to the synthetic seismogram in 2D modelling, justifying the choice of the 50 Hz Ricker wavelet.

Despite the differences, throughout the borehole many reflections are correlating between the 1D and 2D model, give rise to confidence in the modelling methods. The 2D finite-differences model uses, in addition to the v_p and density information, also the v_s. In reality is the shear wave also present and 2D finite-difference modelling results in a more advanced approximation of the seismic response in the COSC-1 borehole, therefore is the 2D zero-offset trace more reliable and better to compare to other seismic results. A comparison of the 1D synthetic traces and the 2D zero-offset trace with the surface seismic is required to assess the fit of both models or the surface seismic to the logging results.

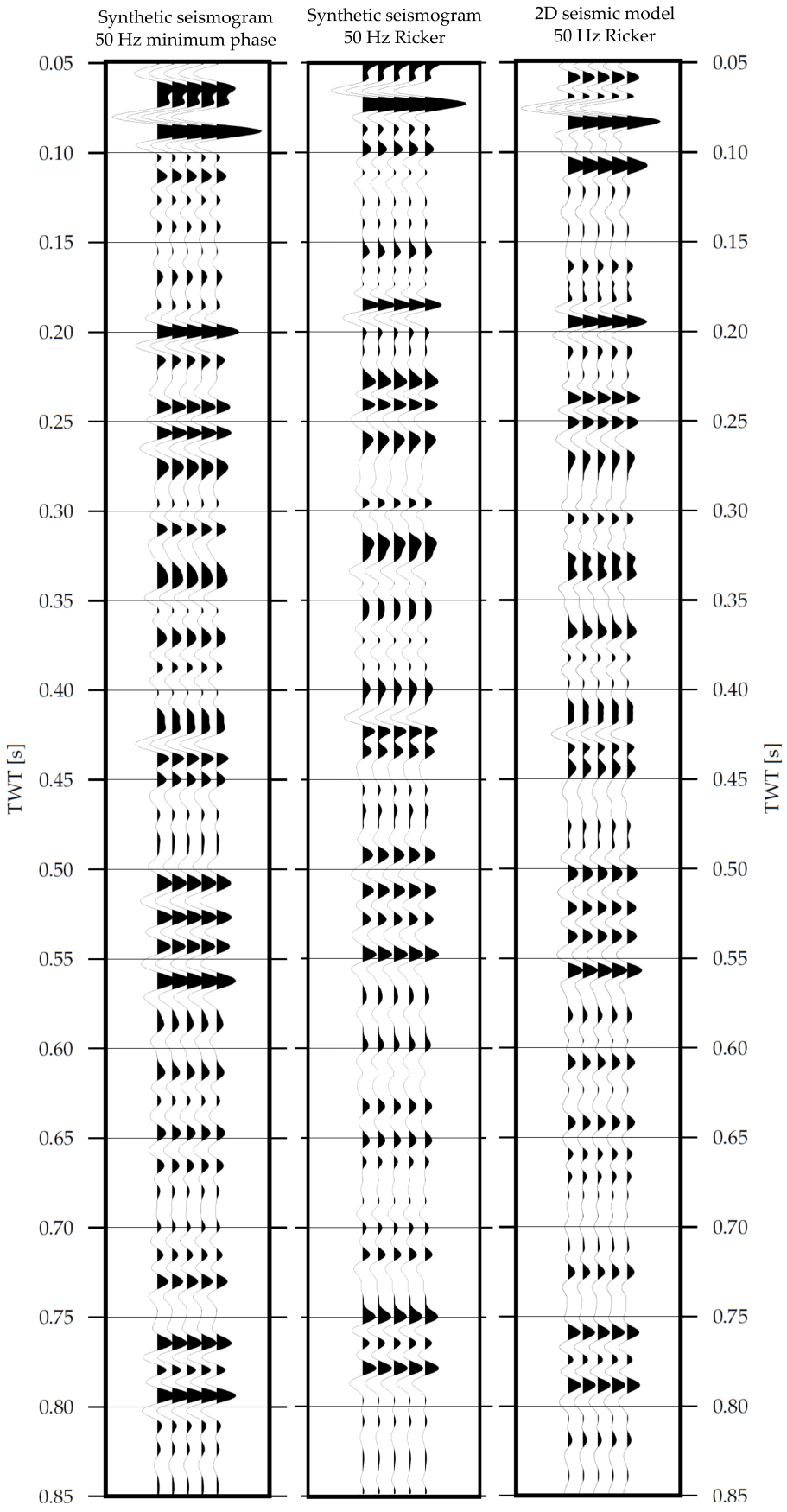

Figure 5.9: Comparison of the synthetic seismograms of `FWVS2` after convolution with a 50 Hz minimum phase wavelet (left panel) and a 50 Hz Ricker wavelet (middle panel) to the zero-offset trace of the 2D elastic and isotropic finite-differences model with source generation by a 50 Hz Ricker wavelet (right panel).

CHAPTER 6

Discussion

The results presented in the previous chapters have implications on the crustal composition and reflectivity within the COSC-1 borehole. In this chapter, the well-logs are validated with comparative studies and put into the context of the COSC-1 borehole and Earth's middle and lower crust. Section 6.1 will focus on the comparison of the logging results and geochemical data to provide information on the mineral content within the borehole. In Section 6.2 the core measurements, ZVSP and surface seismic will be discussed and compared. Thereafter, a discussion will follow with a focus on the crustal seismic reflectivity.

6.1 Crustal composition

Knowledge about the crustal composition from outcrops and core samples enhances the understanding of crustal generation and evolution through geologic time (Christensen and Mooney, 1995). Several geophysical- and sample-based studies are published on this topic and have derived the bulk composition of the crust in a global perspective (Christensen and Mooney, 1995; Rudnick and Fountain, 1995; Hacker et al., 2015). Whereas outcrops of upper crustal structures are abundant, the in-situ composition of the middle and lower crust are more difficult to determine and are estimated from limited exposed terrains, xenoliths and geophysical data (Hacker et al., 2015). Erosion and exhumation in the central Swedish Caledonides brought structures of middle crustal origin to the surface, enabling the study of relict crustal structures that formed during orogeny (Hedin et al., 2012) and by drilling the COSC-1 borehole a continuous section of the crustal composition can be studied and compared with geophysical data.

The core of the COSC-1 borehole is scanned with the Minalyze CS XRF scanner by the Swedish company Minalyze AB. The data set contains geochemical data for several oxides; Al_2O_3, SiO_2, S, K_2O, CaO, TiO_2 and Fe_2O_3. The data is continuously measured and interpolated over a 10 cm interval to produce discrete data points. The core extracted from the COSC-1 borehole is fragmented, leading to data points with extremely low mass fractions which cannot be used for correlation. These data points are removed and afterwards a 75 data point moving average filter is used for correlation and displaying purposes prior to plotting. The geochemical data is presented in Figure 6.1.

The mass fraction distribution of various geochemical components with depth reveals the following observations. The major element composition within the COSC-1 borehole consists mainly SiO_2 (40-90 wt%), additionally proportional amounts of Al_2O_3 (4-18 wt%), CaO (0.5-33 wt%) and Fe_2O_3 (1-12 wt%) are encountered and minor amounts of S (0.1-2.3 wt%), K_2O (0.1-4.9%) and TiO_2 (0.2-1.6 wt%). Most elements display a highly variable trend with depth, but between 1050-1450 m the contents of Al_2O_3, SiO_2, CaO, TiO_2 and Fe_2O_3 show less variable behaviour, coinciding with constant and thick units of gneiss, transitioning from amphibolite, to calc-silicate and eventually to felsic gneiss. Whereas

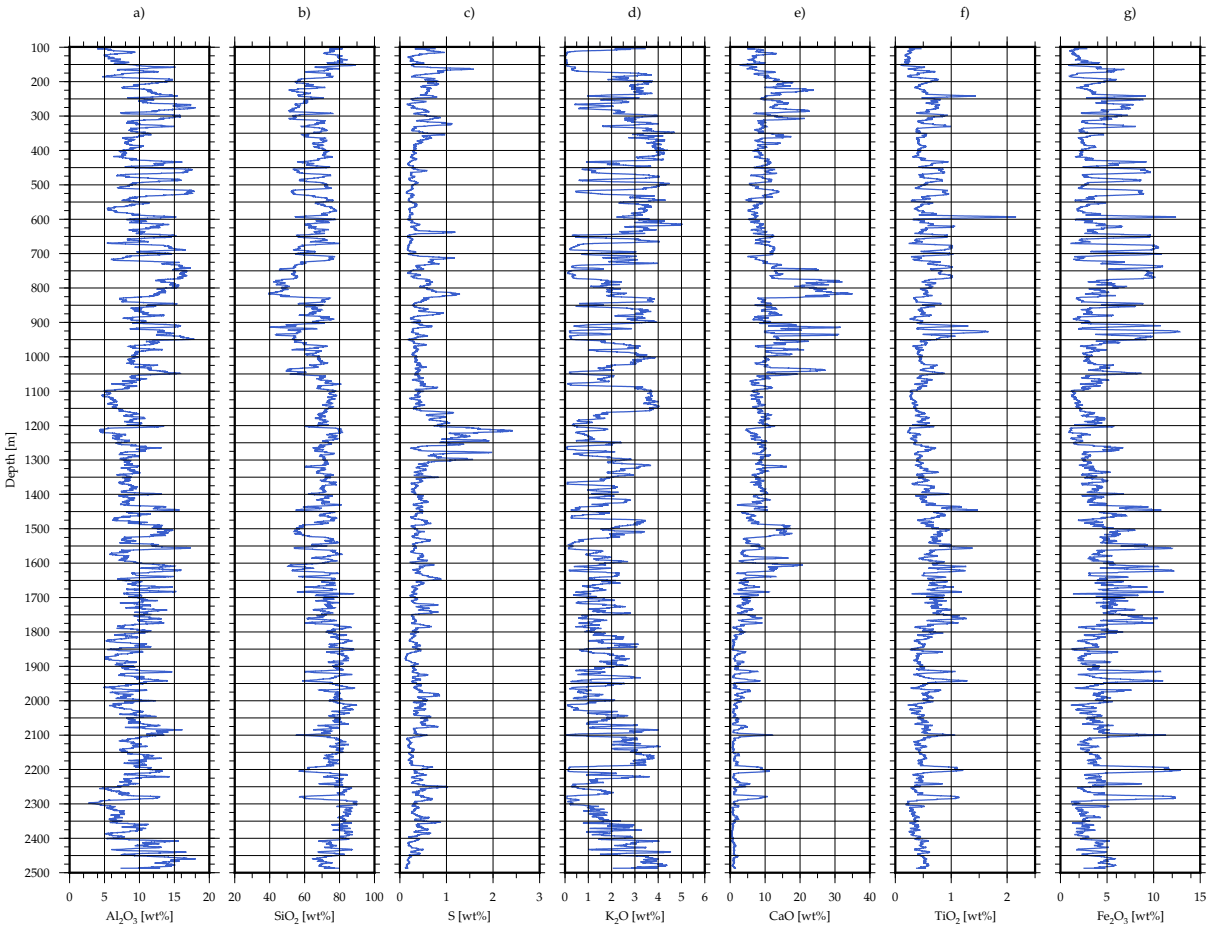

Figure 6.1: The mass fraction of several geochemical components with depth within the interval of 100-1600 m measured by the Minalyze CS XRF scanner. a) Al_2O_3, b) SiO_2, c) S, d) K_2O, e) CaO, f) TiO_2 and g) Fe_2O_3. The data points originate from an interpolation over 10 cm of continuous measurement, removal of physically unreal values and applying a 75 data points moving average.

the sulphur content is generally small (0.1-1 wt%), it exhibits increased amounts in the depth range of 1050-1450 m with a maximum of 2.36 wt% at 1210 m. The elemental composition shows a general trend with depth, which is important for the constraint of lithology as a function of depth. General trends of the Al_2O_3, SiO_2 and CaO content with depth are discussed in detail. The Al_2O_3 and CaO content is decreasing with depth, where the Al_2O_3 content is decreasing from approximately 10 wt% to 7 wt% and the CaO content shows a clear decrease from 10 wt% to nearly 0.5 wt% at total depth. In contrast, the SiO_2 content shows a gradual increase with depth, from 60 wt% to 80 wt%. In contrast, the sulphur, TiO_2 and Fe_2O_3 do not show general trends of increasing or decreasing amounts as a function of depth. Additionally, high values of Al_2O_3 and CaO are anticorrelated with SiO_2; i.e., relatively high values of Al_2O_3 and CaO contents are accompanied by relatively low values of SiO_2 contents and the other way around. A similar effect is seen by comparing the SiO_2 and Fe_2O_3 content, but the Fe_2O_3 content is a bad indicator for a transitioning environment. These trends have important implications on the change in lithology. The increase in SiO_2 content with depth has a direct relation to the decreasing v_p/v_s ratio in (Figure 4.6). The felsic rocks contain more SiO_2 than mafic rocks, and comprises the felsic gneisses, mica schist and meta-sandstones in the borehole. At a depth of 1700 m, a transition is interpreted (Lorenz et al., 2015a), supported by the change from gneisses into lower grade meta-sedimentary rocks. The gradual increasing SiO_2 is reflected by a decrease of v_p/v_s, which indicates a gradual transition to more felsic compositions at depth. Above the interpreted transition zone, successions of calc-silicate gneisses, amphibolites and meta-gabbros are encountered, which explains the elevated content of CaO

in the uppermost 1700 m of the borehole.

The geochemical and borehole geophysical data were compared in order to extract significant relationships between rock composition and log responses. All well-logs are containing data points every 0.1 m, leading toward an extensive data set which can be evaluated by statistical analysis. The Pearson's product-moment correlation coefficient and Spearman's rank correlation coefficient were computed to assess relationships between the well-logs. Pearson's product-moment correlation coefficient (R) is a measure of the linear correlation between two variables, X and Y, and is given by the following equation:

$$R = \frac{Cov[X,Y]}{\sqrt{Var[X] \cdot Var[Y]}} \tag{6.1}$$

Where $Cov[X,Y]$ is the sample covariance given by the following equation:

$$Cov[X,Y] = \frac{\sum_{i=1}^{n}(x_i - \overline{x})(y_i - \overline{y})}{n-1} \tag{6.2}$$

Where x_i and y_i are the entries of the variables, $\overline{x}$ and $\overline{y}$ are the sample mean of the variables and n is the number of samples. $Var[\cdot]$ is described by the sample covariance of the variable with itself.

Spearman's rank correlation coefficient (R_S) relationship can determine the non-linear correlation between two variables using a monotonic function:

$$R_S = 1 - \frac{6\sum_{i=1}^{n} d_i^2}{n(n^2-1)} \tag{6.3}$$

Where d_i is the rank correlation by taking the differences in the rank of the two variables.

Not every correlation found is significant, therefore the existence of the correlation has to proven. To evaluate the significance of R, a test statistic that follows the t-distribution is used. A confidence level of 95% ($\alpha = 0.05$) is mostly used in earth science (Borradaile, 2003). The following equation compares the test statistic with a tabled t-value according to the chosen confidence level and on the degrees of freedom designated as $(n-2)$:

$$\left|\frac{R\sqrt{(n-2)}}{\sqrt{(1-R^2)}}\right| \geq t_{\frac{\alpha}{2}} \tag{6.4}$$

Where the chosen two-tailed $t_{\frac{\alpha}{2}}$ is determined to be 1.960. Based on the high number of data points, the degrees of freedom is considered to be ∞.

The Pearson's product-moment correlation coefficient, Spearman's rank correlation coefficient and $t_{\frac{\alpha}{2}}$ were calculated using the density, v_p, v_s, v_p/v_s ratio, P-wave impedance (Z_p) and S-wave impedance (Z_s) together with the geochemical data (Table 6.1).

For calculating the correlation coefficient are the geochemical logs, core density log and well-logs used. Calculations are performed before averaging the data prior to plotting. The correlation coefficients are presented as they are acquired without processing and reveal correlations within a data set of 15732 to 22955 data points. Irregularities and outliers will be significantly reduced by applying averaging on the data set, but the overall trend is kept. Using the processed data results in an artificially enhanced correlation coefficients, therefore no averaging is applied. Data used in this section, with and without averaging, is presented in Appendix B; Figures B.1 and B.2. The used parameters for correlation are shown in Figure 6.2. Representing the parameters by box-and-whisker plots visualises the spread, skewness and outliers in the data. Note the high amount of outliers for all parameters as a result of high variability and irregularities.

The highest correlation coefficients are found with the density and v_p/v_s ratio ($|R| > 0.3$ and $|R_S| > 0.3$). Other properties have an intermediate correlation with elements, with the exception of very weak

Table 6.1: Degree of dependency between the XRF components and several acoustic properties; P-wave impedance, S-wave impedance and v_p/v_s ratio. Where n denotes the number of samples, R is the Pearson's product-moment correlation coefficient, R_S is Spearman's rank correlation coefficient and $t_{\frac{\alpha}{2}}$ is the critical value for the significance of correlation. $t_{\frac{\alpha}{2}}$ for a significant correlation with 95% certainty is determined to be 1.960.

Component	n	R	R^2	R_S	$t_{\frac{\alpha}{2}}$
Correlation between the geochemical components and density					
Al_2O_3	18575	0.1730	0.0299	0.2056	23.94
SiO_2	22957	-0.2670	0.0713	-0.3279	41.99
S	21173	-0.0126	0.0002	0.0171	1.82
K_2O	22954	-0.0953	0.0090	-0.0841	14.50
CaO	22955	0.24408	0.0596	0.3813	38.13
TiO_2	22955	0.1922	0.0369	0.2431	29.67
Fe_2O_3	22955	0.2057	0.0423	0.2234	31.84
Correlation between the geochemical components and v_p					
Al_2O_3	18575	0.1276	0.0163	0.1464	17.53
SiO_2	22957	-0.2107	0.0443	-0.2413	32.65
S	21173	-0.0163	0.0003	0.0432	2.38
K_2O	22954	-0.1565	0.0245	-0.1910	24.00
CaO	22955	0.2109	0.0445	0.3003	32.68
TiO_2	22955	0.1716	0.0294	0.1808	26.39
Fe_2O_3	22955	0.2026	0.0410	0.1779	31.34
Correlation between the geochemical components and Z_p					
Al_2O_3	18575	0.1942	0.0377	0.2098	26.99
SiO_2	22957	-0.3090	0.0955	-0.3343	49.23
S	21173	-0.0182	0.0003	0.0413	2.65
K_2O	22954	-0.1727	0.0298	-0.1903	26.57
CaO	22955	0.2960	0.0877	0.3976	46.96
TiO_2	22955	0.2357	0.0555	0.2574	36.74
Fe_2O_3	22955	0.2673	0.0714	0.2458	42.02
Correlation between the geochemical components and v_s					
Al_2O_3	15732	-0.0331	0.0011	-0.0488	4.15
SiO_2	19451	0.1712	0.0293	0.1955	24.24
S	18130	-0.0317	0.0010	-0.0521	4.27
K_2O	19450	-0.3487	0.1216	-0.4087	51.88
CaO	19450	-0.1980	0.0392	-0.2475	28.17
TiO_2	19450	0.0178	0.0003	-0.0224	2.48
Fe_2O_3	19450	0.0835	0.0070	0.0413	11.68
Correlation between the geochemical components and Z_s					
Al_2O_3	15732	0.0928	0.0086	0.0739	11.70
SiO_2	19451	-0.0497	0.0025	-0.0208	6.94
S	18130	-0.0353	0.0012	-0.0458	4.75
K_2O	19450	-0.3313	0.1098	-0.3739	48.97
CaO	19450	0.0161	0.0003	-0.0013	2.25
TiO_2	19450	0.1328	0.0176	0.1099	18.69
Fe_2O_3	19450	0.1923	0.0370	0.1498	27.33
Correlation between the geochemical components and v_p/v_s ratio					
Al_2O_3	15732	0.1535	0.0236	0.1787	19.48
SiO_2	19451	-0.3182	0.1013	-0.3478	46.81
S	18130	0.0011	0.0000	0.0436	0.16
K_2O	19450	0.1285	0.0165	0.1588	18.08
CaO	19450	0.3396	0.1154	0.4205	50.36
TiO_2	19450	0.1192	0.0142	0.1518	16.74
Fe_2O_3	19450	0.0965	0.0093	0.1142	13.52

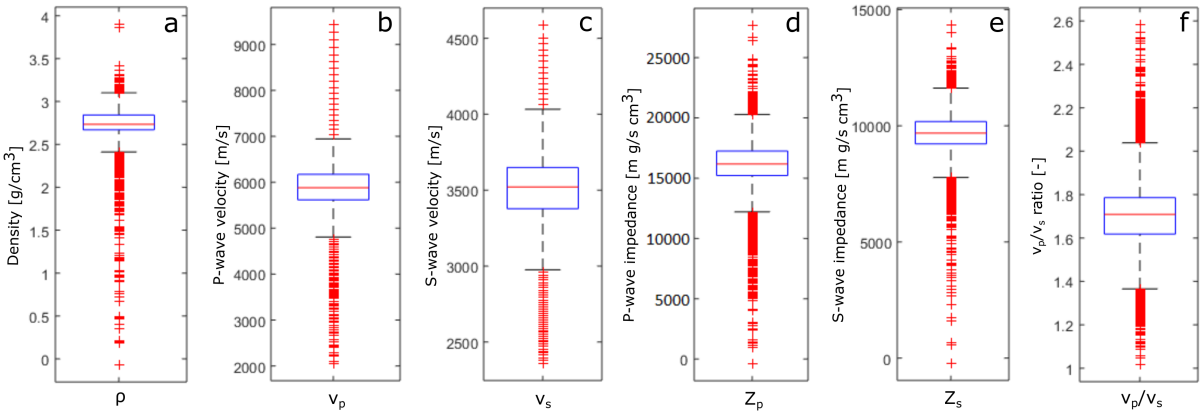

Figure 6.2: Boxplots of the parameters used for correlation with the elements: a) density, b) v_p, c) v_s, d) Z_p, e) Z_s and f) v_p/v_s ratio. The boxes represent the lower quartile and upper quartile. The median is represented by the horizontal red line in the boxes. The whiskers extending above and below the box represent the values $\pm 2.7\sigma$ and 99.3% coverage of normally distributed data. The outliers are shown as + above and below.

correlations of physical properties with the S and K_2O content. In general, all correlations are significant, due to high level of significance $t_{\frac{\alpha}{2}}$, only the correlation of the sulphur content and Z_p is considered insignificant. The high correlation coefficients between density and geochemical components are obvious because rocks are composed by summing each of the components, directly relating to density. A strong negative correlation is observed with the SiO_2 content and positive correlations with the Al_2O_3, CaO, TiO_2 and Fe_2O_3 content. Density is also positively correlated with acoustic properties, the Z_p and Z_s have in general a higher correlation than the correlation of only v_p and v_s. Due to the high correlation between the density and elements, the correlation with the impedances is improved. By analysing the v_p/v_s ratio, good correlations are found without the direct relation between density and geochemical components. The v_p/v_s ratio shows a negative correlation with the SiO_2 content (R = -0.3182 and R_S = -0.3478) and positive correlation with the CaO content (R = 0.3396 and R_S = 0.4205). These correlation coefficients may appear to be low, but contributes nevertheless to the understanding of geochemical composition in relation to acoustic properties. Data of the geochemical and acoustic logs are used without removing outliers and applying processing, giving rise to a scattered distribution and lowering the correlation coefficient significantly. However, the geochemical and acoustic data appear to have a strong visual correlation when presented in cross-plots (Figure 6.3) and is therefore considered as valuable information.

The cross-correlations of CaO in Figure 6.3a-c shows the distribution with v_p/v_s ratio, Z_p and Z_s. Cross-correlations show three distributions of the data. The first distribution is identified with a very low CaO content (0-3 wt%) and the second distribution with a moderate CaO content (5-13 wt%). The remaining data points are mainly distributed with a higher CaO content and spread over a large range for the acoustic property. The first and second distribution cannot be clearly differentiated by Z_p and Z_s due to similar values for these properties, but better slightly better for the Z_p. The small differences in Z_p and Z_s are accounted for when looking at the v_p/v_s ratio in Figure 6.3c. The density is not playing a role and differences are amplified by looking at the ratio of the two body wave velocities. The data population with very low CaO content is identified by low v_p/v_s ratio (~1.60), after comparing these results with the core description it becomes clear these values are from gneisses and meta-sandstones, mainly in the lower part of the borehole. The second distribution is identified by a moderate CaO content and a higher v_p/v_s ratio (~1.73), related to amphibolites (hornblende-bearing mafic rocks) in the upper part of the borehole. The third distribution is identified with a very high CaO content (>16 wt%) and high v_p/v_s ratio (>1.72) and slightly overlapping with the second distribution. Core samples with a very high CaO content are related to marbles and impure marbles, mainly occurring between 750 m and 1050

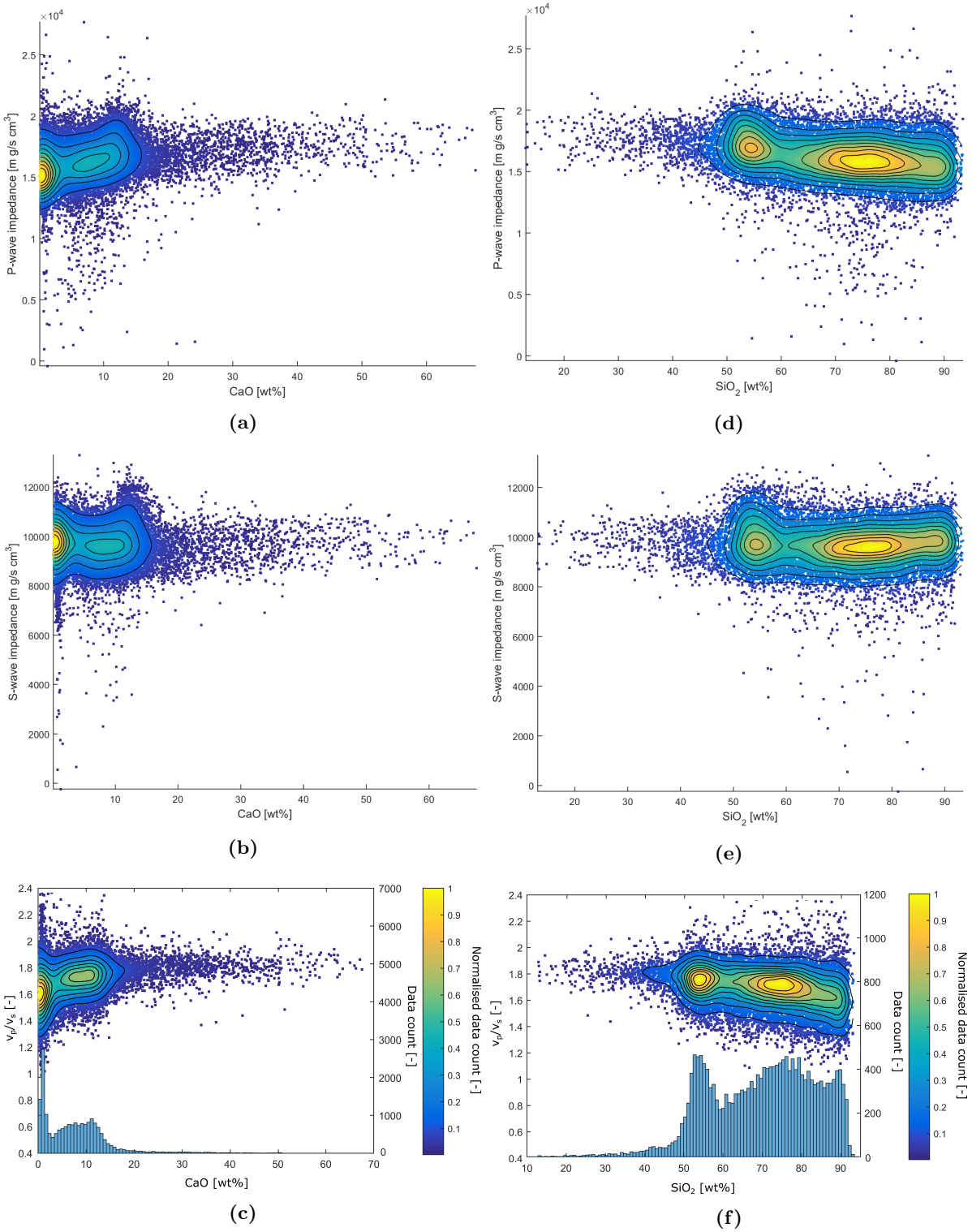

Figure 6.3: The cross-plots between the mass elements CaO (a, b and c) and SiO_2 (d, e and f) and acoustic properties: a) and d) Z_p, b) and e) Z_s and c) and f) v_p/v_s. The cross-plots are obtained by calculating 2D histograms. The colour bar represents the number of data points normalized by the maximum number of data points in one bin. The histograms (bin size = 100) in c and d show the data count of the relevant elements.

m depth. A similar, but negative, correlation is found for the SiO_2 content, however, not as clear as for the CaO content. Figure 6.3d-f shows the cross-correlations of the SiO_2 content. The existence of the three distributions is supported by the histogram of the CaO content (bin size = 100; Figure 6.3c), showing the grouping of lithological units more accurately than the cross-plots irrespective to the v_p/v_s ratio. Note that the bin size will affect the described limits of the grouping. The majority of the rocks contain 1.3-2.0 wt% CaO representing felsic rocks. The second distribution and grouping occurs between 3.3-12.7 wt% CaO representing the mafic rocks but is significantly lower in data count and spanning a larger range of CaO content. The third distribution is almost negligible in contrast to the felsic and mafic rocks due to the large scattering but still make up for continuously occurring marbles and impure marbles. For the SiO_2 content (Figure 6.3f) similar distributions are found, however the data intensity of the v_p/v_s ratio between the felsic (62-89 wt% and ~1.71) and mafic (50-60 wt% and ~1.76) distributions is different; felsic rocks are having a higher v_p/v_s ratio, making it harder to separate them by v_p/v_s ratio. Again, the highest v_p/v_s ratio (>1.76) and lower SiO_2 content (<47 wt%) is accounted for by marbles and impure marbles. The histogram of the SiO_2 content (bin size = 100; Figure 6.3f) also shows the same grouping as in the histogram of the CaO content: a concentrated peak for mafic rocks (52.6-55.3 wt% SiO_2), a long spread for felsic rocks (68.0-85.3 wt%) and a few data points with extremely low SiO_2 content. However, note a more equally distributed data count with SiO_2 content, making it harder to differentiate lithological units based on SiO_2 content.

The geological setting in and around the COSC-1 borehole has a middle crustal origin. In a broader context, previous research has shown clear trends and estimate ranges for SiO_2 content, v_p and v_p/v_s ratio in the middle and lower crust. A global average v_p/v_s ratio for continental crust of 1.768 (Christensen and Mooney, 1995). Furthermore, a general decreasing trend of SiO_2 content is reported from 70 wt% in the upper crust to 40 wt% at 40 km depth (Christensen and Mooney, 1995; Rudnick and Fountain, 1995), implying an increase of mafic rocks with depth. A consensus is not found in the literature on the actual composition. A more recent average SiO_2 content within the lower crust estimate range is from 53 wt% to 70 wt% (Hacker et al., 2015), reporting a more felsic crustal composition as inferred before. Higher SiO_2 contents for middle crustal compositions are found in the range of 63.2 (Weaver and Tarney, 1984) to 69.4 wt% (Shaw et al., 1994).

This study already reported representable v_p values according to Christensen and Mooney (1995) in Section 4.5. Furthermore, the average SiO_2 content is 69.89±9.23 wt% and v_p/v_s ratio is 1.70±0.14 for the complete borehole, determined by averaging the entire borehole record and taking the standard deviation of 1σ. The v_p/v_s ratio is slightly smaller than the global average and an increasing in SiO_2 content shown within the range of 40 to 90 wt%, supported by the lithological units in the borehole, gradually changing towards quartz-rich rocks and indicating a more felsic composition. Seismic studies from the Irish Caledonides (Hauser et al., 2008; Licciardi et al., 2014) are interesting for comparison with these findings. A higher and more similar SiO_2 content is reported for the Irish Caledonides, ~75 wt% for the upper crust and ~64 wt% for a more silica-depleted lower crust. Average v_p/v_s ratios are found, 1.73-1.75 (Hauser et al., 2008) and 1.73±0.05 (Licciardi et al., 2014), also smaller than the global mean average.

The 2.5 km COSC-1 borehole enables to show an accurate and dense record of mixed meta-sedimentary (gneissic) and meta-igneous (amphibolitic) composition in relation with the v_p/v_s ratio. The detailed trend of decreasing v_p/v_s ratio is only recorded for a very thin section of meta-sedimentary crust (inferred to occur at mid-crustal depths in the orogen), which is not directly comparable to v_p/v_s ratio of globally inferred data where records make up ~30-40 km of crustal thickness on average (Christensen and Mooney, 1995). Also, having a continental collision does not imply the same properties after sufficient exposure at the surface compared to the present middle crust. Therefore one can discuss the implications of the COSC-1 data set within the context of crustal composition. Furthermore, the structures

in the COSC-1 borehole are finely layered with meta-sedimentary and meta-igneous rocks varying in thickness. This provides an important consequence in terms of deriving crustal composition from the v_p/v_s ratio. Other seismic methods have a long seismic wavelet and decreasing amplitude progressing to deeper structures, implying an averaging over the parameters of a large rock volume. The FWS contains a continuous resolution with depth and gives the opportunity to observe compositions of deeper buried rocks. This data set shows, therefore, a short but highly resolved composition and v_p/v_s ratio record that may be used to yield insight into the middle and lower crust in layering and continental settings.

6.2 Crustal seismic reflectivity

Crustal seismic reflections are caused by compositional layering, shear zones, anisotropy and fluid-filled faults and fractures and all of these factors may contribute to one reflection group (Smithson et al., 2000). Numerous researches have been conducted on the topic of crustal reflectivity, e.g. Birch (1960, 1961); Christensen (1965); Kern (1978); Christensen (1979); Christensen and Mooney (1995). More locally, Juhojuntti et al. (2001), Hedin (2015), Krauß et al. (2015) Simon et al. (2015) and Wenning et al. (2016) have contributed to the knowledge of important crustal reflectors in the central Swedish Caledonides. New results with varying resolution can improve our understanding of the reflectivity in and around the COSC-1 borehole.

6.2.1 Core measurements

Simulating borehole conditions in the laboratory makes it possible to assess the core velocity measurements in comparison to in-situ logging data and keeping in mind that extracting the core from the borehole releases the overburden stress and may cause core expansion and micro-cracking. When core and log measurements are compared, it has to be taken into account that these measurements were performed on different scales: for core, on a small, discrete sample, and for well-logs, on the borehole wall.

Core measurements give an accurate but much sparser data set to infer reflective successions in the COSC-1 borehole by identifying the body wave velocities and anisotropy of selected core samples. The core samples were selected, based on a geologic facies approach, to test the primary lithologies encountered in the COSC-1 borehole: amphibolite (C193-2 and C556-2), calc-silicate gneiss (C243-2), felsic gneiss (C487-1), amphibole-rich gneiss (C631-1) and garnet-bearing mica schists (C691-1) that are part of a shear zone of varying deformation degree (Wenning et al., 2016). The values found for density, v_p and v_s by performing measurements under controlled laboratory conditions are presented in Table 6.2 and Figure 6.4, along with the values of the FWS and core density data. Core measurements are taken in three directions (x_1, x_2 and x_3) and for comparison purposes, the x_3 direction is used, perpendicular to the foliation and generally parallel to the wellbore and closest resemble the logging acquisition. Core measurements enable to characterise all waveforms, therefore the shear wave velocity is given in a maximum and minimum value to assess the different polarisations of the shear wave. However, the results of the minimum and maximum v_s is very similar.

The comparison of log density and core density results show that these two data sets are generally consistent with one another. The core data are more precisely measured than the log data but are sparsely sampled and lack the more dense sampling provided by the logging measurements. Samples C243-2, C487-1 and C691-1 show a high correlation with the well-log data of the v_p and v_s of less than 150 m/s difference (except at C691-1 where no v_s and v_p/v_s ratio is measured), where core data has higher velocities. For samples C193-2, C556-2 and C631-1 a difference of more than 300 m/s is observed but is considered a reasonable difference. Independently acquired FWS data also differed up to 500 m/s

Table 6.2: The elastic velocities obtained from laboratory measurements of Wenning et al. (2016). Only the data is summarised with similarities to the full-waveform sonic data, so the data in the x_3 direction is considered.

	C193-2	**C243-2**	**C487-1**	**C556-2**	**C631-1**	**C691-1**
Depth [m]	650.8	792.5	1493.6	1691.9	2100.4	2460.3
			FWS data			
ρ [g/cm^3]	3.04	2.90	2.75	2.81	2.71	2.69
v_p [m/s]	6295	6162	6109	6067	6100	5660
v_s [m/s]	3677	3494	3459	3666	3990	-
v_p/v_s [-]	1.71	1.76	1.76	1.65	1.65	-
			Core measurement data			
ρ [g/cm^3]	3.08	2.75	2.80	3.10	3.03	2.90
v_p [m/s]	6670	6250	6110	6460	6530	5510
Min v_s [m/s]	4050	3680	3530	3990	3460	3180
Max v_s [m/s]	4130	3690	3550	4010	3510	3200
Min v_p/v_s [-]	1.62	1.69	1.72	1.61	1.86	1.72
Max v_p/v_s [-]	1.64	1.70	1.73	1.62	1.89	1.74

even by using the same measurement technique. For the v_p/v_s ratio are samples C193-2 and C243-2 slightly lower and C631-1 and C691-1 higher. On the other hand, large differences are observed between the core density and density of laboratory measurements, especially for samples C556-2, C631-1 and C691-1, ending up with differences larger than 0.15 g/cm^3. The difference between densities also has its implications for the impedance and therefore on the reflectivity.

Core measurements were taken to assess the anisotropy of the lithological units, which cannot be determined by the logging acquisition. Anisotropy of the v_p is determined to be varying from 2.97% to 18.87% and for v_s from 2.26% to 24.92% (Wenning et al., 2016). High anisotropy is found for garnet-bearing mica schist (C691-1) and low values for calc-silicate gneiss (C243-2). These results indicate the importance of the direction of measurement and incorporating anisotropy in the assessment of the crustal reflectivity. Differences between core measurements and well-log data can be explained by the anisotropy of the rocks in the borehole. Well-log data cannot account for the anisotropy and foliation, while it measures parallel to the wellbore and obtains only the v_p and non-polarised v_s. Nevertheless, as with the comparison of core and well-log data are comparable, which adds confidence in the reliability of both data sets.

6.2.2 Zero-Offset Vertical Seismic Profiling

Sonic logging and VSP are used as in-situ surveys to obtain the body wave velocities as a function of depth. This could help in lithology delineation and understanding of wave propagation in complex media. The two seismic surveys are often compared to support each other and understand discrepancies (Stewart et al., 1984; Li and Richwalski, 1996; Lüschen et al., 1996). The three main reasons inferred for differences between VSP and FWS data are differences in investigated rock volumes because of their geometry and source frequencies, instrumental errors as well as analysis inaccuracy associated with each method and different wave propagation characteristics (Thomas, 1978). Other factors, e.g. anisotropy within the borehole, could also contribute to differences.

The FWS data is already extensively described and the zero-offset vertical seismic profiling (ZVSP) will be introduced. After drilling, extensive seismic surveys took place around the COSC-1 borehole. The seismic surveys consisted of a high-resolution ZVSP, a multi-azimuthal walk-away VSP experiment and a limited 3D seismic survey with receivers at the surface and in the borehole. The ZVSP results of Krauß et al. (2015) provide P- and S-wave velocities and are compared to the picked P- and S-wave of

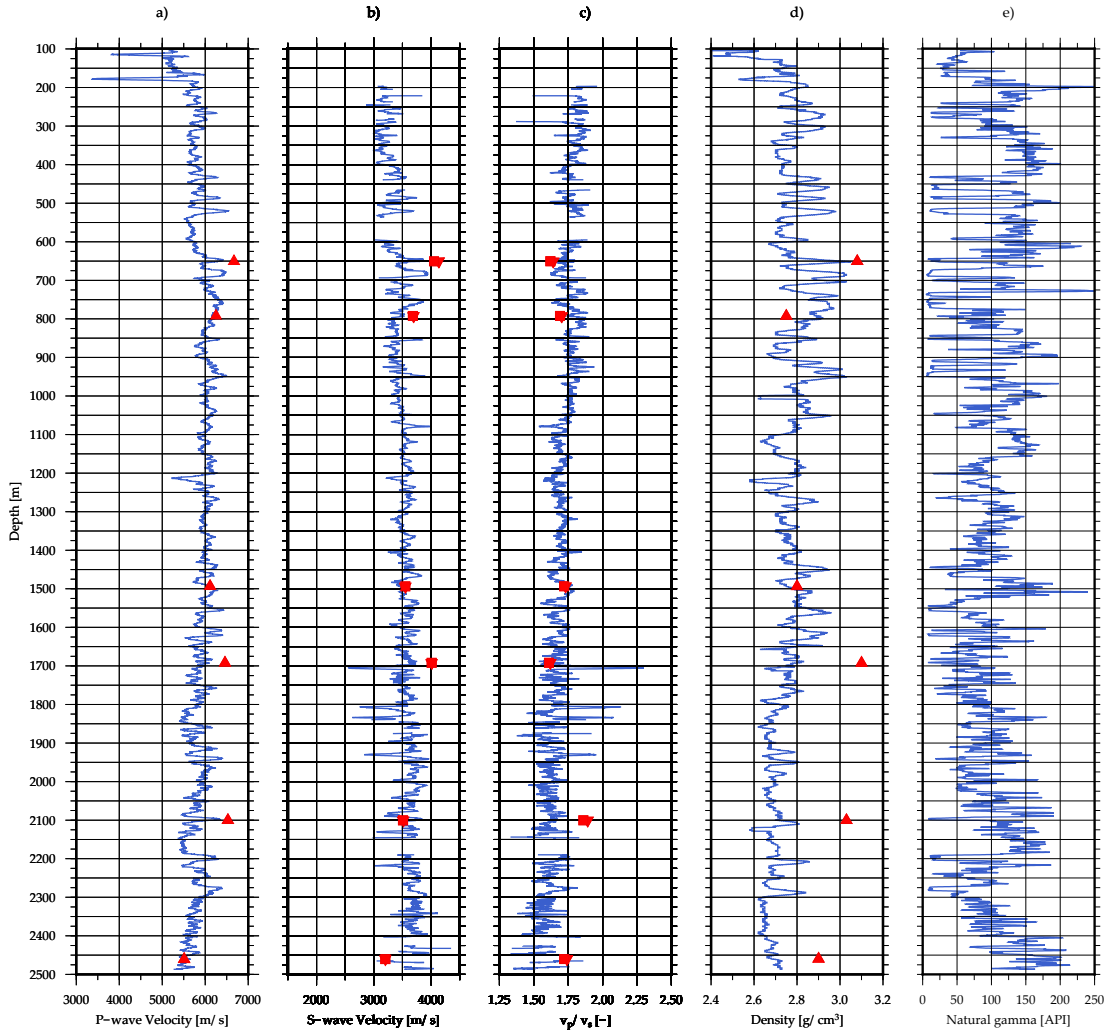

Figure 6.4: Comparison of the well-log measurements and core measurements in the COSC-1 borehole: a) the P-wave velocity, b) S-wave velocity, c) v_p/v_s ratio, d) density and e) natural gamma log. The triangles in the P-wave velocity and density log indicate the discrete core measurements. In the S-wave velocity and v_p/v_s logs minimum S-wave velocities of the discrete core measurements are denoted by squares and maximum values by inverted triangles.

the FWS data, as well as the seismic section.

Data for the ZVSP was acquired by using a hydraulic hammer source (VIBSIST 3000), located approximately 29 m away from the borehole at the surface. The source is activated over a period of 20 seconds as a sequence of impacts with increasing hit frequency. For each source point, 25 seconds of data were recorded. The wave field was recorded in the borehole by 15 three-component receivers using a Sercel Slimwave geophone chain with an inter-tool spacing of 10 meters. The ZVSP was designed to result in a geophone spacing of 2 meters over the whole borehole length. The wave field was not recorded in the upper 100 m for the following two reasons:

1. The borehole is cased down to 103 m, making it impossible record a reliable wavefield.
2. The zero-offset assumption for the geometry is not valid for the upper part of the borehole when the offset between source and borehole is too large, inferred for approximately the first 100 m (relative error is 5% at 86 m and 3% at 114 m).

Rotation of the 3C receivers components was performed to concentrate the S-wave energy on one component and thus, increase the SNR of S-wave events. Processing of the ZVSP data included signal deconvolution to sharpen the signal shape and separation of the up-going and down-going wave fields by FK-filtering.

Logging results

In Figure 6.5 is the comparison shown between the v_p, v_s and v_p/v_s ratio with the ZVSP for `FWVS1` and `FWVS2`. Prior to display, all data sets are averaged by a 25 data point moving average. The ZVSP and `FWVS2` are containing information over the complete borehole, where `FWVS1` only has information for the uppermost 1600 m. In Figure 4.6 was a drift shown between `FWVS1` and `FWVS2` in the interval of 350 m to 1250 m for the v_p. When comparing the ZVSP to the FWS data in Figure 6.5a, a high correlation of the v_p between `FWVS2` and ZVSP is observed. The resolution of the FWS data is higher and fluctuates therefore more over smaller depth intervals than the ZVSP. Nevertheless, over the complete length of the borehole, the general trend of the FWS data is highly similar to the ZVSP.

The v_s of ZVSP in Figure 6.5 shows less similar trend when compared to `FWVS1` and `FWVS2`. The drift between `FWVS1` and `FWVS2` is very small and correlation high, so a comparison is made combined. The ZVSP is in the same velocity range as the FWS data, but the data is often not correlating well, in some cases anti-correlating (e.g. 950-1040 m and 1700-1850 m). The drift of ZVSP and FWS data suggests a difference in either dispersion (Stewart et al., 1984; Li and Richwalski, 1996) or highly anisotropic behaviour of the lithological units. Anisotropic behaviour in combination with foliation is very likely in the interval of 1700 to 1880 m, where mica schist and amphibole-rich gneiss are dominantly present. The ZVSP is assumed to have a zero-offset, but a certain difference in angle between the borehole and wave propagation remains, although very small, giving rise to a varying velocity for P- and S-wave. Mica schist is estimated to have an anisotropy of 24.9% for v_s, the highest of all lithological units (Wenning et al., 2016). The v_s anisotropy for amphibole-rich gneiss is 21.1%, similar to mica schist. Also on the v_p is a certain degree of anisotropy but this is considerably smaller, especially for amphibole-rich gneiss; mica schist has a v_p anisotropy of 18.9% and amphibole-rich gneiss 8.73%. The mentioned differences by Thomas (1978) can be possible explanations, however, one would expect a similar effect in the v_p because the differences are defined by their acquisition. Another striking feature in the v_s log for both methods is that the unavailable data of `FWVS2` is accompanied by low S-wave velocities. Low SNR is encountered in the `FWVS2` at low v_s, making it impossible to observe the S-wave arrival in the seismic sections. Last notable difference is the drift in the uppermost 400 m, the v_s of the ZVSP contains also low velocities, just like `FWVS1`. As inferred in Section 4.5, the low v_s could be due to the borehole condition after drilling. Both data sets, the `FWVS1` and ZVSP, are acquired directly after drilling, causing low velocities as a result of micro fractures which reinstalls over time. Making it possible that the same effect is not observed by the `FWVS2`. The v_p/v_s ratio of the ZVSP in Figure 6.5c is in the same range of the FWS data sets. Deviations between the two types of measurement in v_s didn't result in large differences of v_p/v_s ratio.

The performance of the two different seismic methods is similar, gaining confidence in the velocities, especially of the `FWVS2`. The observed drift of `FWVS1` in v_p makes the correlation decrease and result in a less fit. Overall are the velocities and the v_p/v_s ratio in the same range, making sure that the data sets support each other, despite the difference in resolution. In addition to the limitation of information with depth, the data set of `FWVS2` is nevertheless preferred.

Seismic results

Besides the well-log information, also the seismic data of the ZVSP can be used to compare and validate the results of the FWS logging. The results of seismic modelling are compared with the up-going wave field of the ZVSP, representing the reflection response. The up-going wave field is converted to TWT by delaying the traces with the first-break arrival time. The seismic section can be further processed by extracting the outer margin, resulting into a corridor stack. The corridor stack only provides reflection information at the edge of the up-going wave field and is therefore limiting the seismic information. With

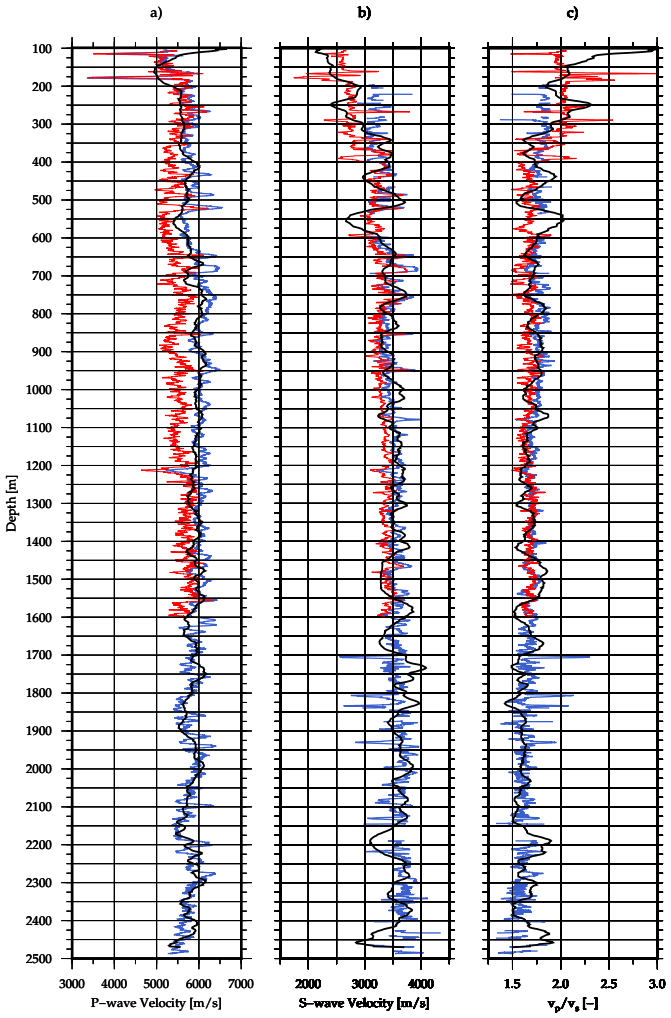

Figure 6.5: Comparison of the ZVSP measurements and core measurements in the COSC-1 borehole: a) the P-wave velocity, b) S-wave velocity, c) v_p/v_s ratio. The v_p, v_s and v_p/v_s logs from the `FWVS1` data are shown in red, the `FWVS2` data in blue and the ZVSP data in black. Prior to display, all data sets are averaged by applying a 25 data point moving average.

the up-going field can the structure around the borehole be analysed by focussing on clear continuous reflections, where the corridor stack only consists of one trace out of the complete ZVSP acquisition.

The corridor stack and up-going field of the ZVSP are shown in Figure 6.6, together with the 1D synthetic seismogram after convolution with a 65 Hz minimum phase wavelet and the 2D finite-difference model. The correlation between the 1D (65 Hz wavelet) and 2D model decreased compared to the 1D model (50 Hz wavelet) in Figure 5.9, the delay between the reflections increased to 0.015 s, the sequence of reflections is still similar despite the difference in wavelet. Therefore is focussed on the 1D model, which should approximate the frequency content of the ZVSP better. Due to the triangular shape, it hard to assess the correlation between the up-going wave field and the two seismic models in the upper 0.05 to 0.10 s. Respectively, two and three high amplitude reflections are present in the 1D and 2D seismic models where the few traces of the up-going wave field show a similar result. Progressing downwards, reflections at 0.20, 0.24, 0.26, 0.42, 0.43, 0.51, 0.525, 0.55, 0.56, 0.62, 0.65, 0.77, 0.78 and 0.79 s are correlating roughly with the up-going wave field. Unlike the seismic models, reflections are not decreasing in amplitude between 0.50 to 0.75 s, contradicting a low reflective zone in the lower part of the borehole. But the three dipping high amplitude reflections at 0.77, 0.78 and 0.79 s in the up-going wave field appear to have the same TWT and relative amplitude compared to reflections in the seismic models, which are characteristic in the seismic data.

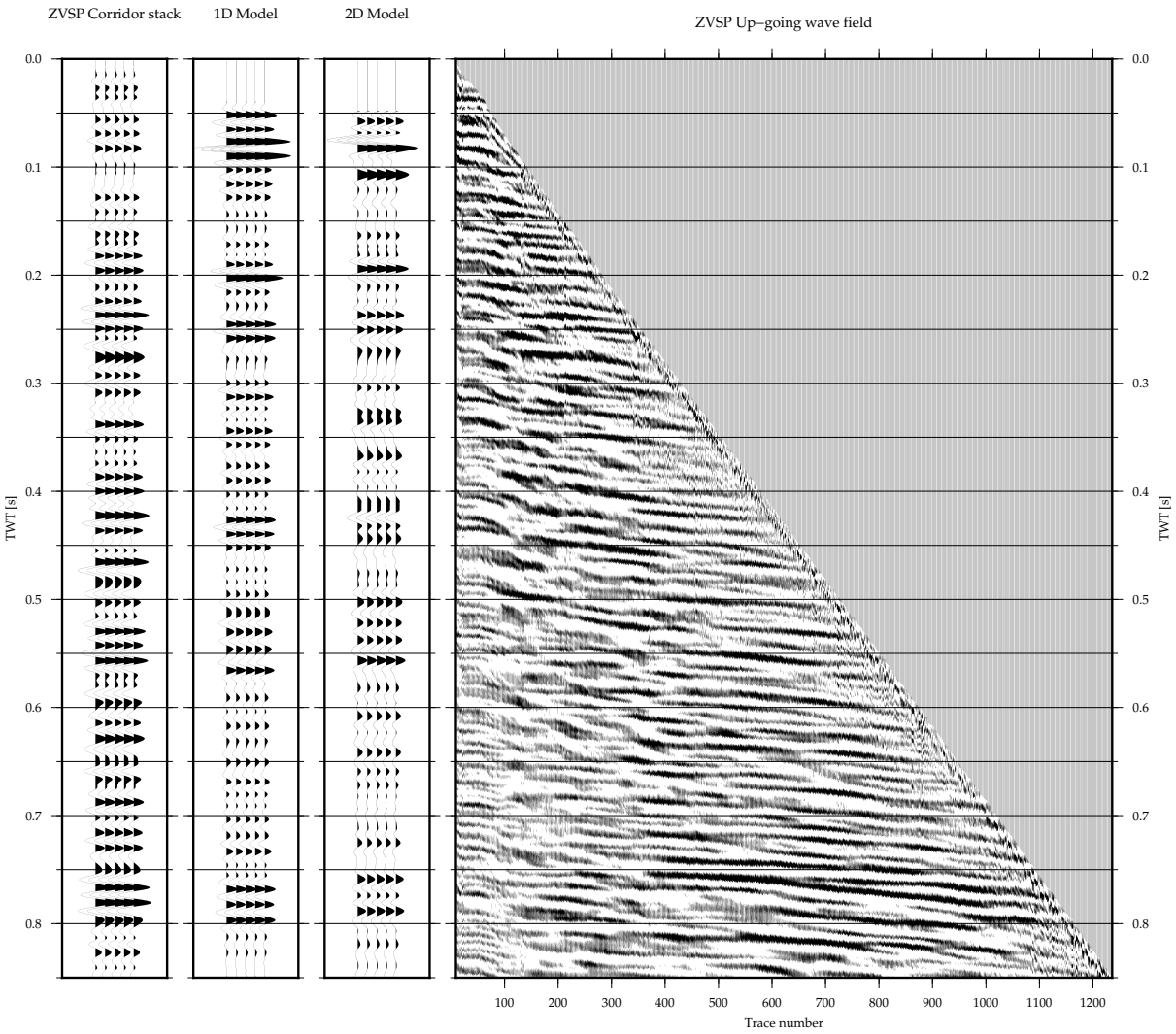

Figure 6.6: Comparison of the 1D and 2D finite-difference seismic models to the corridor stack and up-going wave field resulting from the ZVSP.

The correlation between the seismic models and the corridor stack is less strong compared to the up-going wave field. In the uppermost 0.42 s reflections are anti-correlating and the amplitude of the reflections are differently distributed. At 0.42 s is a reflection found which correlates well with the 2D seismic model and the up-going wave field. Progressing downwards, reflections at 0.525, 0.59, 0.77, 0.78 and 0.79 s are correlating with the 1D model. In general, the corridor stack lacks any correlation in the top part of the borehole, which can be explained by looking at the outer margin of the up-going wave field; not all reflections are present or are slightly delayed, especially in the uppermost 0.42 s. Giving rise to a false sense of reflectivity in the corridor stack. The correlation increases in the lower part, but the low reflective zone between 0.55 and 0.76 s, as seen in the seismic models is not as such shown by the corridor stack, where every reflection seems to have relative amplitude.

Velocities in the same range are found between the FWS data and ZVSP, eliminating uncertainty in the velocities between high-resolution FWS logging and low-resolution seismic studies. The correlation of the 1D model is better with the up-going wave field than with the corridor stack, the correlation with 2D model is less well due to the difference in source wavelet. Furthermore, a high correlation is obtained at reflections which are characteristic, especially in the lower part, and important for the assessment of reflectivity in the COSC-1 borehole. The corridor stack does not provide a similar result, leading to a preference of the up-going wave field over the corridor stack in the interpretation of the reflectivity.

6.2.3 Surface seismic

A limited 3D seismic survey was performed after drilling of the COSC-1 borehole covering a surface area of about 1.5 km^2 around the drill site (Hedin et al., 2016). This study provides information on the 3D geometry of structures within the drilled Lower SNC and underlying rocks down to at least 9 km. Within the 3D migrated seismic cube, Inline 1044 and Crossline 1076 are closest to the COSC-1 borehole, therefore are the seismic models compared to this position in the 3D seismic cube. Besides the comparison of the final migrated seismic section of the limited 3D seismic survey, an example of a shot gather is shown to compare the COSC-1 seismic model with.

The frequency content of the surface seismic has been determined by analysing the receiver gather close to the borehole (PEG226). Figure 6.7a shows the frequency content of the surface seismic in blue, where the power of dominant frequency is concentrated around 50 Hz. A minimum phase wavelet of 50 Hz is therefore used (Figure 6.7b) to match with the frequency content and to prevent small shifts in time due to differences in frequency content. The red line in Figure 6.7a represents the source wavelet of the 1D seismic model, accurately correlating with the source signature of the 3D seismic survey. Besides the 1D seismic model, also the 2D finite-difference model is used to compare with the surface seismic. For the 2D model a 50 Hz Ricker wavelet is used, indicating a mismatch in source wavelet, where seismic surveys are in general better approximated by minimum phase wavelets, as shown in Figure 6.7a.

3D migrated seismic section

The comparison of the seismic models and 3D migrated seismic section is shown in Figure 6.8, where the seismic models are displayed in red at Inline 1044 and replacing Crosslines 1076-1080. The zero-offset trace originating from the seismic model are five times duplicated to enhance the visual comparison. A bulk shift of 93.65 ms downwards is applied to the zero-offset traces to account for the depth of the surface. The black traces in Figure 6.8 are originated from the 3D migrated seismic section. In Figure 6.8a is the comparison with the 1D model shown. In respect to Crossline 1075, the 1D model correlates poorly with the 3D migrated seismic section. The first high amplitude reflection 0.15 s, followed by an anti-correlation with the second high amplitude reflection at 0.17 s. Mixed correlations are found progressing downwards, reflections at 0.275, 0.45, 0.52, 0.61 and 0.64 s are matching with the seismic section. Three high amplitude and dipping reflections around 0.8 s are found in the seismic section, however, these similar reflections are in both seismic models shifted by 30 ms. The mismatch between the characteristic events in the seismic models and the 3D migrated seismic section raises uncertainty about the correlation with the other reflections. Similar results are found in the comparison between the 3D migrated seismic section and the 2D model. Various reflections are correlating, others are anti-correlating and the characteristic dipping reflections at 0.8 s are appearing earlier compared to the 2D seismic model in Figure 6.8b. Despite the uncertainty, the 2D model indicates a better correlation between low amplitude reflections in the middle part of the borehole (e.g. reflections at 0.32, 0.52, 0.58 and 0.62 s). Besides the presented results in this section, also a comparison was performed on a 1D model after convolution with a 50 Hz Ricker wavelet which did not result in an improved correlation. The shape of the seismic wavelet used for 1D convolution is considered as critical in 1D modelling and therefore is a Ricker wavelet a poorer approximation. Also, the effect of polarity reversal is assessed but did not give rise to an improved correlation.

Correlation of synthetic seismograms and stacked time-migrated seismic data is always subjected to uncertainty, Yilmaz (2001) inferred mismatches by i.e. phase rotation with the depth of the synthetic seismogram, inaccuracies in the check-shot survey information and presence of frequency components outside the dominant seismic signal bandwidth. The explanation of the consistent poor correlation between the 3D migrated seismic section and the seismic models cannot be found in the v_p and v_s. In

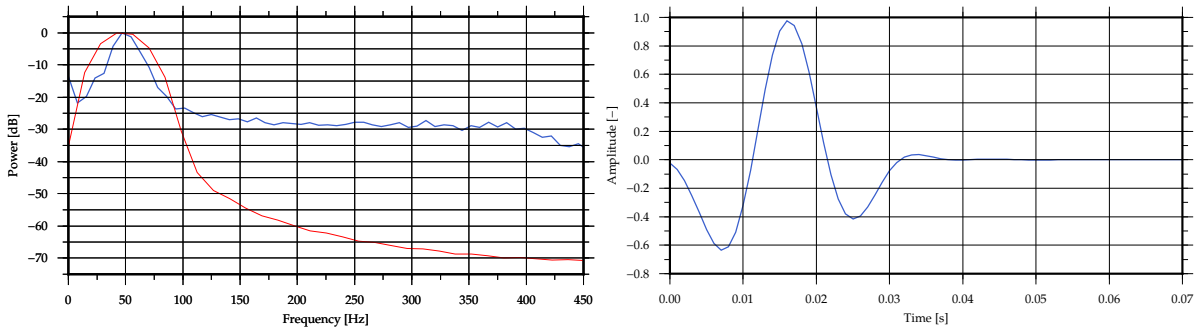

(a) (b)

Figure 6.7: Comparison of the 50 Hz minimum phase wavelet with the surface seismic frequency content. a) the signature of the wavelet over time and b) the frequency spectrum of the surface seismic in blue and the frequency spectrum of the wavelet in red, matching with the dominant frequency of the surface seismic.

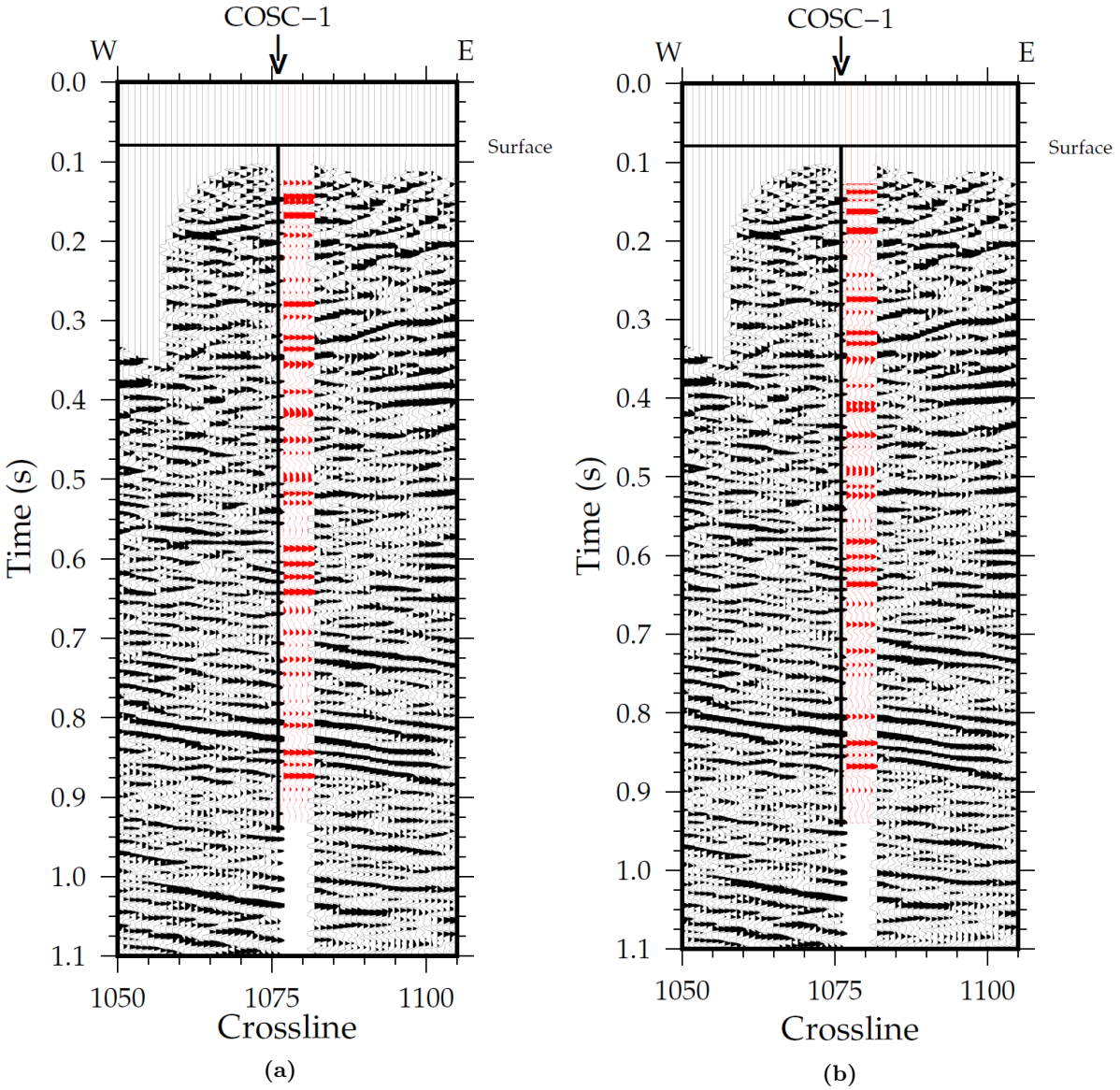

(a) (b)

Figure 6.8: Comparison of the 1D and 2D finite-difference seismic models with the surface seismic of the 3D migrated section. a) 1D seismic model after convolution with a 50 Hz minimum phase wavelet displayed in red. b) 2D finite-difference model with a 50 Hz Ricker wavelet source displayed in red. The black traces originate from the 3D migrated section.

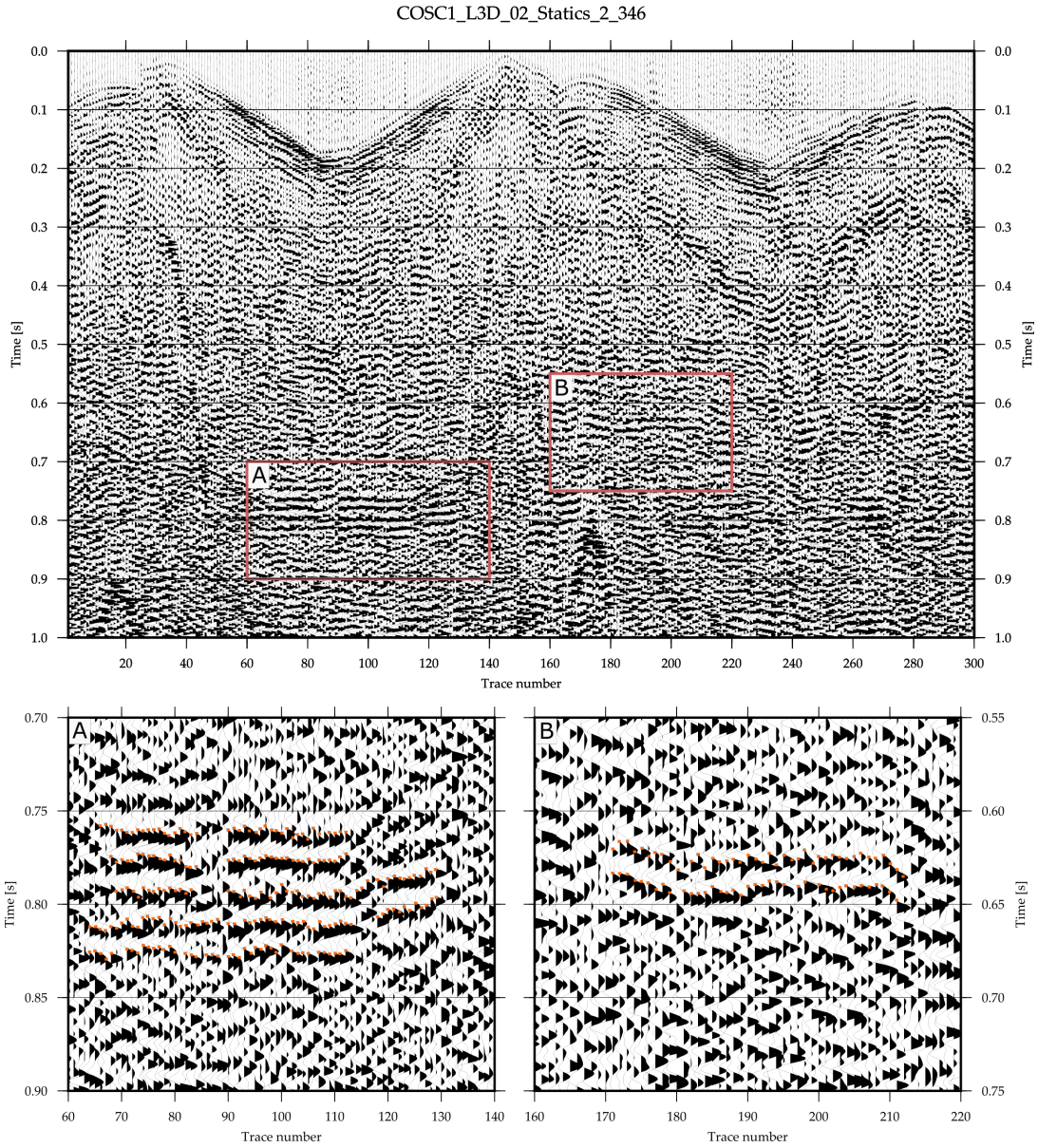

Figure 6.9: Analysis of the `COSC1_L3D_346` shot gather. The upper panel represents the processed shot gather, the lower panels represent small sections of clear reflectivity (orange lines).

general, differences exist between velocities obtained from logging or seismic surveys, the comparison with the ZVSP revealed a good correlation with the velocities and the seismic section. The up-going wave field also revealed three dipping reflections with a high amplitude which correlates with both seismic models, eliminating differences in velocity between the FWS data and the surface seismic. The frequency content of the sources is correlating well, as pointed out in Figure 6.7a. The anisotropic behaviour within the borehole is previously mentioned as the cause of mismatch between seismic results, where the lower part of the borehole is identified by successions of amphibole-rich gneiss and mica schist and can cause differences in the occurrence of reflections at certain TWT. However, anisotropy is not solely contributing to the existing delay of 0.02 to 0.05 s. Another probable explanation can be found in the uncertainty of the migration velocity. By applying an inaccurate migration velocity reflections are not fully focussed and correctly positioned in time. By revisiting the migration velocity and constraints to the derived FWS results, the 3D migrated seismic section can shift in time and enhance the fit with the seismic models of the FWS data and ZVSP.

Shot gather

The acquisition of the limited 3D seismic survey was performed by using a stationary spread of 429 receivers (20 m separation along seven lines spaced 200 m apart) together with the ZVSP and multi-azimuthal walkaway VSP. The `COSC1_L3D_346` shot gather is selected among the other shot gathers to serve as an example to show the reflectivity close to the COSC-1 borehole. This shot gather was excited by a rock breaking hammer (VIBSIST, Cosma and Enescu, 2001) located ~500 m east of the COSC-1 drill site. In Figure 6.9 is the `COSC1_L3D_346` shot gather shown after processing. Applied processing steps are: processing flow of Hedin et al. (2016) after refraction static correction (`COSC1_L3D_02_Statics_2_346`), frequency filtering (45-60-120-180 Hz), Automatic Gain Control (200 ms) and spherical divergence correction ($\sqrt{t}$). The upper panel of Figure 6.9 shows the seismic data of traces 1-300 down to 1.0 s. Some weak reflectivity is observed throughout the seismic section and strong reflectivity at two locations: five reflections at 0.76, 0.775, 0.795, 0.81 and 0.825 s (orange traces (64-129) in the lower left panel of Figure 6.9) and two reflections at 0.63 and 0.64 s (orange trace (172-212) in the lower right panel of Figure 6.9). These reflections are compared to the seismic models in Figure 5.9. Before a comparison can be performed, several observations are noted. First of all, source excitation occurred at 19 ms as a result of refraction static correction, reflections will therefore resemble the modelling results after subtraction of the source excitation time. Furthermore, the processing on the seismic models and shot gather is not identical and can lead to differences. Finally, the shot gather is not located in the borehole, the same geological units will be encountered however dependant of offset. The reflections found in the shot gather resemble roughly with the 1D and 2D seismic models. The two reflections at 0.63 and 0.64 s coincide with the low amplitude reflection at 0.64 s in the models, a better fit is obtained with the 2D model. Where two reflections are encountered in the shot gather, the seismic models only show one significant reflection, uncertainty arises if the reflection at 0.61 s correlates with the second reflection. The five strong reflections between 0.76 and 0.825 s coincide with the three high amplitude reflections in both seismic models between 0.76 and 0.795 s. The two reflections in the shot gather after 0.8 s are not found in the seismic models.

The found reflections in the shot gather are only approximated to correlate with the seismic models, uncertainty exists if the reflections are similar. Based on the strong amplitude and continuity already after refraction static correction and minor processing, the reflections between 0.76 and 0.795 s correlate better than the 3D migrated seismic section. It has to be verified if the reflections are similar.

6.2.4 Reflectivity of the COSC-1 borehole

Seismic modelling of the FWS data provided densely sampled velocity information through the Lower SNC into the basal shear zone, validated by core measurements and ZVSP results. Hedin et al. (2016) divides the reflectivity in the COSC-1 borehole into two sections based on seismic observations and lithologies observed in the borehole: 1) the Lower SNC (<1710 m) and 2) the high-strain shear zone (>1710 m). Strong reflections due to the abundance of interfaces are observed in the uppermost part of the borehole, dominated by gneisses with mafic lenses of variable thickness within felsic rocks. Seismic modelling of the FWS data revealed strong reflections in the upper part correlating well with the ZVSP and sporadically with the 3D migrated seismic section.

Gradual increasing strain below 1700 m, with mica schists and intermittent mylonites increasing in frequency and thickness, has previously been interpreted as the basal shear zone of the Lower SNC (Hedin et al., 2016). More recently, strong reflectivity between mica schist and amphibole-rich gneiss to explain seismic reflections in the middle crust, large impedance contrast and level of anisotropy give rise to these reflections (Wenning et al., 2016). In laboratory conditions, the occurrence of the mylonitic shear zone within layered amphibolites and mica schist could be highly reflective in other

middle crustal levels, producing R_c, when juxtaposed, of 0.1. Combined observation of the FWS data and geological interpretation on the core reports a lower R_c, the impedance contrast between mica schists and amphibole-rich gneiss result in a maximum R_c of 0.05. Differences in magnitude are explained due ideal conditions in the laboratory and finely layering observed in the FWS data, resulting in gradually changing R_c.

The interpreted basal shear zone has a nearly uniform thickness throughout the seismic volume and ca. 12° dip towards the south-east (Hedin et al., 2016), is supported by the up-going wave field of the ZVSP. Nevertheless, high reflectivity in the basal shear zone is inferred to be deeper than was shown before. Seismic modelling results of the FWS data places the reflective interfaces at 0.84-0.90 s TWT, 30 ms deeper in comparison to the surface seismic. Uncertainty in seismic wavelength and velocities in the borehole itself is eliminated, however, uncertainty remains in the uppermost 103 m which approximated by constant velocity and density.

CHAPTER 7

Conclusion and outlook

The 2.5 km deep scientific COSC-1 borehole (ICDP 5054-1-A) was successfully drilled during spring and summer of 2014, targeting the Lower Seve Nappe Complex (SNC) with a variety of conducted seismic studies, nearly 100% core recovery, downhole and on-core measurements. The full-waveform sonic (FWS) data set has been processed and analysed for two logging campaigns (`FWVS1` and `FWVS2`) to provide compressional- and shear wave velocity information within the COSC-1 borehole. In addition to velocity information also core density data are used to compare to core measurements, XRF data and ZVSP velocities. Furthermore is the velocity and density information used as input parameters in 1D seismic modelling and 2D elastic and isotropic finite-difference modelling to compare the synthetic traces to other seismic studies; i.e. ZVSP and surface seismic.

7.1 Conclusion

Two FWS data sets have been processed and analysed resulting in the v_p and v_s. `FWVS1` contains velocity information down to 1600 m depth and after processing the P- and S-wave arrival is determined for every trace. `FWVS2` is logged down to 2488 m but the data is of lower quality resulting in a picked P-wave for every trace and 84.82% of the traces for S-wave arrival after processing. The resulting v_p and v_s of `FWVS1` and `FWVS2` are correlating when picked, although a ∼500 m/s drift is observed in the v_p between 400 and 1200 m. General trends of the v_p, v_s and v_p/v_s ratio indicate the following: (1) the fluctuating v_p is considered to be varying and reinstalling itself around a constant velocity with depth, (2) the v_s is gradually increasing with depth as a combined result of mineral composition and overburden pressure and (3) the v_p and increasing v_s result in a gradually decreasing in v_p/v_s ratio. The gradual change in lithology is supported by the interpretation of the core and XRF data. The densely sampled XRF data shows similar trends with depth; relatively moderately good correlation coefficients, especially after visual inspection, are obtained between the v_p/v_s ratio with an observed increasing SiO_2 content (R = -0.3182) and decreasing CaO content (R = 0.3396). The results imply a gradual transitioning middle crust from mafic to felsic composition over the complete borehole. An average SiO_2 content of 69.89±9.23 wt% and v_p/v_s ratio of 1.70±0.14 is inferred from the data sets.

The velocities have been validated by comparing the logging data with direct core measurements and velocities inferred by the ZVSP. Despite the difference in resolution between the core measurement and ZVSP, bridged by the FWS data set, velocities are correlating. Sparsely sampled core measurements differ in 3 out of 6 samples with 300 m/s and a maximum of 430 m/s for amphibole-rich gneiss, caused by high anisotropy. Velocities originated from the ZVSP are in the same velocity range as the FWS results with an excellent correlation for the v_p. Similar v_p and v_s between different seismic surveys gives a good starting point when analysing synthetic seismic models based on the FWS data with actual surface seismic surveys.

The FWS results have been used to generate 1D synthetic seismograms of `FWVS1` and `FWVS2`, and a 2D elastic and isotropic finite-difference model for `FWVS2`. Both models are comparable, indicating a reflective Lower SNC. Differences in the seismic models are due to the choice of the seismic wavelet. Both models have been compared to the up-going wave field and corridor stack of the ZVSP; high correlation is obtained with the up-going wave field in general and a lack correlation with the upper part of the corridor stack. The lower part of the corridor stack and up-going wave field (0.74-0.80 s TWT) indicate three highly reflective interfaces which are also observed in the seismic models. A combination of the seismic models and ZVSP gives a good interpretation of the local reflectivity in the COSC-1 borehole. Poor correlation is obtained with the 3D migrated seismic section, slightly better for the 2D model. The three highly reflective previously observed interfaces appear to be delayed by 30 ms. Probable reasons for the poor correlation, especially in the lower part of the borehole, are the result of the anisotropic behaviour of the highly deformed basal shear zone and uncertainties in the migration velocity of the 3D seismic cube.

Reflective interfaces in the basal shear zone (>1710 m) are inferred as a result of amphibole-rich gneiss and mica schist interfaces. Similar reflections in the 3D migrated section indicate similar results but yields a poor correlation with the seismic models. Comparisons of the FWS data set show correlations with other seismic methods which can be used in the further development of COSC, but also differences which may have to be accounted for in the future.

7.2 Outlook

The data set of the COSC scientific drilling project is large and growing, further analysis can be performed to improve the results of this thesis study or new information can validate and extend the obtained results. Follow-up studies can be performed on either the geophysics or the rock properties in and around the COSC-1 borehole.

The missing v_s information can be retrieved from the data by using different and more sophisticated processing algorithms, e.g. Slowness Time Coherence or Maximum Likelihood Method. The additional v_s can be used to further analyse the uppermost and lowermost 100 m.

Seismic modelling of the FWS resulted in a good correlation with the ZVSP, proving to be a powerful method to estimate the seismic reflection response in and around the COSC-1 borehole as a function of offset. Improved seismic modelling and a correct implementation of the free surface could enhance the reflection response and analyse the converted waves in a more qualitative manner. Furthermore, the seismic modelling can be extended into elastic and anisotropic (VTI or orthorhombic symmetry) finite-difference modelling by using the results of the core measurements, lowering the uncertainty existing between the other performed seismic studies.

To increase the correlation between the FWS modelling results and the 3D migrated seismic section, besides the addition of anisotropy in the seismic modelling, the migration velocity can be revisited and constrained to the FWS logging results.

The middle crustal composition in the central Swedish Caledonides is inferred by a 2.5 km thick succession of lithological units transitioning towards felsic conditions. The composition can be further analysed when minor trace elements are included into the study of the rock properties.

Acknowledgement

During this Master thesis research, I have been supported by many people. I would like to express my gratitude to all who made my stay in Uppsala a success.
First of all, I would like to thank my supervisors Chris Juhlin and Cédric Schmelzbach for providing me with the opportunity to work at Uppsala University and to visit the COSC-1 drill site in Åre. Furthermore, I am thankful for reviewing my thesis and providing me with feedback.
I would like to express my gratitude to Bjarne Almqvist and Peter Hedin for their never-ending enthusiasm and willingness to help me out. My discussions with you have inspired me greatly and driven me during the progress of this master thesis research. It was a great pleasure working with you. Furthermore, I would like to thank all other people involved in the COSC scientific drilling project who I worked with: David Gee for helping me out and inspiring me with the Caledonian geology, Théo Berthét for the interesting discussions and letting me help assist in the fieldwork around the COSC-1 drill site and Henning Lorenz for all COSC related questions. Also I would like to thank Per-Gunnar Alm (Lund University) and Jochem Kuck (GFZ Potsdam) for acquiring the full-waveform sonic data set and Felix Krauß (GFZ Potsdam) for answering all my questions on the ZVSP acquisition and processing.
I would like to thank all my roommates, colleagues and friends I met for joining in fika and making my time in Uppsala unforgettable.
Finally, I am Kira Aßhoff thankful for standing by my side and for simply being there despite the geographical distance.
All in all, this research experience and my stay in Uppsala has enriched me.

Uppsala, 12 August 2016 M.C. Ooms

Bibliography

K. Aki and P.G. Richards. *Quantative seismology*. University Science Books, 2nd edition, 2002. ISBN 978-1891389634.

R.M. Alford, K.R. Kelly, and D.M. Boore. Accuracy of finite-difference modelling of the acoustic wave equation. *Geophysics*, 39(6):834–842, 1974. doi: 10.1190/1.1440470.

A. Bayliss, K.E. Jordan, B.J. Lemesurier, and E. Turkel. A fourth-order accurate finite-difference scheme for the computation of elastic waves. *Bulletin of the Seismological Society of America*, 76(4):1115–1132, 1986.

F. Birch. The velocity of compressional waves in rocks to 10 kilobars, Part 1. *Journal of Geophysical Research*, 65(4):1083–1102, 1960. doi: 10.1029/JZ065i004p01083.

F. Birch. The velocity of compressional waves in rocks to 10 kilobars, Part 2. *Journal of Geophysical Research*, 66(7):2199–2224, 1961. doi: 10.1029/JZ066i007p02199.

G.J. Borradaile. *Statistics of earth science: their distribution in space, time, and orientation*. Springer-Verlag, 2003. ISBN 3-540-43603-0.

N.I. Christensen. Compressional wave velocities in metamorphic rocks at pressures to 10 kbar. *Journal of Geophysical Research*, 70(24):6147–6164, 1965. doi: 10.1029/JZ070i024p06147.

N.I. Christensen. Compressional wave velocities in rocks at high temperatures and pressures, critical thermal gradients, and crustal low-velocity zones. *Journal of Geophysical Research*, 84(B12):6849–6857, 1979. doi: 10.1029/JB084iB12p06849.

N.I. Christensen and W.D. Mooney. Seismic velocity structure and composition of the continental crust: A global view. *Journal of Geophysical Research*, 100(B6):9761–9788, 1995. doi: 10.1029/95JB00259.

F. Corfu, D. Gasser, and D.M. Chew. New perspectives on the Caledonides of Scandinavia and related areas: introduction. In *New Perspectives on the Caledonides of Scandinavia and Related Areas*. Geological Society, London, Special Publications, 390, 2014a. ISBN 978-1-86239-377-6. doi: 10.1144/SP390.28.

F. Corfu, T.B. Andersan, and D. Gasser. The Scandinavian Caledonides: main features, conceptual advances and critical questions. In *New Perspectives on the Caledonides of Scandinavia and Related Areas*. Geological Society, London, Special Publications, 390, 2014b. ISBN 978-1-86239-377-6. doi: 10.1144/SP390.28.

C. Cosma and N. Enescu. Characterization of fractured rock in the vicinity of tunnels by the swept impact seismic technique. *International Journal of Rock Mechanics and Mining Sciences*, 38(6):815–821, 2001. doi: 10.1016/S1365-1609(01)00046-6.

R. Courant, K. Friedrichs, and H. Lewy. Über die partiellen Differenzengleichungen der mathematischen Physik. *Mathematische Annalen*, 100(1):32–74, 1928. doi: 10.1007/BF01448839.

D. Dyrelius. Aeromagnetic interpretation in a geotraverse area across the central Scandinavian Caledonides. *Geoliska Föreningens i Stockholm Förhandlingar*, 102(4):421–438, 1980. doi: 10.1080/11035898009454498.

D. Dyrelius. Gravity and magnetics in the central Scandes. *Geoliska Föreningens i Stockholm Förhandlingar*, 108(3):278–281, 1986. doi: 10.1080/11035898609454705.

D. Dyrelius, D.G. Gee, R. Gorbatschev, H. Ramberg, and E. Zachrisson. A profile through the central Scandinavian Caledonides. *Tectonophysics*, 69(3):247–284, 1980. doi: 10.1016/0040-1951(80)90213-9.

D.W. Ellis and J.M. Singer. *Well Logging for Earth Scientists.* Springer, 2nd edition, 2007. ISBN 978-1-4020-3738-2.

R. Emmermann and J. Lauterjung. The German Continental Deep Drilling Program KTB: overview and major results. *Journal of Geophysical Research*, 102(B8):18179–18201, 1997. doi: 10.1029/96JB03945.

A. Fichtner. *Full Seismic Waveform Modelling and Inversion.* Springer-Verlag, 2011. ISBN 978-3-642-15806-3.

S. Fomel, P. Sava, I. Vlad, Y. Liu, and V. Bashkardin. Madagascar: open-source software project for multidimensional data analysis and reproducible computational experiments. *Journal of Open Research Software*, 1(1):1:e8, 2013. doi: 10.5334/jors.ag.

D. Gasser. The Caledonides of Greenland, Svalbard and other Arctic areas: status of research and open questions. In *New Perspectives on the Caledonides of Scandinavia and Related Areas.* Geological Society, London, Special Publications, 390, 2013. ISBN 978-1-86239-377-6. doi: 10.1144/SP390.17.

D.G. Gee. A tectonic model for the central part of the Scandinavian Caledonides. *American Journal of Science*, 275A:468–515, 1975.

D.G. Gee and B.A. Sturt. *The Caledonide Orogen: Scandinavia and Related Areas.* John Wiley and Sons Ltd., 1985. ISBN 0-471-10504-X.

D.G. Gee, R. Kumpulainen, D. Roberts, M.B. Stephens, and E. Zachrisson. Scandinavian Caledonides, Tectonostratigraphic Map, Scale 1:2,000,000. *Sveriges Geologiska Undersökning, Ba 35*, 1985.

D.G. Gee, H. Fossen, N. Henriksen, and A.K. Higgins. From the early Paleozoic platforms of Baltica and Laurentia to the Caledonide Orogen of Scandinavia and Greenland. *Episodes*, 31(1):44–51, 2008.

D.G. Gee, C. Juhlin, C. Pascal, and P. Robinson. Collisional Orogeny in the Scandinavian Caledonides (COSC). *Geoliska Föreningens i Stockholm Förhandlingar*, 132(1):29–44, 2010. doi: 10.1080/11035891003759188.

B.R. Hacker, P.B. Kelemen, and M.D. Behn. Continental lower crust. *Annual Review of Earth and Planetary Sciences*, 43:167–205, 2015. doi: 10.1146/annurev-earth-050212-124117.

F. Hauser, B.M. O'Reilly, P.W. Readman, J.S. Daly, and R. Van den Berg. Constraints on crustal structure and composition within a continental suture zone in the Irish Caledonides from shear wave wide-angle reflection data and lower crustal xenoliths. *Geophysical Journal International*, 175(3): 1254–1272, 2008. doi: 10.1111/j.1365-246X.2008.03945.x.

P. Hedin. *Geophysical studies of the upper crust of the central Swedish Caledonides in relation to the COSC scientific drilling project.* Digital Comprehensive Summaries of Uppsala Dissertations from the Faculty of Science and Technology, Acta Universitatis Upsaliensis 1281, 2015. ISBN 978-91-554-9320-2.

P. Hedin, C. Juhlin, and D.G. Gee. Seismic imaging of the Scandinavian Caledonides to define ICDP drilling sites. *Tectonophysics*, 554–557:30–41, 2012. doi: 10.1016/j.tecto.2012.05.026.

P. Hedin, A. Malehmir, D.G. Gee, C. Juhlin, and D. Dyrelius. 3D interpretation by integrating seismic and potential field data in the vicinity of the proposed COSC-1 drill site, central Swedish Caledonides. *Geological Society, London, Special Publications*, 390:301–319, 2014. doi: 10.1144/SP390.15.

P. Hedin, B. Almqvist, T. Berthet, C. Juhlin, S. Buske, H. Simon, R. Giese, F. Krauß, J.-E. Rosberg, and P.-G. Alm. 3D reflection seismic imaging at the 2.5 km deep COSC-1 scientific borehole, central Scandinavian Caledonides. *Tectonophysics*, 2016. doi: 10.1016/j.tecto.2015.12.013.

K. Hsu and A.B. Baggeroer. Application of the maximum-likelihood method (MLM) for sonic velocity logging. *Geophysics*, 51(3):780–787, 1986. doi: 10.1190/1.1442130.

C.A. Hurich, H. Palm, D. Dyrelius, and Y. Kristoffersen. Deformation of the Baltic continental crust during Caledonide intracontinental subduction: views from seismic reflection data. *Geology*, 17(5): 423–425, 1989. doi: 10.1130/0091-7613(1989)017⟨0423:DOTBCC⟩2.3.CO;2.

ICDP. *Annual Report: ICDP Status and Future as of December 2015*. International Continental Scientific Drilling Program, 2015.

C. Juhlin. Finite-difference elastic wave propagation in 2d heterogeneous transversely isotropic media. *Geophysical Prospecting*, 43(6):843–858, 1995. doi: 10.1111/j.1365-2478.1995.tb00284.x.

N. Juhojuntti, C. Juhlin, and D. Dyrelius. Crustal reflectivity underneath the central Scandinavian Caledonides. *Tectonophysics*, 334(3-4):191–210, 2001. doi: 10.1016/S0040-1951(00)00292-4.

F.C. Karal and J.B. Keller. Elastic wave propagation in homogeneous and inhomogeneous media. *Journal of the Acoustical Society of America*, 31(6):694–705, 1959. doi: 10.1121/1.1907775.

K.R. Kelly, R.W. Ward, S. Treitel, and R.M. Alford. Synthetic seismograms: a finite difference approach. *Geophysics*, 41(1):2–27, 1976. doi: 10.1190/1.1440605.

H. Kern. Effect of high temperature and high confining pressure on compressional wave velocities in quartz-bearing and quartz-free igneous and metamorphic rocks. *Tectonophysics*, 44(1):185–203, 1978. doi: 10.1016/0040-1951(78)90070-7.

C.V. Kimball and T.L. Marzetta. Semblance processing of borehole acoustic array data. *Geophysics*, 49 (3):274–281, 1984. doi: 10.1190/1.1441659.

T. Korja, M. Smirnov, L.B. Pedersen, and M. Gharibi. Structure of the Central Scandinavian Caledonides and the underlying Precambrian basement, new constraints from magnetotellurics. *Geophysical Journal International*, 175(1):55–69, 2008. doi: 10.1111/j.1365-246X.2008.03913.x.

Y.A. Kozlovsky. *The Superdeep Well of the Kola Peninsula*. Springer, 1987.

F. Krauß, H. Simon, R. Giese, S. Buske, P. Hedin, C. Juhlin, and H. Lorenz. Zero-Offset VSP in the COSC-1 borehole. *Geophysical Research Abstracts*, 17, 2015. doi: EGU2015-3255.

R.D. Law, M.P. Searle, and L. Godin. *Channel Flow, Ductile Extrusion and Exhumation in Continental Collision Zones*. Geological Society, London, Special Publications, 268, 2006. ISBN 1-86239-209-9.

A.R. Levander. Fourth-order finite-difference P-SV seismograms. *Geophysics*, 53(11):1425–1436, 1988. doi: 10.1190/1.1442422.

R.J. LeVeque. *Numerical methods for conservation laws*. Birkhäuser, 2nd edition, 1992. ISBN 978-3764327231.

X.-P. Li and S. Richwalski. Seismic attenuation and velocities of P- and S-waves in the German KTB area. *Journal of Applied Geophysics*, 36(2-3):67–76, 1996. doi: 10.1016/S0926-9851(96)00036-5.

A. Licciardi, N. Piana Agostinetti, S. Lebedev, A.J. Schaeffer, P.W. Readman, and C. Horan. Moho depth and Vp/Vs in Ireland from teleseismic receiver functions analysis. *Geophysical Journal International*, 199(1):561–579, 2014. doi: 10.1093/gji/ggu277.

H. Lorenz, J.-E. Rosberg, C. Juhlin, L. Bjelm, B.S.G. Almqvist, T. Berthet, R. Conze, D.G. Gee, I. Klonowska, C. Pascal, K. Pedersen, N.M.W. Roberts, and C.-F. Tsang. COSC-1 - drilling of a subduction-related allochthon in the Palaeozoic Caledonide orogen of Scandinavia. *Scientific Drilling*, 19:1–11, 2015a. doi: 10.5194/sd-19-1-2015.

H. Lorenz, J.-E. Rosberg, C. Juhlin, L. Bjelm, B.S.G. Almqvist, T. Berthet, R. Conze, D.G. Gee, I. Klonowska, C. Pascal, K. Pedersen, N.M.W. Roberts, and C.-F. Tsang. Operational report about phase 1 of the Collisional Orogeny in the Scandinavian Caledonides scientific driling project (COSC-1). *GFZ German Research Centre for Geosciences*, 2015b. doi: 10.2312/ICDP.2015.002.

H. Lorenz, J.-E. Rosberg, C. Juhlin, L. Bjelm, B.S.G. Almqvist, T. Berthet, R. Conze, D.G. Gee, I. Klonowska, C. Pascal, K. Pedersen, N.M.W. Roberts, and C.-F. Tsang. COSC-1 operational report - Scientific data sets. *GFZ German Research Centre for Geosciences*, 2015c. doi: 10.1594/GFZ.SDDB.ICDP.5054.2015.

W. Lowrie. *Fundamentals of Geophysics*. Cambridge University Press, 2nd edition, 2007. ISBN 978-0-521-85902-8.

E. Lüschen, K. Bram, W. Söllner, and S. Sobolev. Nature of seismic reflections and velocities from VSP-experiments and borehole measurements at the KTB deep drilling site in southeast Germany. *Tectonophysics*, 264(1):309–326, 1996. doi: 10.1016/S0040-1951(96)00134-5.

J.-L. Mari, F. Glangeaud, and F. Coppens. *Signal Processing for Geologists and Geophysicists*. Editions Technip, 1999. ISBN 978-2710807520.

J.L. Mari, P. Gaudiani, and J. Delay. Characterization of geological formations by physical parameters obtained through full waveform acoustic logging. *Physics and Chemistry of the Earth, Parts A/B/C*, 36(17-18):1438–1449, 2011. doi: 10.1016/j.pce.2011.07.011.

W.S. McKerrow, C. Mac Niocaill, and J.F. Dewey. The Caledonian Orogeny redefined. *Journal of the Geological Society*, 157(6):1149–1154, 2000. doi: 10.1144/jgs.157.6.1149.

H. Palm. Time-delay interpretation of seismic refraction data in the Caledonian front, Jämtland, central Scandinavian Caledonides. *Geoliska Föreningens i Stockholm Förhandlingar*, 106(1):1–14, 1984. doi: 10.1080/11035898409454597.

H. Palm, D.G. Gee, D. Dyrelius, and L. Björklund. A reflection seismic image of Caledonian structure in central Sweden. *Sveriges Geologiska Undersökning, Ca 75*, 1991.

G.R. Pickett. The use of acoustic logs in the evaluation of sandstone reservoirs. *Geophysics*, 25(1): 250–274, 1960. doi: 10.1190/1.1438691.

W.L. Pilant. *Elastic waves in the Earth*. Elsevier B.V., 1st edition, 1979. ISBN 978-0-444-41798-5.

D. Roberts and D.G. Gee. An introduction to the structure of the Scandinavian Caledonides. In *The Caledonide Orogen: Scandinavia and Related Areas*. John Wiley and Sons Ltd., 1985. ISBN 0-471-10504-X.

J.-E. Rosberg and H. Lorenz. A new scientific drilling infrastructure in Sweden. *Geophysical Research Abstracts*, 14, 2012. doi: EGU2012-7379.

R.M. Rudnick and D.M. Fountain. Nature and composition of the continental crust: A lower crustal perspective. *Review of Geophysics*, 33(3):267–309, 1995. doi: 10.1029/95RG01302.

M.H. Salisbury, C.W. Harvey, and L. Matthews. The acoustic properties of ores and host rocks in hardrock terranes. In *Hardrock Seismic Exploration*, volume 10, pages 9–19. Society of Exploration Geophysicists, 2003. ISBN 1-56080-114-X.

D.R. Schmitt, C.J. Mwenifumbo, K.A. Pflug, and I.L. Meglis. Geophysical logging for elastic properties in hard rock: a tutorial. In *Hardrock Seismic Exploration*, volume 10, pages 20–42. Society of Exploration Geophysicists, 2003. ISBN 1-56080-114-X.

A. Sei. A family of numerical schemes for the computation of elastic waves. *SIAM Journal on Scientific Computing*, 16(4):898–916, 1995. doi: 10.1137/0916052.

O. Serra. *Fundamentals of well-log interpretation*. Elsevier, 1st edition, 1984. ISBN 0-444-42132-7.

D.M. Shaw, A.P. Dickin, H. Li, R.H. McNutt, H.P. Schwarcz, and M.G. Truscott. Crustal geochemistry in the Wawa-Foleyet region, Ontario. *Canadian Journal of Earth Sciences*, 31(7):1104–1121, 1994. doi: 10.1139/e94-099.

H. Simon, F. Krauß, P. Hedin, S. Buske, R. Giese, and C. Juhlin. A combined surface and borehole seismic survey at the COSC-1 borehole. *Geophysical Research Abstracts*, 17, 2015. doi: EGU2015-4554.

A.S.L. Sjöqvist, M. Arthursson, A. Lundström, E. Calderén Estrada, A. Inerfeldt, and H. Lorenz. An innovative optical and chemical drill core scanner. *Scientific Drilling*, 19:13–16, 2015. doi: 10.5194/sd-19-13-2015.

S.B. Smithson, F. Wenzel, Y.V. Ganchin, and I.B. Morozov. Seismic results at Kola and KTB deep scientific boreholes: velocities, reflections, fluids, and crustal composition. *Tectonophysics*, 392(1-4): 301–317, 2000. doi: 10.1016/S0040-1951(00)00200-6.

R.R. Stewart, P.D. Huddleston, and T.K. Kan. Seismic versus sonic velocities: A vertical seismic profiling study. *Geophysics*, 49(8):1153–1168, 1984. doi: 10.1190/1.1441745.

A.G.B. Strömberg, L. Karis, E. Zachrisson, T. Sjöstrand, and R. Skogland. Geological Map of Jämtland County (Caledonides), Scale 1:2,000,000. *Sveriges Geologiska Undersökning, Ca 53*, 1994.

D.H. Thomas. *Seismic applications of sonic logs*, volume 19. 1978.

L. Thomsen. Weak elastic anisotropy. *Geophysics*, 51(10):1954–1966, 1986. doi: 10.1190/1.1442051.

J. Thorbecke. *2D Finite-DifferenceWavefield Modelling*, 2016.

A.E. Törnebohm. Om fjällproblemet. *Geoliska Föreningens i Stockholm Förhandlingar*, 10(5):328–336, 1888. doi: 10.1080/11035898809444211.

C.-F. Tsang, J.-E. Rosberg, P. Sharma, T. Berthet, A. Niemi, and C. Juhlin. Hydrogeologic testing during drilling: Application of flowing fluid electrical conductivity (FFEC) logging method hydrologic testing during drilling of a deep borehole. *Hydrogeological Journal*, 2016. doi: 10.1007/s10040-016-1405-z.

J. Virieux. P-SV wave propagation in heterogeneous media; velocity-stress finite-difference method. *Geophysics*, 51(4):889–901, 1986. doi: 10.1190/1.1442147.

J. Virieux, V. Etienne, V. Cruz-Atienza, R. Brossier, E. Chaljub, O. Coutant, S. Garambois, D. Mercerat, V. Prieux, S. Operto, Ribodetti A., and J. Tago. Modelling seismic wave propagation for geophysical imaging. In *Seismic Waves - Research and Analysis*. InTech, 2012. ISBN 978-953-307-944-8. doi: 10.5772/30219.

C.P.A. Wapenaar and A.J. Berkhout. *Advances in Exploration Geophysics*, volume 2nd. Elsevier B.V., 1st edition, 1989. ISBN 978-0-444-88472-5.

B.L. Weaver and J. Tarney. Empirical approach to estimating the composition of the continental crust. *Nature*, 310:575–577, 1984. doi: 10.1038/310575a0.

R.M. Weiss and J. Shragge. Solving 3D anisotropic elastic wave equations on parallel GPU devices. *Geophysics*, 78(2):F7–F15, 2013. doi: 10.1190/geo2012-0063.1.

Q.C. Wenning. Physical rock property and borehole stress measurements from the COSC-1 borehole Åre, Sweden. Master's thesis, Swiss Federal Institute of Technology Zürich, 2015.

Q.C. Wenning, B. Almquist, P. Hedin, and A Zappone. Seismic anisotropy in mid to lower orogenic crust: Insights from laboratory measurements of Vp and Vs in drill core from central Scandinavian Caledonides. *Tectonophysics*, 2016. doi: 10.1016/j.tecto.2016.07.002.

O. Yilmaz. *Seismic Data Analysis*. Society of Exploration Geophysicists, 2001. ISBN 978-1-56080-094-1.

APPENDIX A

Seismic modelling in Madagascar

A.1 Utilisation of Madagascar

Madagascar is an open-source software package which implements a computational environment that is designed for conducting computational challenging experiments in the area of large-scale geophysical data analysis (Fomel et al., 2013). The Madagascar program can be found on `http://www.ahay.org/wiki/Main_Page/`, where information on the program, reproducible documents and mailing lists can be accessed. Before start using Madagascar, the program needs to be downloaded from `https://sourceforge.net/projects/rsf/files/` and be installed by following the instructions on `http://www.ahay.org/wiki/Installation`.

In this thesis is seismic modelling with Madagascar executed by using Linux Ubuntu operating system. Seismic models can be set-up by either writing an own modelling code or by using reproducible documents from the Madagascar website. For this thesis the `ewefd2d` modelling code is used for 2D elastic and isotropic finite-difference modelling. The used modelling code is very versatile to expand the model to 3D and construct a more complicated model by including anisotropy. The utilisation described in this section is based on the experience of employing the `ewefd2d` modelling code, be aware of the many other applications of Madagascar in modelling, seismic processing and more.

The modelling codes are made up on the lowest level by RSF (Regularly Sampled Format) files, which is the format used to exchange information between Madagascar programs. Conceptually, the RSF file format is one of the easiest to understand, as RSF files are simply regularly sampled hypercubes of information. This format is simpler and easier to manage then the SEG-Y format used in conventional seismic processing. In Madagascar, there are two main ways of creating scripts: shell scripts, and Python scripts using `Scons`. The software construction tool `Scons`, used her, manages and reproduces computational experiments and processing flows defined by the RSF files through Python-based scripts. Practically, to start the 2D elastic and isotropic finite-difference modelling three file types are required: `SConstruct`, `.rsf` and `.rsf@`. `Sconstruct` is describing the script that manages the modelling by calling other codes to perform computational experiments (e.g. `fdmod` and `stiffness`). The `.rsf` file for the v_p, v_s and ρ is required when not directly defined in the `Sconstruct`. When many layers or complex input models need to be constructed it is easier to use Matlab and create a matrix of the model, written in a `.rsf@` file for v_p, v_s and ρ. Afterwards, the resulting file from Madagascar which is the model response is converted from RSF to SEG-Y. In this section the used files are given: `SConstruct`, `rsfgenerator.m`, `vp-2d.rsf` and `rsf2segy.sh`.

SConstruct

```
# ------------------------------------------------------------ #
# ------------------------- SConstruct ----------------------- #
# ------------------------------------------------------------ #
from rsf.proj import*       # Begin of a SContruct file
import fdmod,stiffness      # Importing supporting documents

# ------------------------------------------------------------ #
# Model parameters                                             #
# ------------------------------------------------------------ #
par = {
    # Dimension discretisation (distances in km)
    'nx':3001, 'ox':0, 'dx':0.002, 'lx':'x', 'ux':'km',
    'ny':3001, 'oy':0, 'dy':0.002, 'ly':'y', 'uy':'km',
    'nz':1244, 'oz':0, 'dz':0.002, 'lz':'z', 'uz':'km',
    # Time discretisation (time in s)
    'nt':8601, 'ot':0, 'dt':0.0001, 'lt':'t', 'ut':'s', 'kt':100,
    # Source frequency in Hz
    'frq':50,
    # Absorbing boundary implementation
    'nb':150, 'nbell':5,
    # Output and snapshot interval
    'jsnap':50, 'height':10
    }

fdmod.param(par)

# ------------------------------------------------------------ #
# Import and plot vp, vs and density from .@rsf                #
# ------------------------------------------------------------ #
Plot('vp-2d','vp-2d','''
    byte allpos=y bar=y color=j |
    grey flat=n color=j wanttitle=n
    scalebar=y barlabel='Vp (km/s)' barlabelsz=8
    label1="Depth" label2="Offset"
    ''')

Plot('vs-2d','vs-2d','''
    byte allpos=y bar=y color=j |
    grey flat=n color=j wanttitle=n
    scalebar=y barlabel='Vs (km/s)' barlabelsz=8
    label1="Depth" label2="Offset"
    ''')

Plot('ro-2d','ro-2d','''
    byte allpos=y bar=y color=j |
```

```
    grey flat=n color=j wanttitle=n
    scalebar=y barlabel='Density (kg/ckm)' barlabelsz=8
    label1="Depth" label2="Offset"
    ''')

# Combine all plots in one image
Result('input_param','vp-2d vs-2d ro-2d','SideBySideAniso')

# ------------------------------------------------------------ #
# Elastic source wavelet configuration                         #
# ------------------------------------------------------------ #
fdmod.wavelet('wav_',par['frq'],par)
Flow('souz','wav_','math output=input*1')
Flow('soux','wav_','math output=input*0')
Flow('wave-2d',['souz','soux'],'''
    cat axis=2 space=n ${SOURCES[1:2]} |
    transp plane=12 |
    transp plane=23 |
    transp plane=12
    ''')

fdmod.ewavelet('wave-2d','',par)

# ------------------------------------------------------------ #
# Source and receiver position                                 #
# ------------------------------------------------------------ #
xsou    =par['ox']+(par['nx']/2*par['dx']);
zsou    =0.0001

fdmod.point('ss-2d',xsou,zsou,par)
fdmod.horizontal('rr-2d',zsou,par)

# ------------------------------------------------------------ #
# Calculation stiffness matrix and 2D elastic modeling         #
# ------------------------------------------------------------ #
stiffness.iso2d('Ic-2d','vp-2d','vs-2d','ro-2d',par)
stiffness.cplot2d('Ic-2d',1,1,par)
fdmod.ewefd2d('Id-2d','Iw-2d','wave-2d','Ic-2d','ro-2d','''
    'ss-2d','rr-2d','ssou=n opot=n',par)
    ''')

# ------------------------------------------------------------ #
# Plotting model response                                      #
# ------------------------------------------------------------ #
Plot('Id-2d','window n2=1 | transp |' '''
    + fdmod.dgrey('title="Model Response" ',par))
    ''')
```

```
# Application shape AGC to improve image model response
Flow('Id-shapeagc','Id-2d', 'shapeagc rect1=50')
Plot('Id-shapeagc','window n2=1 | transp |' '''
    + fdmod.dgrey('title="Shape AGC rect1=50" ',par))
    ''')

# Combine raw and processed model response in one image
Result('Id-2d-comp','Id-2d Id-shapeagc','SideBySideAniso')

# ------------------------------------------------------------ #
# Movie of wavefield                                           #
# ------------------------------------------------------------ #
Plot('Iw-2d','''
    window n3=1 |
    grey gainpanel=all title=Wave
    label1=Depth unit1=km label2=Offset unit2=km
    ''')

# ------------------------------------------------------------ #
# Snapshot of wavefield                                        #
# ------------------------------------------------------------ #
Result('wave_snapshot','Iw-2d','''
    window f4=1 n4=1 n3=1 | byte gainpanel=all pclip=99 |
    grey title="Wavefield at t=0.75s"
    wheretitle=t
    labelsz=4 label1=Depth unit1=km label2=Offset unit2=km
    ''')

End()
# ------------------------------------------------------------ #
# End of SConstruct                                            #
# ------------------------------------------------------------ #
```

rsfcreator.m

```
% ------------------------------------------------------------------------ %
% ------------------------------ rsfcreator.m ---------------------------- %
% ------------------------------------------------------------------------ %
function rsfcreator(vp2d,vs2d,ro2d,dz,dx,datapath)

% ------------------------------------------------------------------------ %
% Function reads a matrix representing the vp, vs and density input models
% (all matrices should be the same size) and outputs .rsf and .rsf@
% required for 2D modelling in Madagascar. Note: dimensions of the model
% are expressed in km.
%
% INPUT:
% vp2d       matrix of the compressional wave model (nz x nz)
% vs2d       matrix of the shear wave model (nz x nz)
% ro2d       matrix of the density wave model (nz x nz)
% dz         spatial increment in the z-direction
% dx         spatial increment in the x-direction
% datapath   datapath to the location of the .rsf@ file for Madagascar
%
% OUTPUT:
% vp-2d.rsf vs-2d.rsf ro-2d.rsf vp-2d.rsf@ vs-2d.rsf@ ro-2d.rsf@
%
% Written by: M.C. Ooms, 12 August 2016.
% ------------------------------------------------------------------------ %

% Parameters
[nz,nx] = size(vp2d);
n1 = nz;
n2 = nx;
n3 = 1;
d1 = dz;
d2 = dx;
o1 = 0;
o2 = 0;
unit1 = 'km';
unit2 = 'km';
label1 = 'z';
label2 = 'x';

vp_name = 'vp-2d';  % Output file name for vp
vs_name = 'vs-2d';  % Output file name for vs
ro_name = 'ro-2d';  % Output file name for density

% Write .rsf header file for vp, vs and density
fidh = fopen([vp_name '.rsf'],'w');
```

```
fprintf(fidh,'%s\n',['n1=' num2str(n1)]);
fprintf(fidh,'%s\n',['n2=' num2str(n2)]);
fprintf(fidh,'%s\n',['n3=' num2str(n3)]);
fprintf(fidh,'%s\n',['d1=' num2str(d1)]);
fprintf(fidh,'%s\n',['d2=' num2str(d2)]);
fprintf(fidh,'%s\n',['o1=' num2str(o1)]);
fprintf(fidh,'%s\n',['o2=' num2str(o2)]);
fprintf(fidh,'%s\n',['unit1="' unit1 '"']);
fprintf(fidh,'%s\n',['unit2="' unit2 '"']);
fprintf(fidh,'%s\n',['label1="' label1 '"']);
fprintf(fidh,'%s\n',['label2="' label2 '"']);
fprintf(fidh,'%s\n','data_format="native_float"');
fprintf(fidh,'%s\n','esize=4');
fprintf(fidh,'%s\n',['in="' datapath 'vp-2d.rsf@"']);
fclose(fidh);

fidh = fopen([vs_name '.rsf'],'w');
fprintf(fidh,'%s\n',['n1=' num2str(n1)]);
fprintf(fidh,'%s\n',['n2=' num2str(n2)]);
fprintf(fidh,'%s\n',['n3=' num2str(n3)]);
fprintf(fidh,'%s\n',['d1=' num2str(d1)]);
fprintf(fidh,'%s\n',['d2=' num2str(d2)]);
fprintf(fidh,'%s\n',['o1=' num2str(o1)]);
fprintf(fidh,'%s\n',['o2=' num2str(o2)]);
fprintf(fidh,'%s\n',['unit1="' unit1 '"']);
fprintf(fidh,'%s\n',['unit2="' unit2 '"']);
fprintf(fidh,'%s\n',['label1="' label1 '"']);
fprintf(fidh,'%s\n',['label2="' label2 '"']);
fprintf(fidh,'%s\n','data_format="native_float"');
fprintf(fidh,'%s\n','esize=4');
fprintf(fidh,'%s\n',['in="' datapath 'vs-2d.rsf@"']);
fclose(fidh);

fidh = fopen([ro_name '.rsf'],'w');
fprintf(fidh,'%s\n',['n1=' num2str(n1)]);
fprintf(fidh,'%s\n',['n2=' num2str(n2)]);
fprintf(fidh,'%s\n',['n3=' num2str(n3)]);
fprintf(fidh,'%s\n',['d1=' num2str(d1)]);
fprintf(fidh,'%s\n',['d2=' num2str(d2)]);
fprintf(fidh,'%s\n',['o1=' num2str(o1)]);
fprintf(fidh,'%s\n',['o2=' num2str(o2)]);
fprintf(fidh,'%s\n',['unit1="' unit1 '"']);
fprintf(fidh,'%s\n',['unit2="' unit2 '"']);
fprintf(fidh,'%s\n',['label1="' label1 '"']);
fprintf(fidh,'%s\n',['label2="' label2 '"']);
fprintf(fidh,'%s\n','data_format="native_float"');
fprintf(fidh,'%s\n','esize=4');
```

```
fprintf(fidh,'%s\n',['in="' datapath 'ro-2d.rsf@"']);
fclose(fidh);

% Write .rsf@ file for vp, vs and density
fidd = fopen([vp_name '.rsf@'],'w');
    for x=1:n2
        for z=1:n1
            fwrite(fidd,vp2d(z,x),'single');
        end
    end
fclose(fidd);

fidd = fopen([vs_name '.rsf@'],'w');
    for x=1:n2
        for z=1:n1
            fwrite(fidd,vs2d(z,x),'single');
        end
    end
fclose(fidd);

fidd = fopen([ro_name '.rsf@'],'w');
    for x=1:n2
        for z=1:n1
            fwrite(fidd,ro2d(z,x),'single');
        end
    end
fclose(fidd);
% ------------------------------------------------------------------------ %
% End of rsfcreator.m                                                      %
% ------------------------------------------------------------------------ %
```

vp-2d.rsf

As an example the file structure of `vp-2d.rsf` is shown as a result of the `rsfcreator.m` output, similar structures are given for `vs-2d.rsf` and `ro-2d.rsf`.

```
# ------------------------------------------------------------ #
# ------------------------- vp-2d.rsf ------------------------ #
# ------------------------------------------------------------ #
n1=3244
n2=3001
n3=1
d1=0.002
d2=0.002
o1=0
o2=0
unit1="km"
unit2="km"
label1="z"
label2="x"
data_format="native_float"
esize=4
in="/var/tmp/Documents/Madagascar/Model/vp-2d.rsf@"
# ------------------------------------------------------------ #
# End of vp-2d.rsf                                             #
# ------------------------------------------------------------ #
```

rsf2segy.sh

```
# ------------------------------------------------------------ #
# ------------------------ rsf2segy.sh ----------------------- #
# ------------------------------------------------------------ #
#!/bin/sh

# Parameters
input=Id-2d      # Input .rsf file
n=8601           # Number of samples in time domain
d=0.0001         # Sampling rate

< $input.rsf sftransp plane=23 | sftransp plane=12 |
sfwindow n3=1 | sfremap1 d1=$d n1=$n  > $input-2.rsf
sfsegyheader < $input-2.rsf > tfile.rsf
sfsegywrite  < $input-2.rsf tfile=tfile.rsf > Seismic/$input.segy

# ------------------------------------------------------------ #
# End of rsf2segy.sh                                           #
# ------------------------------------------------------------ #
```

A.2 2D elastic and isotropic finite-difference testing

The 2D model of the COSC-1 borehole is performed to acquire the zero-offset trace and analyse wave conversion as an offset function. The treatment of the surface is an important parameter in seismic modelling. The `ewefd2d` modelling code provides an implementation of absorbing and free surface boundary conditions for the surface. The results of testing the different boundary conditions are discussed in this section by looking at four models; a homogeneous model and a model representing the COSC-1 borehole with absorbing boundaries and free surface. The model parameters are given in Table 5.1) for all models.

Model 2 and 3

Model 2 and 3 are two homogeneous models of calc-silicate gneiss calc-silicate gneiss (Figure A.1; v_p = 6358 m/s, v_s = 3653 m/s, ρ = 2.726 g/cm^3). Model 2 has absorbing boundaries of 150 grid points and Model 3 has a free surface implementation. In Figure A.2 are for each model (Figures A.2a-b for Model 2 and Figures A.2c-d for Model 3) two snapshots of the wave fields shown at time, t = 0.15 s and t = 0.25 s. The absorbing boundaries of Model 2 are performing well, the wave field gets attenuated and due to the used homogeneous model, minor reflections occur from the boundary in both wave field snapshots. The free surface of Model 3, on the other hand, causes severe reflections at the surface. The stress is not zero of the wave field at the surface but gets reflected as an interface in the model itself, also triangular wave form spreading with a similar velocity as the S-wave.

The raw and processed model responses of Model 2 and 3 are compared in Figure A.3. Processing steps applied to the raw model response are trace balancing (0-860 ms), spherical divergence correction ($\sqrt{t}$) and adding bias (0.02). The processed model response of Model 2 in Figure A.3a shows only the arrival of the P- and S-wave, where the processed model response of Model 3 in Figure A.3b shows many linear reflections of P- and S-wave reverberating at the surface. The free surface implementation causes severe problems on the wave field simulation and the model response in a homogeneous medium. The influence of both boundary conditions is further assessed on the actual representation of the COSC-1 borehole.

Model 4 and 5

Model 4 and 5 represent the COSC-1 borehole and are defined by the v_p, v_s and density values of the FWS logging results and core density measurements, similar to the 1D seismic model. The data points averaged over 50 cm and the first 103 m is approximated by v_p = 5200 m/s, v_s = 3000 m/s and ρ = 2.68 g/cm^3 (Figure A.4). Missing values of the v_s over depth due to picking difficulties are approximated by Equation 3.4. In Figure A.5 are for each model (Figures A.5a-b for Model 4 and Figures A.5c-d for Model 5) two snapshots of the wave fields shown at time, t = 0.25 s and t = 0.45 s. Similar to Model 2 and 3, the absorbing boundaries of Model 4 are performing well, the wave field shows reflections occurring throughout the simulation, at the surface wave fields get attenuated and cause reflections from the surface. The free surface of Model 5, on the other hand, causes reflections, but also strong internal reflections at the surface propagating with the same velocity as the S-wave. The stress is not zero of the wave field at the surface but gets reflected by an interface in the model itself, also triangular wave form spreading with a similar velocity as the S-wave.

The raw and processed model responses of Model 4 and 5 are compared in Figure A.6. Processing steps applied to the raw model response are trace balancing (0-860 ms), spherical divergence correction ($\sqrt{t}$) and adding bias (0.02). The processed model response of Model 4 in Figure A.6a shows reflections throughout the model as expected. However, the influence of reflection from the surface, shown in Figure

A.5a-b, cannot be quantitatively analysed and therefore not be used to represent the zero-offset trace as the representation of the borehole. The processed model response of Model 5 in Figure A.6b shows many linear reflections between the S-wave and zero-offset, making it impossible to determine important reflections in the borehole. The model response is so full of noise from the surface as a result of the free surface boundary condition making it impossible to further explore this boundary condition. Other solutions need to be found for obtaining a true amplitude zero-offset trace of the seismic model.

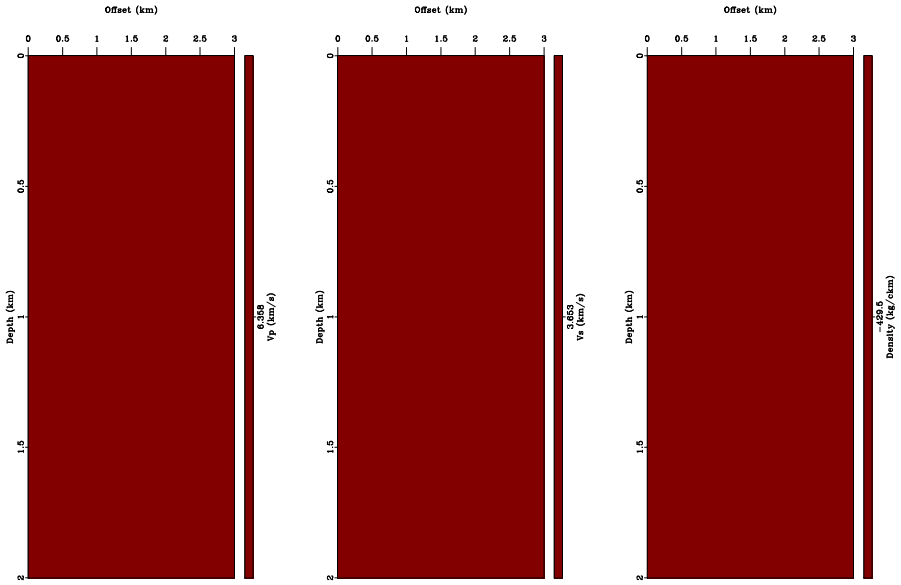

Figure A.1: Input parameters of a homogeneous model (Model 2 and 3 in Table 5.1).

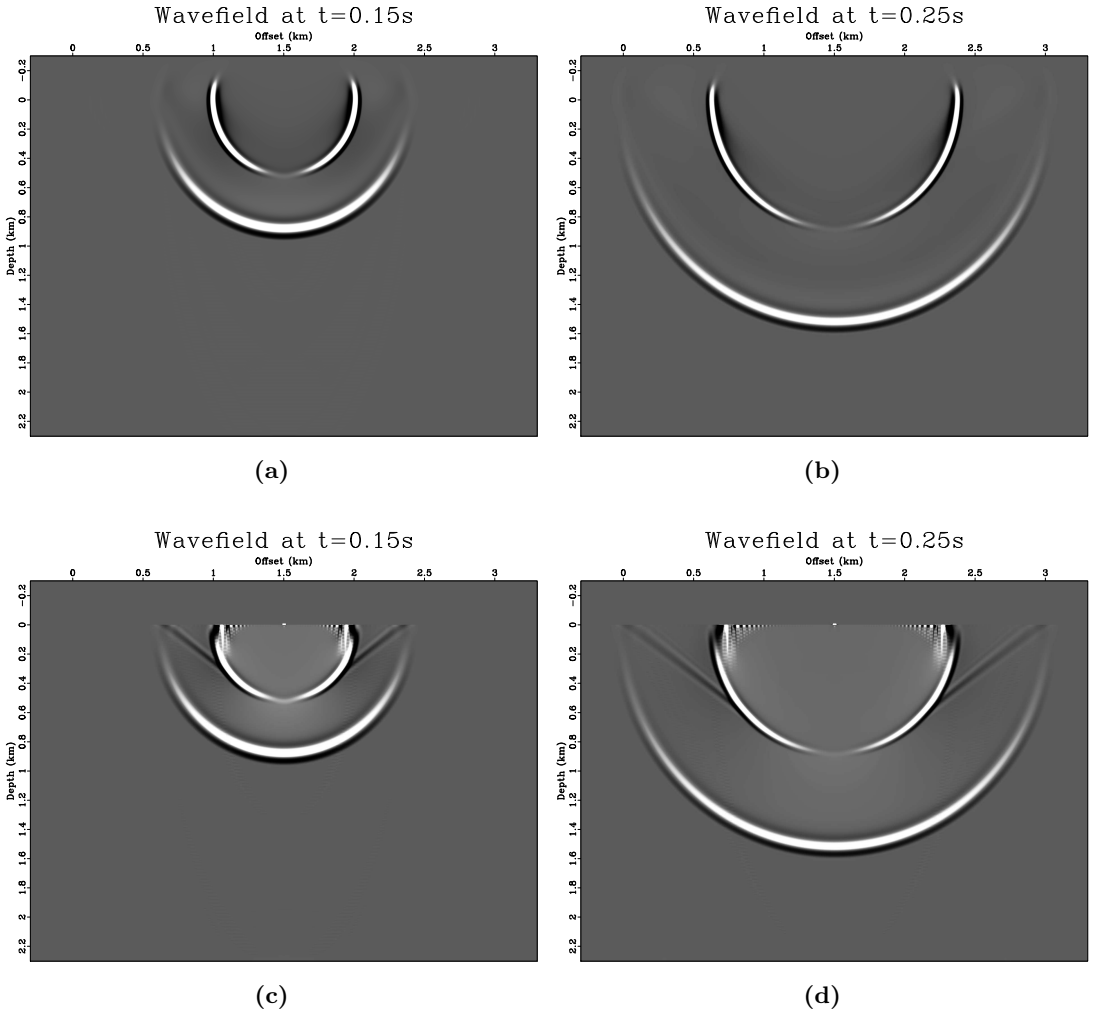

Figure A.2: Wave field snapshots of two homogeneous models with different boundary treatment (Model 2 and 3 in Table 5.1) at time: a) and b) is a homogeneous medium with absorbing boundaries at times $t = 0.15$ s and $t = 0.25$ s, c) and d) is a homogeneous medium with a free surface at times $t = 0.15$ s and $t = 0.25$ s.

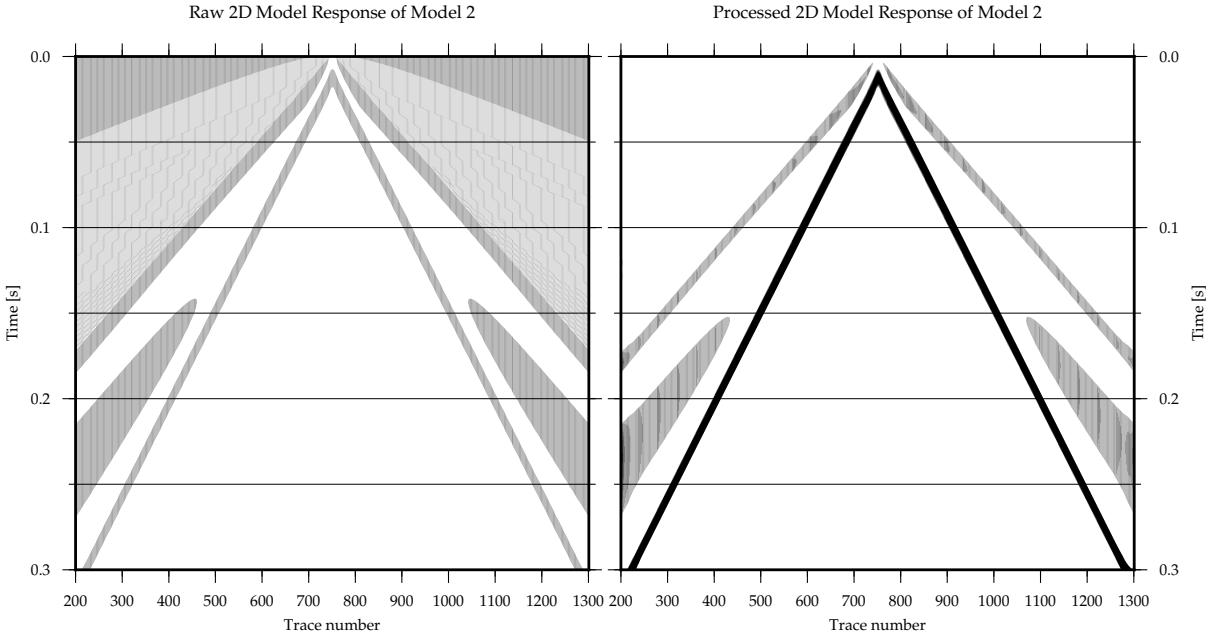

(a)

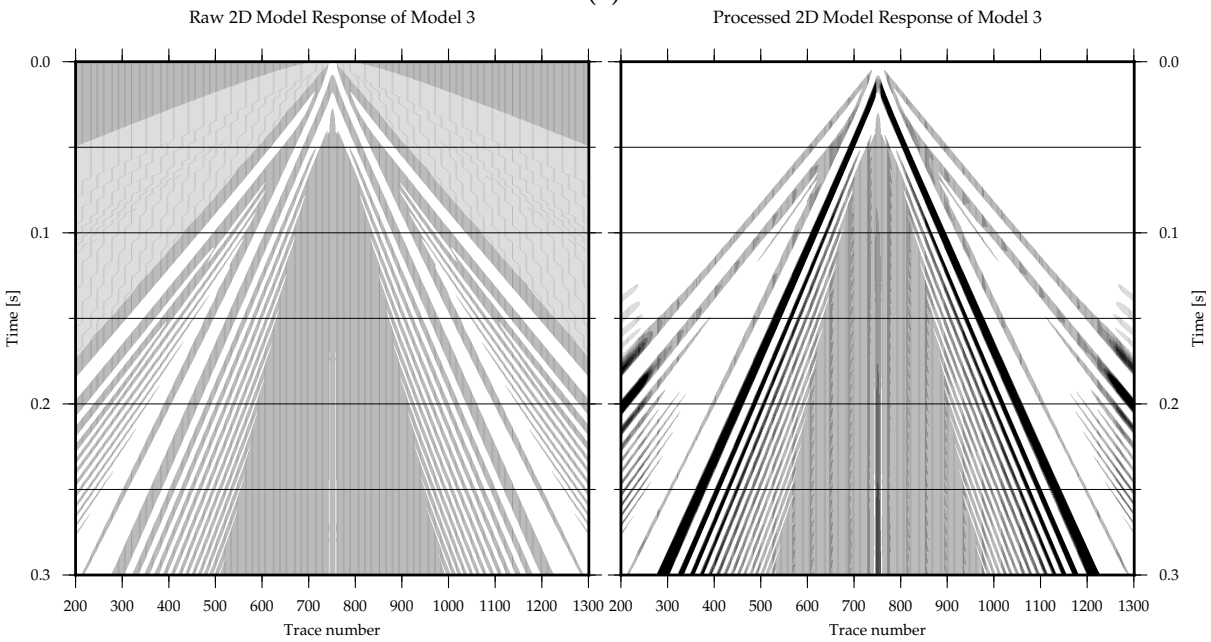

(b)

Figure A.3: Comparison of a homogeneous model response with different boundary treatment (Model 2 and 3 in Table 5.1). a) is the model with absorbing boundaries and b) the model with a free surface. In a) and b) is the left panel displaying the raw model response and the right panel is displaying the model response after processing.

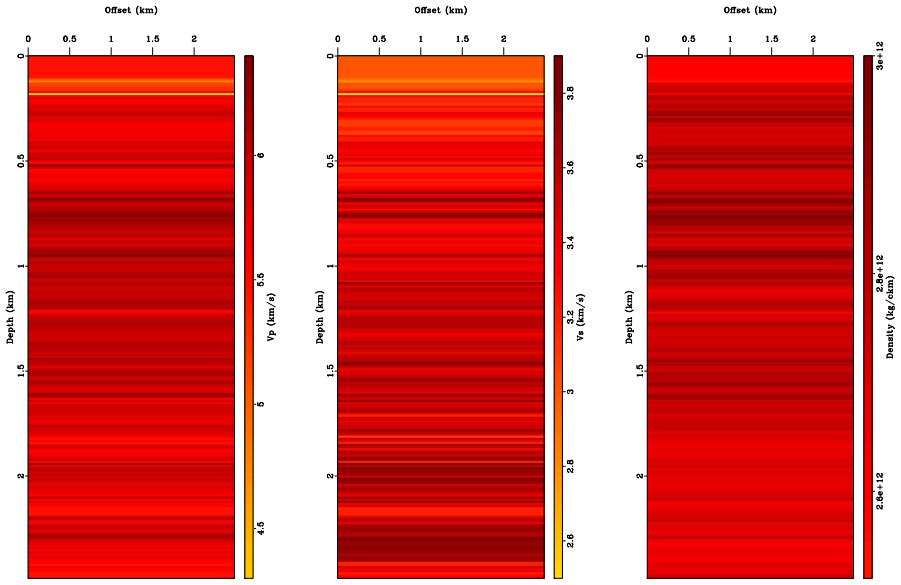

Figure A.4: Input parameters of the model representing the COSC-1 borehole (Model 4 and 5 in Table 5.1).

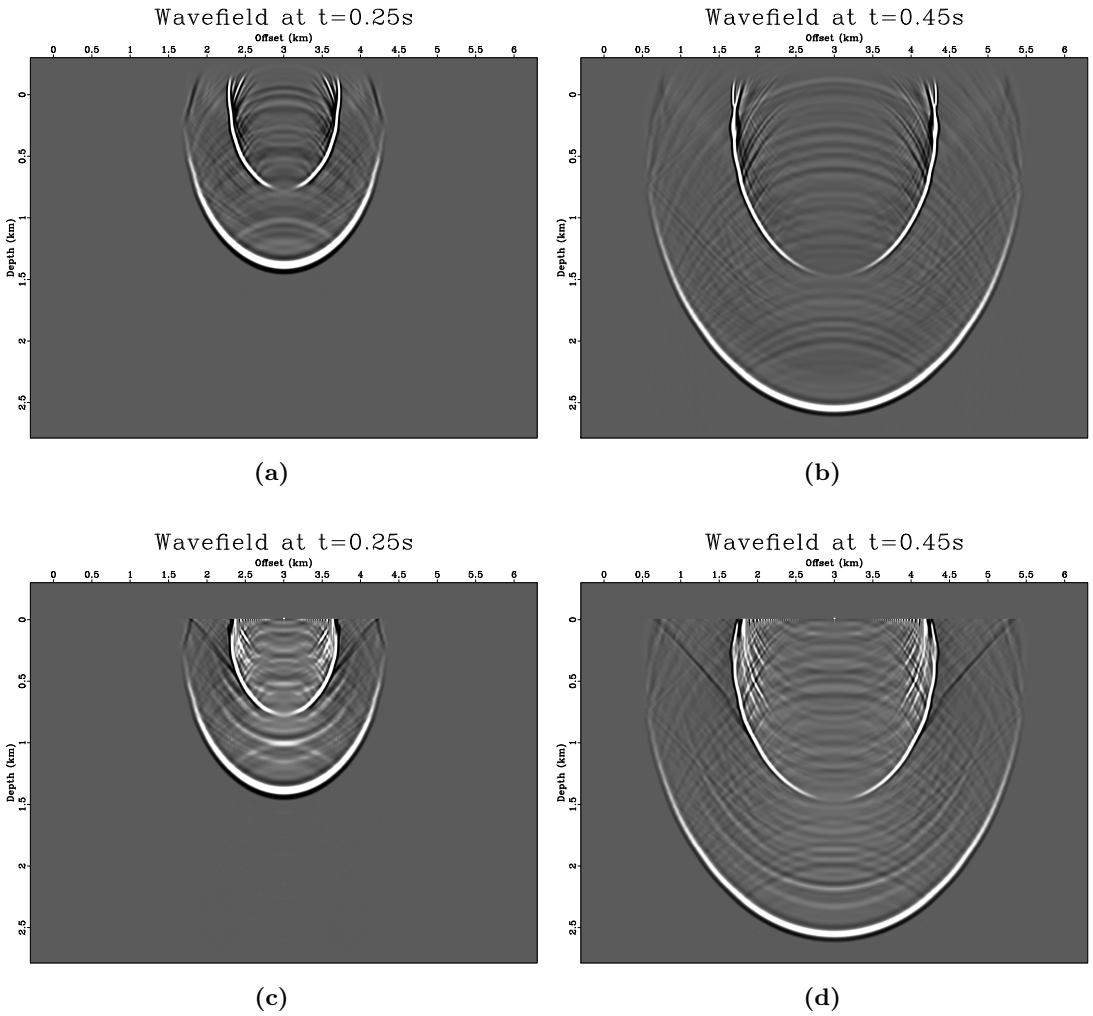

Figure A.5: Wave field snapshots of the model representing the COSC-1 borehole with different boundary treatment (Model 4 and 5 in Table 5.1) at time: a) and b) is the medium with absorbing boundaries at times $t = 0.25$ s and $t = 0.45$ s, c) and d) is the with a free surface at times $t = 0.25$ s and $t = 0.45$ s.

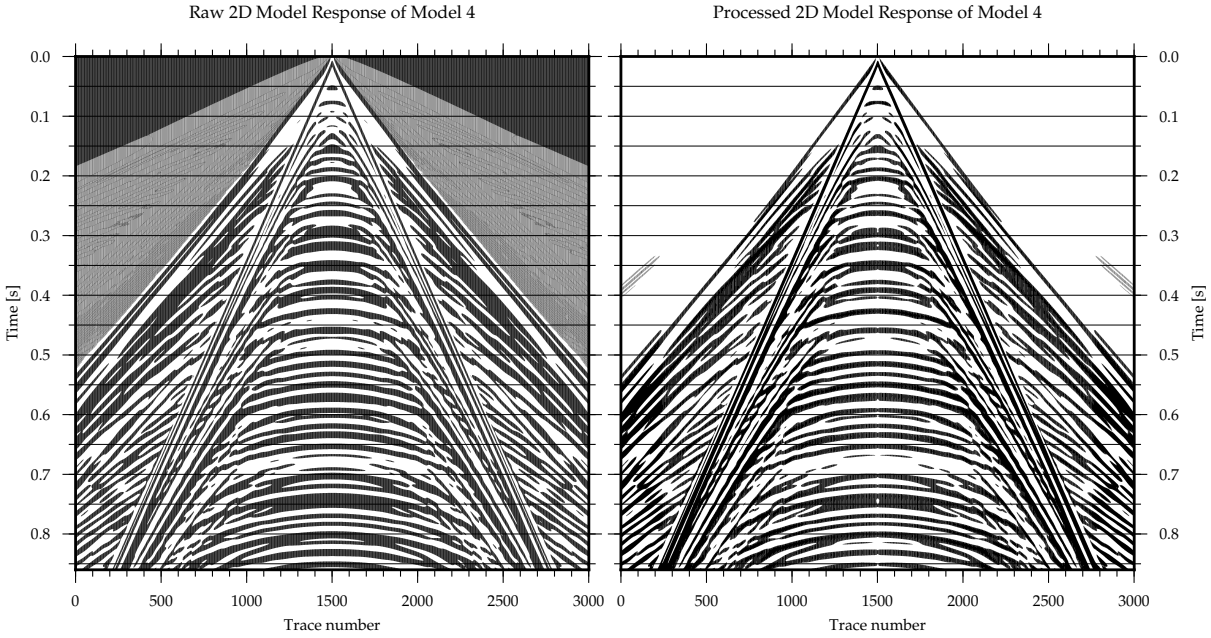

(a)

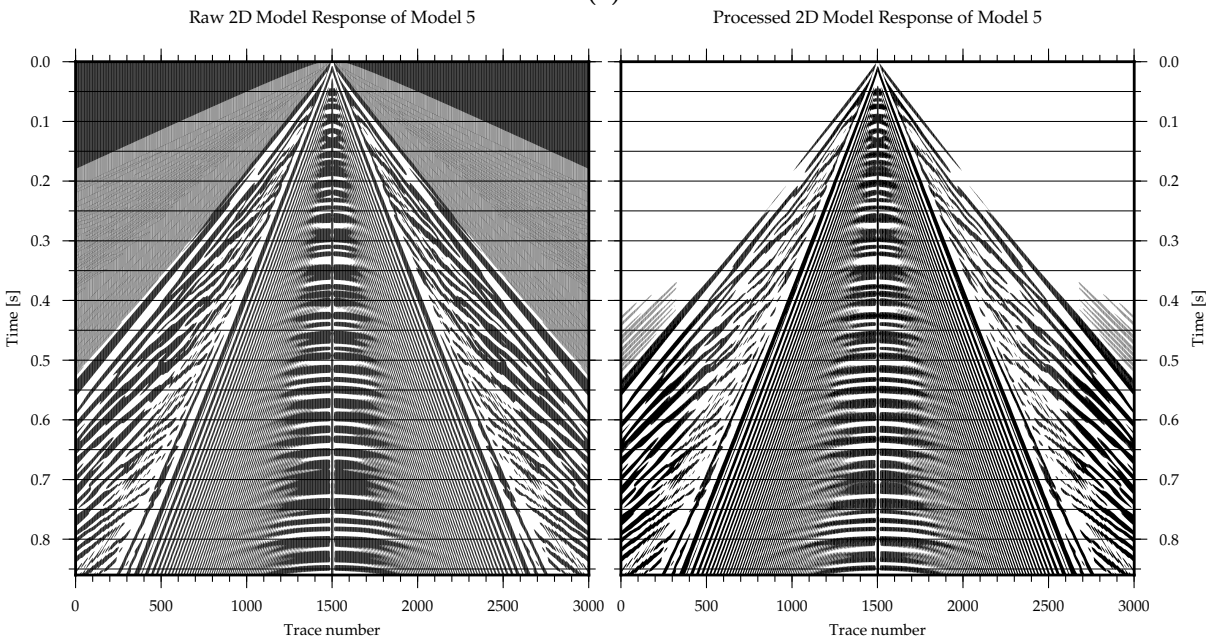

(b)

Figure A.6: Comparison of the COSC-1 borehole model response with different boundary treatment (Model 4 and 5 in Table 5.1). a) is the model with absorbing boundaries and b) the model with a free surface. In a) and b) is the left panel displaying the raw model response and the right panel is displaying the model response after processing.

APPENDIX B

Effect of averaging on logs

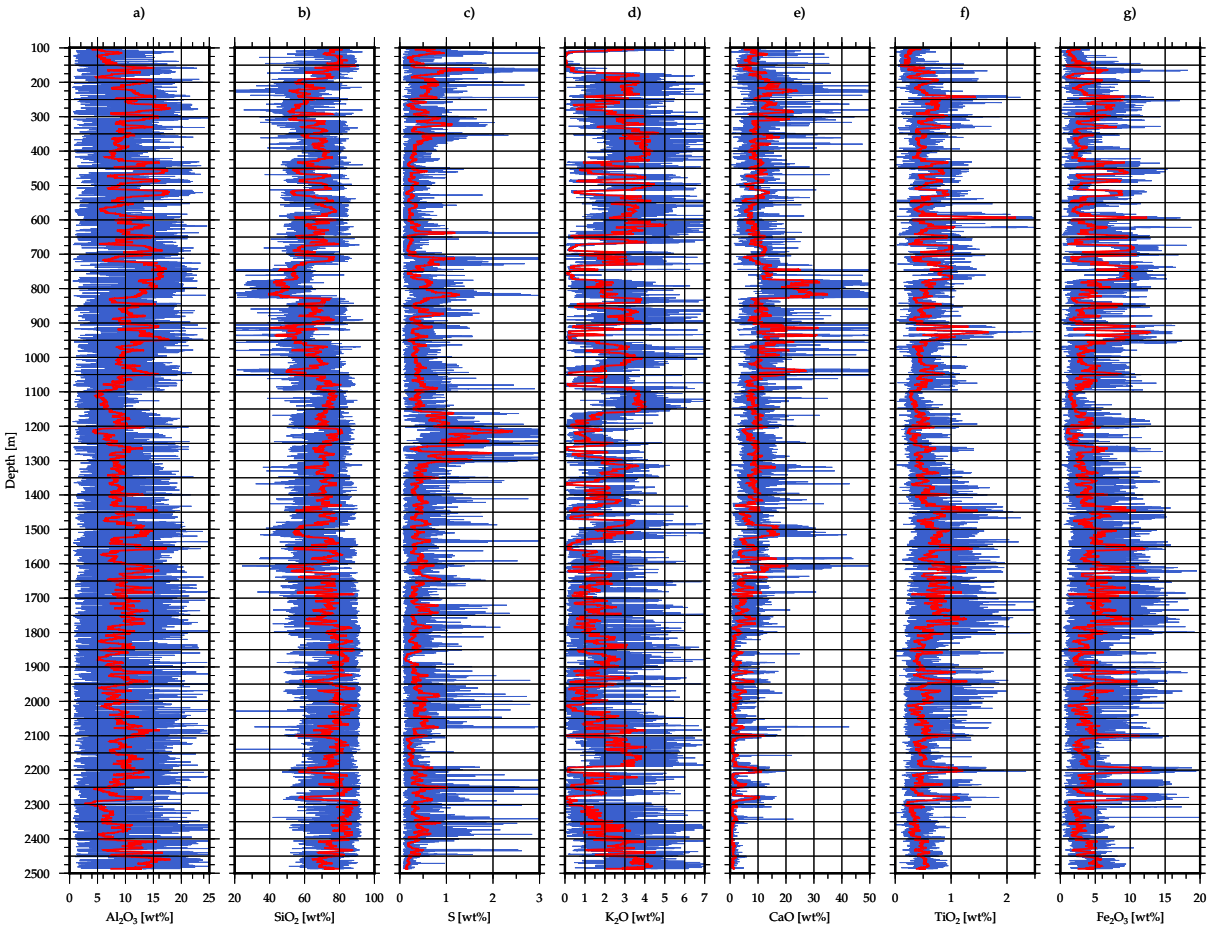

Figure B.1: The mass fraction of several geochemical components with depth within the interval of 100-1600 m measured by the Minalyze CS XRF scanner. a) Al_2O_3, b) SiO_2, c) S, d) K_2O, e) CaO, f) TiO_2 and g) Fe_2O_3. The data points originate from an interpolation over 10 cm of continuous measurement, removal of physically unreal values and applying a 75 data points moving average. In blue is the actual data and in red the 75 data point averaged data.

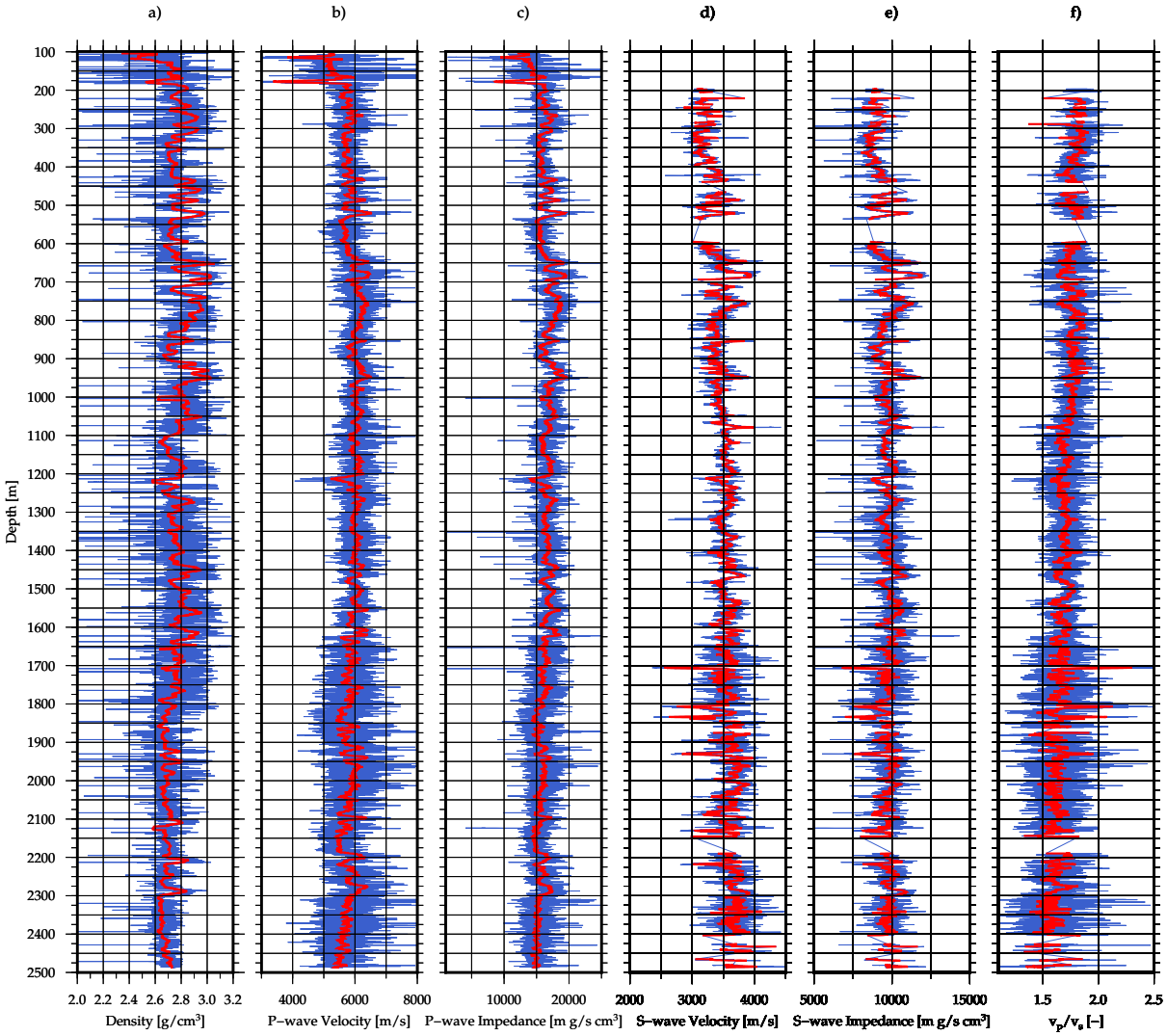

Figure B.2: Acoustic parameters and density udes for correlation to the XRF data. a) density, b) v_p, c) Z_p, d) v_s, e) Z_s and f) v_p/v_s ratio. The data points originate removal of physically unreal values and applying a 25 data points moving average for acoustic parameters and 75 data point moving average for density. In blue is the actual data and in red the averaged data.